DOCUMENTS
GVTDOC
D 211.
9:
4087

Ad 775624

NAVAL SHIP RESEARCH AND DEVELOPMENT CENTER

Bethesda, Maryland 20034

VIBRATORY DYNAMICS OF FLOW-EXCITED STRUTS IN WATER

by

William K. Blake and Lawrence J. Maga

LIBRARY
MAR 14
U.S. NAVAL ACADEMY

APPROVED FOR PUBLIC RELEASE:
DISTRIBUTION UNLIMITED

SHIP ACOUSTICS DEPARTMENT
RESEARCH AND DEVELOPMENT REPORT

20070122042

December 1973 Report 4087

VIBRATORY DYNAMICS OF FLOW-EXCITED STRUTS IN WATER

The Naval Ship Research and Development Center is a U. S. Navy center for laboratory effort directed at achieving improved sea and air vehicles. It was formed in March 1967 by merging the David Taylor Model Basin at Carderock, Maryland with the Marine Engineering Laboratory at Annapolis, Maryland.

Naval Ship Research and Development Center

Bethesda, Md. 20034

MAJOR NSRDC ORGANIZATIONAL COMPONENTS

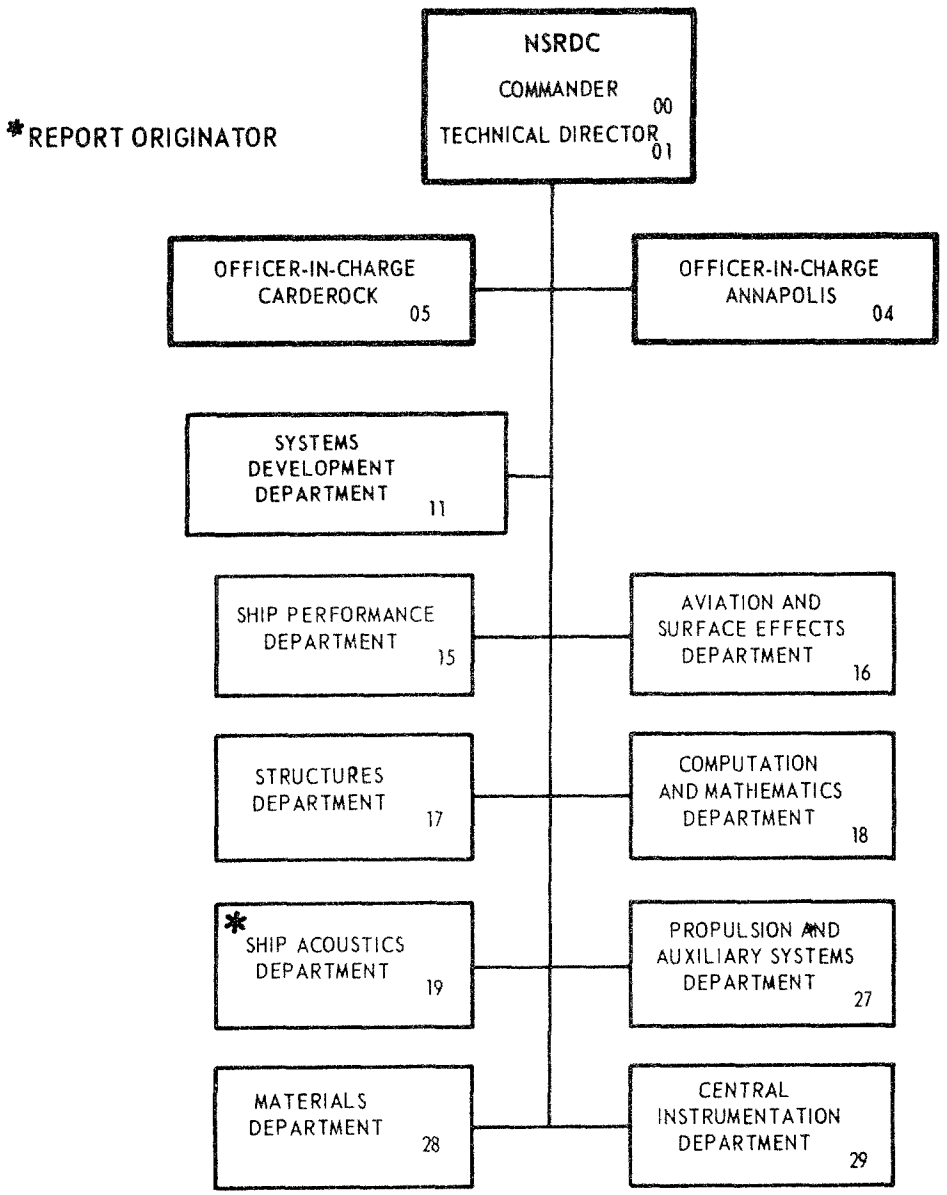

NDW-NSRDC 3960/44 (REV. 8/71)
GPO 917-872

DEPARTMENT OF THE NAVY
NAVAL SHIP RESEARCH AND DEVELOPMENT CENTER
BETHESDA, MD. 20034

VIBRATORY DYNAMICS OF FLOW-EXCITED STRUTS IN WATER

by

William K. Blake and Lawrence J. Maga

APPROVED FOR PUBLIC RELEASE:
DISTRIBUTION UNLIMITED

December 1973 Report 4087

TABLE OF CONTENTS

	Page
ABSTRACT	1
ADMINISTRATIVE INFORMATION	1
1. INTRODUCTION	1
2. AN ANALYTICAL DESCRIPTION OF THE MOTION OF A BEAM IN WATER	3
FORMULATION OF THE BEAM-VIBRATION FIELD	3
HYDRODYNAMIC COUPLING AND DAMPING EFFECTS	7
RESPONSE OF THE WATERLOADED BEAM TO A RANDOM PRESSURE FIELD	11
3. WIND TUNNEL INVESTIGATION OF THE FLUCTUATING PRESSURE FIELD	13
DESCRIPTION OF EXPERIMENT	14
MEAN AND TURBULENT VELOCITY PROFILES	15
STATISTICS OF THE SURFACE PRESSURE FIELD	18
4. WATER TUNNEL INVESTIGATION OF THE DAMPING AND VIBRATION OF A BEAM IN FLOW	21
DESCRIPTION OF EXPERIMENT	22
Description of Test Specimens	22
Water Tunnel and Damping Fixture	22
Vibration Analysis	23
Anemometer Positioning and Flow Measurement	23
Mechanical Impulse Generator	24
Test Procedure	24
RESULTS OF MEASUREMENTS	25
Resonance Frequencies and Mode Shapes	25
Dependence of Damping on Flow	26
Flow-Induced Vibration Measurements	28
Mean and Turbulent Velocity Profiles Behind the Beam	30
5. ANALYTICAL ESTIMATES OF THE FLOW-INDUCED ACCELERATION SPECTRUM	32
RESPONSE TO THE BOUNDARY-LAYER PRESSURE	32
RESPONSE TO INFLOW TURBULENCE	34
6. CONCLUSION	35

Page

ACKNOWLEDGMENT 36

REFERENCES 66

LIST OF FIGURES

Figure 1 – Coordinate System for a Strut Immersed in a Flow Field 37

Figure 2 – Cross Sections of Beams for Air- and Water-Flow Measurement, Showing Coordinates of Sensor Locations 37

Figure 3 – Mean-Velocity Profiles at various Stations along the Strut in the Wind Tunnel at $\alpha = 0$ Degree 38

Figure 4 – Turbulence Intensities, Measured along the Rigid Strut at $\alpha = 0$ Degree in the Wind Tunnel 39

Figure 5 – Mean-Velocity Profiles at various Stations along the Strut in the Wind Tunnel at $\alpha = 2$ Degrees 40

Figure 6 – Turbulence Intensities, Measured along the Rigid Strut at $\alpha = 2$ Degrees in the Wind Tunnel 41

Figure 7 – Increase of Displacement Thicknesses along the Symmetrical Strut at $\alpha = 0$ Degree and 2 Degrees 42

Figure 8 – Comparison of Measured Mean-Velocity Profiles to Coles Law of the Wall for $\alpha = 0$ Degree and 2 Degrees 43

Figure 9 – Autospectra of the Wall Pressure on the Strut in the Wind Tunnel at $\alpha = 0$ Degree 43

Figure 10 – Autospectra near the Semichord, Position A, on the Strut in the Wind Tunnel at $\alpha = 2$ Degrees 44

Figure 11 – Autospectra of the Wall Pressure on the Strut in the Wind Tunnel at $\alpha = 2$ Degrees 44

Figure 12 – Normalized Longitudinal Cross Spectral Density Magnitude on the Rigid Strut at $\alpha = 0$ Degree 45

Figure 13 – Normalized Longitudinal Cross Spectral Density Magnitude on the Rigid Strut at $\alpha = 2$ Degrees 45

Figure 14 – Phase Velocities of the Wall Pressure on the Strut 46

Figure 15 – Normalized Lateral Cross-Spectral Density at Position C on the Strut at $\alpha = 2$ Degrees 47

Figure 16 – Streamwise Coherence of the Pressure Field 47

Figure 17 – Beam Support and Clamping Arrangement 48

Figure 18 – Mechanical Impulse Generator Circuit 49

Page

Figure 19 – Comparison of Theoretically Straight and Experimentally Determined Node Lines of the 2.75-Inch-Wide Beam 50

Figure 20 – Measured and Theoretical Mode Shapes for the Cantilevered Beams in Water 51

Figure 21 – Acceleration Levels, Measured in 3-Hertz Bands on a 2.75-Inch Chord Beam in Flow at 23.5 Feet per Second 52

Figure 22 – Total Loss Factors of the Beams in Water with $U_0 = 0$ 53

Figure 23 – Dependence of the Total Loss Factors of the 2.75-Inch Beam on Flow Speed 54

Figure 24 – Hydrodynamic Loss Factors on the 20-Inch-Long Beams of 1.5- and 2.75-Inch Widths 55

Figure 25 – Hydrodynamic Loss Factors for the 5- by 20-Inch Beam 56

Figure 26 – Hydrodynamic Loss Factors for the 1.5- by 14-Inch Beam, $\ell w/L = 0.428$ 57

Figure 27 – Frequency Spectral Densities, $\overline{a^2} / \Delta f$, Determined from the Flow-Induced Modal Response of the 2.75-Inch Beam 58

Figure 28 – Normalized Acceleration Spectra for the 2.75- by 20-Inch Beam . . . 59

Figure 29 – Normalized Acceleration Spectra for the 5- by 20-Inch Beam 59

Figure 30 – Normalized Acceleration Spectra for the 1.5- by 20-Inch Beam 60

Figure 31 – Normalized Acceleration Spectra for the 1.5- by 14-Inch Beam 60

Figure 32 – Mean-Velocity Profiles at Position F behind the 2.75-Inch Strut in Water 61

Figure 33 – Normalized Turbulence Intensities at Position F behind the 2.75-Inch Strut in Water 61

Figure 34 – Autospectra of the Longitudinal Turbulence Intensity at Position F, $x/h = 0.2$, Measured in Air and Water 62

Figure 35 – Spectral Densities of Background Turbulence Intensities in the Water Tunnel 62

Figure 36 – Comparison of the Measured and Theoretical Dimensionless Acceleration Spectra for the 2.75-Inch Beam 63

LIST OF TABLES

Table 1 – Mean Properties of Boundary Layers 64

Table 2 – Resonance Frequencies in Water and Air 64

Table 3 – Comparison of Boundary Layer Parameters in Air and Water 65

ABSTRACT

The general problem of the response of a cantilevered beam to flow over its surface is considered experimentally and theoretically. The measured flow-induced modal vibratory motion of a nonsinging beam is compared to theoretical estimates of inflow turbulence excitation and boundary-layer excitation. The comparison indicates that while the response to turbulent inflow is dominant at low frequencies, the response of the strut to its own boundary layer is important at high frequencies. The magnitude of hydrodynamically induced damping is also characterized experimentally. It is shown that results agree favorably with an approximate expression based on finite-aspect-ratio, unsteady airfoil theory. Loss factors, based on entrained mass, are found to be inversely proportional to a reduced frequency based on the width of the strut and inflow speed. Finally, a wind tunnel study of the statistical properties of the boundary layer formed on the strut is described. The results disclose that flow separation at the leading edge, which is sensitive to angles of attack, generates a low-frequency pressure field that is markedly higher than that normally encountered in boundary layers. At high frequencies, the pressure field is influenced by the local flow parameters normally used in boundary-layer studies.

ADMINISTRATIVE INFORMATION

The work reported herein was funded by the Naval Ship Systems Command under Subproject S-F35 452 007, Task 15129, Work Unit 1942-057.

1. INTRODUCTION

The motion of a beam in water is influenced by water loading, both hydrodynamically and acoustically. In the case of an unbaffled beam without a mean-fluid motion, the water-loading is due to entrained-fluid inertia arising from fluid forces in phase opposition with acceleration, to acoustic radiation arising from compressible fluid forces in phase opposition with the beam velocity, and to viscous forces arising from shearing in the fluid associated with flow around edges and near nodal points. The viscous effect is generated as the beam moves normal to its neutral surface and sets up a local eddy field which is dissipated by viscosity. The viscous losses have been studied on free-free beams by Blake (1972),[1] who has shown the dependence of this damping on fluid properties and beam geometry. Acoustic

[1] Blake, W. K., "On the Damping of Transverse Motion of Free-Free Beams in Dense Stagnant Fluids," Shock and Vibration Bulletin Vol. 42, Part 4, pp. 41–55 (Jan 1972). A complete listing of references is given on pages 66 and 67.

and inertial fluid reactions on free-free beams have been studied by Blake (1971)[2] for cases in which the length of the acoustic wave is substantially larger than the beam width, thickness, and structural wave length. Also, for beams at frequencies lower than acoustic coincidence, the experiments of Reference 2 have shown that modal coupling may be easily neglected.

When there is mean-fluid motion parallel to the plane of the neutral surface of the beam, the hydrodynamic forces are generated by the potential flow around the beam. Superposition of the steady inflow with the vibration velocity of the beam is manifested in an oscillating angle of attack which results in fluid forces and moments. The motion of the beam generates vorticity in its wake, and the fluid-reaction force is equal to the time rate of change of momentum imparted to the wake. The relative importance of the forces and moments involved in the circulation fluctuations depend on the mode of vibration; they are also capable of introducing coupling between the different modes. We will be concerned with cases involving relative magnitudes of entrained mass, which are less than or comparable to the modal mass of the strut. Also, our considerations will be restricted to low enough speeds that the structure-fluid instabilities leading to flutter divergence are not important. At these low speeds and low ratios of added mass-to-structure mass, the hydrodynamic reactions are largely restricted to forces and moments which oppose the beam motion and are proportional to the beam velocity; they increase the observed damping of the strut.

In addition to the reaction fluid forces, we must characterize the flow-induced excitation forces. These can be caused by the boundary layer formed on the strut, by the formation of the viscous wake at the trailing edge, and by interaction with turbulent velocity fluctuations in the inflow. In the case of boundary-layer excitation, the local pressure field is more or less distributed over the width and span of the beam. This excitation will be altered by changes in the angle of attack of the beam and, possibly, by beam vibration if the modal amplitudes are high enough.

When wake-vortex excitation occurs, the pressures are localized at the trailing edge, and they are often characterized by discrete-frequency excitation. The vortex-induced excitation is most intense when the separation points of the boundary layer are well defined.

A third source of excitation involves the reaction of the beam to turbulence in the inflow. These pressures are induced because of the unsteady local angle of attack generated by the inflow turbulence. The pressures are maximum at the leading edge. A recent investigation by Mugridge (1970),[3] which is an extension of the early theoretical work of

---

[2]Blake, W. K., "Radiation from Free-Free Beams under Influences of Light and of Heavy Fluid-Loading," NSRDC Report 3716 (Nov 1971).

[3]Mugridge, B. D., "The Generation and Radiation of Acoustic Energy by the Blades of a Sub-Sonic Axial Flow Fan Due to Unsteady Flow Interaction," University of Southampton (England) Ph. D. Thesis (Jan 1970).

Reissner (1947),[4] characterizes the unsteady forces affecting an airfoil in terms of the spectrum of inflow turbulence. The results are expected to apply in the current investigation, except when effects of finite thickness become important.

The purpose of the investigation was to measure the flow-induced vibration and damping of a cantilevered strut in water and to compare those findings to theoretical predictions. To assist in the theoretical predictions, a subsidiary wind tunnel experiment was performed to characterize the statistics of the boundary-layer flow field, developed on a rigid, two-dimensional strut of geometrically similar cross section. The air experiment was performed at Reynolds numbers based on a chord near to those experienced in the water test. This measurement provided necessary scaling criteria for use in estimates of the response of a flexible strut to flow. Also in this report, estimates of the dynamical responses of the beams to inflow are compared with measurements. A theoretical discussion precedes a description of the measurements in order to establish normalization factors with which to examine experimental results.

2. AN ANALYTICAL DESCRIPTION OF THE MOTION OF A BEAM IN WATER

FORMULATION OF THE BEAM-VIBRATION FIELD

We will consider the response of a beam to random hydrodynamic pressure fields which are generated on both sides of the beam by any of the three sources outlined previously. The fluid loading in the forms of acoustic, inertial, and unsteady lift pressures are included in the analysis. The basic analysis essentially follows the format of the Lin (1967)[5] normal mode analysis of a linear system when the statistical properties of the excitation are specified. Leehey (1968)[6] and Davies (1969)[7] have used the same approach to estimate the response of panels to boundary-layer turbulence. The relationships which are presented here could be straightforwardly derived by modifying any of the results available in the previously described references. For completeness, however, the basic development has been outlined as follows. The beam motion is a low-frequency limit for the motion of a cantilevered plate for which three sides are free, and the fourth side is clamped. In the experiments described later, both beam and plate modes were encountered.

---

[4]Reissner, E., "On the General Theory of Thin Airfoils for Non-Uniform Motion," National Advisory Committee for Aeronautics TN 946 (Aug 1947).

[5]Lin, Y.K., "Probablistic Theory of Structural Dynamics," McGraw-Hill, Inc., New York (1967).

[6]Leehey, P., "Trends in Boundary Layer Noise Research," Proceedings of the Air Force Office of Scientific Research–University of Toronto, Institute for Aerospace Studies Symposium, Toronto, Ontario, Canada (20–21 May 1968).

[7]Davies, H. G., "Sound from Turbulent Boundary Layer Excited Panels," Massachusetts Institute of Technology Acoustics and Vibration Laboratory Report 70208-2 (Feb 1969).

Figure 1 shows the strut under consideration; it is positioned so that the flow is parallel to the neutral surface and perpendicular to the longest dimension L. The beam has width w and thickness h. Space coordinates in the plane of the neutral surface are designated by $\vec{x}$; time is designated by t. Fluctuating hydrodynamic pressures $p_f(\vec{x},t)$ are generated on each surface, and the pressures on the upper and lower surfaces may or may not be correlated with each other, depending on the manner of flow excitation. Fluid-reaction pressures are generated by the blade motion so that those on the upper and lower surfaces are correlated. In these cases, we let $p_h(\vec{x}, t)$ denote the differential of the flow-dependent hydrodynamic reaction pressures associated with fluid lifts and moments on the surfaces, and we let $p_a(\vec{x},t)$ denote the differential of flow-independent acoustic and inertial reaction pressures on the upper and lower surfaces. We will neglect viscous damping in the theoretical analysis. The equation of motion for the vibration velocity $v(\vec{x},t)$ of the plate of uniform thickness and density is

$$D\nabla^4 v(\vec{x},t) + \rho_p h \beta \dot{v}(\vec{x},t) + \rho_p h \ddot{v}(\vec{x},t) = \dot{p}_f(\vec{x},t) - \dot{p}_h(\vec{x},t) - \dot{p}_a(\vec{x},t) \qquad (1)$$

where ρ_p is the volume density of the strut material, and the dots above symbols denote time derivatives. The stiffness is

$$D = \frac{1}{12} \frac{E h^3}{1 - \sigma^2}$$

where E is Young's modulus, and σ is Poisson's ratio of the strut material. Mechanical damping caused by friction in the clamp, and hysteretic material losses are represented by an *ad hoc* mechanical damping coefficient β. The strut velocity can be decomposed into its generalized time Fourier components

$$V(\vec{x},\omega) = \frac{1}{2\pi} \int_{-\infty}^{\infty} v(\vec{x},t)\, e^{i\omega t}\, dt$$

which are expandable in the normal modes of the strut $\Psi_{mn}(\vec{x})$

$$V(\vec{x},\omega) = \sum_{m,n} V_{mn}(\omega)\, \Psi_{mn}(\vec{x}) \qquad (2)$$

where

$$\int_{-w/2}^{w/2} \int_0^L \Psi_{mn}^2(\vec{x})\, d\vec{x} = L \cdot w \qquad (3)$$

In general, $\Psi_{mn}(\vec{x})$ can be separated into eigenfunctions which are dependent on the coordinates x and z in Figure 1, i.e.

$$\Psi_{mn}(\vec{x}) = \psi_m(z)\phi_n(x) \tag{4}$$

where $\psi_m(z)$ and $\phi_n(x)$ are separate eigenfunctions describing m-th order axial variation and n-th order lateral variation of the (m,n) mode pattern. For slender beams we can simplify our discussions by considering separately those modes which possess node lines either parallel or perpendicular to the long axis of the beam. The former family of modes will be called torsion modes or (o,n) modes; the latter family will be called bending modes or (m,o) modes. The modes that have a combination of these nodal patterns, i.e., (m,n) modes, will be called plate modes. The plate modes were not often encountered in the experimental work, which will be discussed later.

Mode shapes for modes of cantilevered plates have been theoretically calculated as well as measured; a review of the results of many investigations has been given by Leissa (1969).[8] Letting m equal the number of node lines along the width and n be the number of node lines along the length, the modes of a beam can be approximated by the following closed forms*

$$\Psi_{0,1}(\vec{x}) = \frac{2x}{w}\sqrt{3}\left[\psi_0(k_0 z) + \frac{1}{4}\psi_1(k_1 z)\right] \tag{5A}$$

$$\Psi_{0,2}(\vec{x}) = \phi_2(k_2 x)\left[\psi_0(k_0 z) + \frac{1}{4}\psi_1(k_1 z)\right] \tag{5B}$$

$$\Psi_{1,1}(\vec{x}) = \frac{2x}{w}\left[-\frac{1}{4}\psi_0(k_0 z) + \psi_1(k_1 z) + \frac{2}{3}\psi_2(k_2 z)\right] \tag{5C}$$

$$\Psi_{m,0}(\vec{x}) = \psi_m(k_m z) \tag{5D}$$

where $\psi_m(k_m z)$ is the orthogonal set of mode shapes for a cantilevered beam with m node lines normal to its length, and $\phi_n(k_n x)$ is the mode shape for a free-free beam with n node lines normal to its width. The modal wave numbers are given by

---

[8]Leissa, A. Q., "Vibration of Plates," National Aeronautics and Space Administration Report SP-160 (1969).

*Inspection will show that Equations (5) are only approximately normalized according to Equation (3). This is due to the series truncations necessary to obtain the simplified forms. Lack of normalization is most important for the (1,1) mode.

$$k_m = (2m + 1)\,\pi/2L \qquad m > 0$$

and

$$k_n = 0 \qquad 0 \leqslant n < 2$$

$$k_n = (2n - 1)\,\pi/2w \qquad n > 2$$

The generalized time Fourier transform of Equation (1), with subsequent substitution of Equation (2) into Equation (1) gives, using Equation (3)

$$[D k_{mn}^4 + i|\omega|\rho_p h\beta - \rho_p h\omega^2]\, V_{mn}(\omega)$$

$$= \frac{i\omega}{Lw} \int_{-w/2}^{w/2} \int_0^L [p_f(\vec{x},\omega) - p_a(\vec{x},\omega) - p_h(\vec{x},\omega)]\, \Psi_{mn}(\vec{x})\, d\vec{x} \tag{6}$$

where $k_{mn}^2 = k_m^2 + k_n^2$

If we make the advantageous assumption of acoustically uncoupled modes, we can write the acoustic back reaction as a summation over modes, i.e.

$$p_a(\vec{x},\omega) \simeq \sum_{m,n} (r_{mn} + i\omega\, m_{mn})\, \Psi_{mn}(\vec{x})\, V_{mn}(\omega) \tag{7}$$

where, for the (m,n) mode, r_{mn} is the radiation resistance per unit area, and m_{mn} is the entrained fluid mass per unit area. For free-free beams, Blake[2] has shown that

$$r_{m0} \simeq \rho_0 c_0 \left(\frac{2\pi^2}{217}\right) (k_a w)^2 \frac{w}{\pi L} \left(\frac{k_a}{k_m}\right)^2 \tag{8}$$

for $k_a/k_m \ll 1$, and $k_a w < 4$, where k_a is the acoustic wave number. For a clamped-free beam, Equation (8) is likely to be of the correct decimal order of magnitude. The entrained inertia per unit area for beams has been given by Blake for $k_a/k_m \ll 1$ to be

$$m_{m,0} = \rho_0 \frac{\pi}{4} w \qquad k_m w < 1 \tag{9A}$$

$$m_{m,0} = \rho_0 \frac{\pi}{2} w\,(1 + k_a w)^{-1} \qquad k_m w > 1 \tag{9B}$$

Both of these relationships are expected to apply approximately for all of the (m,0) modes considered in the experiments. For modes involving torsion, r_{mn} is likely to be less than that predicted using Equation (7). In using Equation (7), we have assumed that the fluid impedance is locally proportional to the transverse velocity of the strut. In the special case of the torsion (0,1) mode, the fluid inertial impedance is manifested in an entrained moment of inertia, which can be approximated using two-dimensional potential flow relationships. This special case will be further examined at the end of this section.

HYDRODYNAMIC COUPLING AND DAMPING EFFECTS

When there is no mean flow past the beam, the important fluid reactions to motion are acoustic and inertial. The imposition of a mean flow parallel to the plane of the neutral surface (Figure 1) causes additional forces. Given the Fourier component of vertical velocity on the beam surface $V(\vec{x}, \omega)$, the local small angle of attack to the flow of mean velocity U_0 is $V(\vec{x},\omega)/U_0$. This Fourier component of angle of attack generates a generalized unsteady pressure having a major component in phase opposition with $V(\vec{x},\omega)$. Depending on whether the motion is characterized by bending (m,0) modes or by torsion (0,n) modes, this unsteady differential pressure field $p_h(\vec{x},\omega)$ has a chordwise distribution which can provide different relationships between net forces and moments.

The basic two-dimensional theory for the oscillating hydrofoil has been worked out independently by Theodorsen (1935)[9] and by von Kármán and Sears (1938).[10] The theoretical expressions for the more appropriate three-dimensional theory have been derived in closed form by Reissner.[4] The expressions are unwieldly for our purposes, so we will make use of certain closed-form approximations to numerical solutions of the Reissner expressions. These solutions were obtained by Lawrence and Gerber (1952)[11] and were experimentally verified by Laidlaw and Halfman (1956).[12] For the beam (m,0) modes of our problem, a three-dimensional correction to the two-dimensional expressions will be a function of reduced frequency $\omega c/U_0$, where c is the half-width of the beam, and local aspect ratio $AR = \pi/wk_m$. Since the lift and moment distributions are not uniform over the chord of the strut, the flow can induce modal coupling as indicated in the following analysis.

---

[9]Theodorsen, T., "General Theory of Aerodynamic Instability and the Mechanism of Flutter," National Advisory Committee for Aeronautics Report 496 (1935).

[10]von Kármán, T. and W. R. Sears, Journal of the Aeronautical Sciences, Vol. 5, p. 379 (1938).

[11]Lawrence, H. R. and E. H. Gerber, Journal of the Aeronautical Sciences, Vol. 19, p. 769 (1952).

[12]Laidlaw, W. R. and R. L. Halfman, Journal of the Aeronautical Sciences, Vol. 23, p. 117 (1956).

The local hydrodynamic pressure $p_h(\vec{x},\omega)$ can be written

$$p_h(\vec{x},\omega) = \sum_{m,n} \tilde{C}_{m,n}(\Omega) \cdot 2\pi\rho_0 U_0 \ell_{mn}(\vec{x}) V_{mn}(\omega) \Psi_{mn}(\vec{x}) \tag{10}$$

where we have assumed that the pressure is locally proportional to the vertical velocity; however, it is weighted by a chordwise lift-distribution function $\ell_{mn}(\vec{x})$ that depends on the mode of motion. The fluid density is ρ_0; $\tilde{C}_{mn}(\Omega)$, where $\Omega = \omega c/U_0$, we will call the modal oscillatory lift coefficient, which is a function of mode type and of aspect ratio $\pi(k_n w)^{-1}$. Equation (10) can be given more commonplace significance if we consider the special case of two-dimensional translatory motion. This case is approximated in practice by the limit $k_m = k_0 \to 0$. The total lift distribution dL/dz for a two-dimensional strip is given by

$$\frac{dL}{dz} = \int_{-w/2}^{w/2} p_h(x,z,\omega)\,dx = 2\pi\rho_0 w U_0 \quad \tilde{C}_{1,0}(\Omega) \int_{-1/2}^{1/2} \ell_{1,0}(x)\,d\frac{x}{w} \tag{11}$$

where the term in square brackets is the two-dimensional Theodorsen function $C(\Omega)$.[9] Alternatively, for the (0,1) mode of an infinite beam, we have two-dimensional pitch motion for which the spanwise moment distribution is

$$\frac{dM}{dz} = \int_{-w/2}^{w/2} p_h(x,z,\omega)\,x\,dx = \frac{\pi}{16}\rho_0 w^2 U_0 \frac{2\sqrt{3}}{w}\left[\tilde{C}_{0,1}(\Omega) \int_{-1/2}^{1/2} 32\ell_{0,1}(x) \frac{x}{w}^2 d\frac{x}{w}\right] \tag{12}$$

where the term in square brackets is $[1 - C(\Omega)]$; see Sears (1940).[13] The high-frequency limit of $C(\Omega)$ is $\lim_{\Omega\to\infty} C(\Omega) = 1/2$.

If we substitute Equations (7) and (10) into Equation (6), we can see that the effect of $\ell_{mn}(x)$ is to couple modes, if $\ell_{mn}(x)$ is not independent of x. We obtain

$$z^0_{mn}(\omega) V_{mn}(\omega) = P_{mn_f} - \sum_{i,j} 2\pi \tilde{C}_{ij}(\Omega)\rho_0 U_0 V_{ij}(\omega)$$

$$\cdot \frac{1}{Lw} \int_{-w/2}^{w/2} \int_0^L \ell_{ij}(x)\ \psi_{ij}(x,z)\,\psi_{mn}(x,z)\,dx\,dz \tag{13}$$

---

[13] Sears, W. R., Journal of the Aeronautical Sciences, Vol. 8, p. 104 (1940).

where

$$z^0_{mn}(\omega) = (i\omega)^{-1}\left[D k^4_{mn} - \omega^2(\rho_p h + m_{mn}) + i|\omega|(\rho_p h\beta + r_{mn})\right]$$

and we have written

$$P_{\substack{mn\\f}} = \frac{1}{Lw}\int_{-w/2}^{w/2}\int_0^L p_f(\vec{x},\omega)\,\Psi_{mn}(\vec{x})\,d\vec{x}$$

The (m,0) modes can be coupled with types (m,1) modes because a heaving motion of the beam produces a moment as well as a lift, and a pitching motion of the beam produces a lift as well as a moment. The first two factors of the summation term of Equation (13) can be written as

$$P_{\substack{m,0\\h}} = i\omega\rho_0 2\pi\left\{V_{m,0}(\omega)\,\tilde{C}_{m,0}(\Omega)\frac{1}{w}\int_{-w/2}^{w/2}\ell_{m,0}(x)\,\phi_0(x)\,\phi_0(x)\,dx\right.$$

$$\left. + V_{m,1}(\omega)\,\tilde{C}_{m,1}(\Omega)\frac{1}{w}\int_{-w/2}^{w/2}\ell_{m,1}(x)\,\phi_1(x)\,\phi_0(x)\,dx\right\} \tag{14}$$

where we have used Equation (4). To evaluate approximately the relative sizes of the modal amplitudes $V_{m,0}(\omega)$ and $V_{m,1}(\omega)$, we note that Equation (13) can be evaluated at the resonance frequency of the (m,0) mode $\omega_{m,0}$ for $U_0 = 0$ so that

$$\frac{V_{m,1}(\omega_{m,0})}{V_{m,0}(\omega_{m,0})} \approx \eta\left[\frac{\omega^2_{m,0}}{\omega^2_{m,1} - \omega^2_{m,0}}\right]$$

Here we have assumed that the $P_{\substack{mn\\f}}(\omega)$ are of comparable magnitude, and we have let

$$|\omega|\,\eta = \frac{\beta\rho_p h + r_{m,0}}{\rho_p h + m_{m,0}}$$

where $\eta \ll 1$ is the loss factor of the (m,0) mode in still water. With flow, the loss factor increases, but if it remains very much less than unity, the ratio of the torsional modal amplitude to the bending modal amplitude is still likely to be very small when $\omega_{m,1}$ and $\omega_{m,0}$ are sufficiently different. Furthermore, in the case of $\Omega > 1$, $C(\Omega)$ and $[1 - C(\Omega)]$ are both approximately one-half so that both coefficients of the modal amplitudes in Equation (14) are of a similar decimal order of magnitude. Thus for light damping, for which $\eta < 1$, for speeds low enough that $\Omega > 1$, and for $\omega_{m,1}$ considerably different than $\omega_{m,0}$, this type of modal coupling can be neglected.

Equation (13) as it applies to beam modes now becomes

$$\left\{ D k_{m,0}^4 - \omega^2 (\rho_p h + m_{m,0}) + i|\omega| [r_{m,0} + \pi \rho_0 U_0 C_{m,0} (\Omega)] \right\} V_{m,0}(\omega)$$

$$= i \omega P_{\substack{m,0 \\ f}} (\omega) \tag{17}$$

The lift function $C_{m,0}(\Omega)$ now incorporates the integrated lift-distribution function; it still includes a three-dimensional effect, and it parallels the expression of Sears.[13] The lift function accounts for spanwise load variation but neglects the overall finite length L of the beam. For example, for large L, $C_{0,0}(\Omega)$ is just the Theodorsen function. Resonance conditions for the lightly damped, clamped-free beam in flow occur at all frequencies for which $D k_m^4 - \omega_m^2 (\rho_p h + m_m) = 0$. The second index in the subscript will hereafter be dropped when beam modes are considered. The total loss factor η_t under flow conditions is then

$$\eta_t = \frac{r_t}{\omega(\rho_p h + m_m)} = \frac{\rho_p h \omega \eta_m + r_m + \pi \rho_0 U_0 C_{m,0} (\Omega)}{\omega (\rho_p h + m_m)} \tag{18}$$

where m_m is given by Equation (9),

β has been replaced by $\omega \eta_m$, and

η_m is the mechanical loss factor.

Equation (18) shows that as U_0 is increased, the hydrodynamic damping increases. It is pertinent to note here that flow effects on the added mass are neglected, since they occur only at reduced frequencies less than unity. Furthermore, the calculations of Lawrence and Gerber[11] show that the three-dimensional effects of structural vibration make the flow contribution to entrained inertia even more insignificant.

A hydrodynamic loss factor can be defined in terms of the hydrodynamic resistance and entrained inertia

$$\eta_H = \frac{\pi \rho_0 U_0 C_{m,0} (\Omega)}{\omega m_m} \tag{19}$$

For $k_m w < 1$ the entrained mass is given by Equation (9A), and $C_{m,0}$ can be approximated by its two-dimensional value $C_{m,0}(\Omega) \simeq 1/2$ for $\Omega > 1$, and $\pi / k_m w >> 1$, so that

$$\eta_H = 1/\Omega \tag{20}$$

is a limiting value for low-order modes. At low-aspect ratio, i.e., $\pi/k_n w < 1$, we can use the Lawrence and Gerber[11] small-aspect-ratio approximation to give

$$C_{m,0} \simeq \pi/2k_m w$$

and combine this with Equation (9B) to give

$$\eta_H = 1/2\ \Omega \tag{21}$$

for high-order modes at high reduced frequencies.

In the case of torsion (0,n) modes, a similarly defined hydrodynamic loss factor is obtained by using the Sears[13] two-dimensional moment function. The flow-induced resistance to the angular velocity of the section, e.g., $r_{0,1}$, must be normalized by the entrained moment of inertia per unit area, i.e., we can define a loss factor using Sears[13] expressions

$$\eta_H = \frac{r_{0,1}}{\omega I_f} = \frac{\pi/16\,\rho_0^2\ c^2\ U_0}{\left[\omega\ \pi/128\,\rho_0\, w^3\right]} = \frac{2}{\Omega} \tag{22}$$

This is just double the two-dimensional loss factor induced by the bending motion. The ratio of the resonance frequency of the (0,1) mode in water to that in air is just the square root of of the ratio of I_B to $I_B + I_f$, where $I_B = \rho_p h \cdot c^2/12$. Thus

$$\frac{\omega_{wet}}{\omega_{dry}} = \left[\frac{I_B}{I_B + I_f}\right]^{1/2} \tag{23}$$

RESPONSE OF THE WATERLOADED BEAM TO A RANDOM PRESSURE FIELD

We will assume that the hydrodynamic excitation pressure fields on each side of the strut are uncorrelated with each other. Thus, the response of the strut to large-scale inflow turbulence is not identically given by the following analysis; that case will be discussed in Chapter 5. The generalized time transform of $p_f(\vec{x},t)$ is a stochastic variable as well as its generalized modal coefficient $p_{m,0}(\omega)$, which is used in Equation (17) and is defined following Equation (13). The modal velocity coefficient $V_{mn}(\omega)$ is also a stochastic variable. We will assume statistical stationarity and ergodicity in regard to time-averaging. The auto-spectral density of the vibration velocity measured at a location $\vec{x}_0$ on the strut is, using Equation (2),

$$\begin{aligned}\phi_w(\omega, \vec{x}_0) &= 2\pi\ \langle V(\vec{x}_0,\omega)\ V^*(\vec{x}_0,\omega)\rangle \\ &= 2\pi \sum_{m,n} \langle V_{mn}(\omega)\ V^*_{mn}(\omega)\rangle\ \Psi^2_{mn}(\vec{x}_0)\end{aligned}$$

where the brackets ($\langle\ \rangle$) denote an ensemble average.

Using Equation (17) we have for the local autospectral density of velocity

$$\phi_{vv}(\omega,\vec{x}_0) = 2 \sum_{m,n} \frac{\Psi_{m,n}(\vec{x}_0)}{|z_{mn}(\omega)|^2} \frac{1}{A_s^2} \int_{A_s}\int_{A_s} \phi_p(\vec{x},y,\omega)\Psi_{mn}(\vec{x})\Psi_{mn}(\vec{y})d\vec{x}\,d\vec{y} \tag{24}$$

where the total impedance

$$z_{m,n}(\omega) = \left[D k_{mn}^4 - \omega^2(\rho_p h + m_m) + i\omega^2(\rho_p h + m_m)\eta_t\right](i\omega)^{-1}$$

includes the fluid reaction, and the cross spectral density of surface pressure is

$$\phi_p(\vec{x},\vec{y},\omega) = 2\pi\langle p_f(\vec{x},\omega)p_f^*(\vec{y},\omega)\rangle$$

The factor 2 outside the summation accounts for the decorrelation of the upper and lower surfaces. The summation is technically over all modes which are excited at frequency ω. Also in Equation (24) we have replaced Lw by A_s, denoting an area integration. The surface pressure-cross spectral density depends on both points of measurement $\vec{x}$ and $\vec{y}$. As is discussed in the next section, it may be measured with pairs of pressure sensors. In such an experiment, the cross spectral density of pressures, measured at locations $\vec{x}$ and $\vec{y} = \vec{x} + \vec{r}$, is obtained.

We will simplify our discussions by expressing the pressure cross spectrum in a separable form

$$\phi_{pp}(\vec{x};\vec{r},\omega) = \overline{p^2(x)}\,\Phi(\omega)\,e^{-|r_x|/\lambda_x}\,e^{-|r_z|/\lambda_z}\,e^{-i\frac{r_x\omega}{U_c}} \tag{25}$$

In this expression $\overline{p^2(x)}$ is the mean-square pressure at a chordwise coordinate x, and $\Phi(\omega)$ is its autospectrum. The pressure field is convected chordwise across the strut at a speed U_c. The λ_x and λ_z are each one-half of the chord- and spanwise-integral correlation lengths of the pressure. The motivation for selecting this functional form comes from the theories of boundary-layer excitation. Specifically, Corcos (1964)[14] has suggested the model for the pressure cross spectrum as long as the statistics of the pressure field are homogeneous in space $\vec{x}$. We may expect Equation (25) to apply approximately if the field is homogeneous within a correlation area $2\lambda_x\,2\lambda_z$.

[14]Corcos, G.M., Journal of the Acoustical Society of America, Vol. 35, p. 192 (1964).

In the case of discrete vortex excitation, an alternative form of Equation (25) is necessary to account for the localization of pressure at the trailing edge. However, in the experiments singing did not occur so that case will not be considered.

For the flow excitation of the cantilevered strut, the statistics are uniform over the spanwise direction as long as the turbulent flow field is unaffected by strut vibration. The pressure field is expected to change with chordwise distance x from the leading edge because of the growth of the boundary layer on the strut. Near the trailing edge, where the upper and lower surfaces converge, the static pressure gradient is adverse, causing a more pronounced thickening of the boundary layer in that region. Because of the spatial nonstationarity of the flow field, we can only approximately evaluate Equation (24) with Equation (25). For the cases that $\lambda_x/w << 1$, and $\lambda_z k_m << 1$, the integrals over r_x and r_y may be approximated, giving for beam modes

$$\phi_{vv}(\omega,z_0) \simeq 2\sum_m \frac{\psi_m^2(z_0)}{|z_m(\omega)|^2} \frac{4\bar{\lambda}_x\bar{\lambda}_z}{A_s} \int_{-1/2}^{1/2} \overline{p^2}(\vec{x}) \frac{\Phi(\omega)}{1+(\omega\lambda_x/U_c)^2} \, d\frac{x}{w} \tag{26}$$

where $2\bar{\lambda}_x$ and $2\bar{\lambda}_z$ are the integral correlation lengths of the pressure field averaged over the area of the strut. If we have measurements of the mean-square pressure with its correlation area and autospectrum, we can estimate the modal response of the (m,0) mode of the beam, knowing the total loss factor of the beam. The autospectral density for the local acceleration of the (m,0) mode at resonance is

$$\phi_{\substack{AA\\m}}(\omega,z_0) = 2\frac{\psi_m^2(z_0)}{[\rho_p h + m_m]^2\eta_T^2} \cdot \frac{4\bar{\lambda}_x\bar{\lambda}_z}{A_s} \int_{-1/2}^{1/2} \overline{p^2}(x) \frac{\Phi(\omega)}{1+(\omega\lambda_x/U_c)^2} \, d\frac{x}{w} \tag{26B}$$

In Chapter 3 we will outline the measurement of the statistics of the pressure field; in Chapter 4 we will discuss measurements of the actual flow-induced–beam-vibration levels in a water tunnel and, finally, in Chapter 5 we will compare those levels to those which are estimated, using Equation (26B) and the statistics of the pressure field obtained in the wind tunnel.

3. WIND TUNNEL INVESTIGATION OF THE FLUCTUATING PRESSURE FIELD

A survey of the turbulent boundary-layer mean and fluctuating-velocity profiles was made in conjunction with two-point, longitudinal and lateral wall-pressure, cross spectral densities. The measurements were performed in air for zero and a 2-deg angle of attack.

The purpose of this investigation was to determine the pressure-field statistics and to ascertain which parameters may be used in scaling the wind tunnel results to make predictions for the water tunnel experiment, described in a later section.

DESCRIPTION OF EXPERIMENT

The boundary-layer investigation was performed on a strut. Figure 2a shows the cross-section. The strut was 4-ft in length with a thickness of 2 in. and chord of 22 in. It was positioned between two end plates to insure two-dimensionality of the mean flow. Mean and turbulent velocity profiles were measured at the lettered positions shown in Figure 2a. Auto and cross spectral densities of wall pressure were measured at Positions A through D on the strut. A complete description of the experimental technique and instrumentation has been given by Blake and Dwyer (1973);[15] only an outline will be given here.

Velocity measurements were made with a Thermosystems 1010A hot wire anemometer, used with a Thermosystems 1005B linearizer. The anemometer probe was continuously traversed in directions normal to the strut. Incremental movement of the probe could be made in 0.01-in. steps. The error in absolute positioning was generally about 0.02-in. because there was no satisfactory means of determining a positioning datum under flow conditions without damaging the probe. Using the linearized-voltage outputs, the velocity profiles could be directly normalized on the mean voltage corresponding to the free-stream velocity. The boundary-layer thickness has been defined as the distance from the wall for which the mean linearizer voltage is 0.99 of the mean voltage corresponding to the local free-stream velocity. Normalized mean velocities, which are determined directly from the linearized mean voltages, are in error by less than 10 percent, when $U/U_\infty \approx 0.5$, and by less than 20 percent, when $U/U_\infty \approx 0.25$. These errors are basically determined by the deviation of the relationship between velocity U and voltage V from King's law, which states

$$V^2 - V_0^2 = A\sqrt{U}$$

The anemometer voltage at $U = 0$ is V_0, and A is a constant. The linearizer adjustments were set under the assumption that King's law holds.

Fluctuating-pressure measurements were made with Bruel and Kjaer (B & K) 4138 microphones, which had been fitted with pinholes one-thirty second of an inch in diameter. The pinhole reduced the sensitive area of the microphone and caused cavity resonance at

[15] Blake, W. K. and R. D. Dwyer, "A Statistical Description of the Pressure and Velocity Fields at Trailing Edges of Flat Struts," NSRDC Report 4241 (1973).

approximately 17 kHz. The microphones were connected to B & K 2619 cathode followers, using the B & K UA 0123 flexible right-angle adaptors, which had been custom-fitted with a special 1/8-in. fitting for the microphone. The complete microphone system was acoustically calibrated in a free field by comparison with another microphone of known sensitivity. The calibration was reliable to ± 1 dB.

Spectral analysis was performed online, using a Time Data TD 90A fast Fourier processor. The effective bandwidth of analysis ranged from 12 to 64 Hz with total numbers of independent samples ranging from 256 to 1000. This number of samples made the statistical precision on spectral densities well within ± 10 percent.

MEAN AND TURBULENT VELOCITY PROFILES

Boundary-layer surveys were made at selected Positions A through G on the strut and in the wake of the strut. Measurements were obtained with angles of attack α at 0 and 2 deg. When the strut was set at an angle of attack, the measurements were made on the low static pressure side of the strut. Figure 3 shows normalized mean-velocity profiles, measured at Positions C through F. The mean velocities are normalized on the local free-stream velocity; distance from the wall is normalized on the local boundary-layer thickness. The dotted line in Figure 3 is a mean-velocity profile, measured by Blake and Dwyer[15] on a similarly shaped strut. That strut was of the same thickness; however, it had a much longer parallel section than the strut considered here. This profile was measured in nearly zero pressure gradient at 60 ft/sec and a distance from the leading edge roughly corresponding to just forward of Position C on the strut considered here. Comparison of the zero pressure-gradient profile with those measured at Position C shows the effects of the adverse pressure gradient imposed on the flow after the knuckle. Profiles measured at points downstream of Position C show further effects of the adverse pressure gradient; the mean velocity near the wall continues to be retarded; however, flow separation was not observed. Profiles measured at 50 and 100 ft/sec inflow appear to be similar when scaled in the manner of Figure 3; however, profiles at different streamwise locations are notably dissimilar because of rapidly changing static pressure.

A flow-visualization experiment in which the strut was painted with a mixture of linseed oil and titanium dioxide disclosed a small separated-flow region at the leading edge. The region had a streamwise extent of approximately h/2, h being the strut thickness. The separation bubble was centered on the point at which the circular leading edge was faired into the parallel sides of the strut. The flow visualization disclosed no other separation regions on the strut; this was in agreement with the anemometer measurements.

Profiles of turbulence intensity, measured on the strut at $\alpha = 0°$, are shown in Figure 4. They generally reflect the effects of the adverse pressure gradient on the tapered section of the strut. Figure 4a shows a profile obtained in an adverse pressure gradient by Schloemer (1967)[16] for qualitative comparison. At all stations of measurement, as well as in the Schloemer result, the intensities are peaked near $y/\delta \simeq 0.2$ to 0.3. The measurements at Position C were made at Reynolds numbers based on mean-in-flow velocity U_0 and on local momentum thickness $N_{R_{e\theta}} = U_0\,\theta/\nu$ on the order of 2.5×10^3; the Schloemer measurement was made at $N_{R_{e\theta}} \simeq 9180$. We have used the conventional definition of momentum thickness

$$\theta = \int_0^\infty \frac{U}{U_\infty}\left(1 - \frac{U}{U_\infty}\right) d\left(\frac{y}{\delta}\right)$$

The large difference in Reynolds numbers restricts the quantitative comparison of the Schloemer results with the current ones. The results of Figure 4 also show a slight, but consistent, reduction in the peak-turbulence intensities as the mean velocity is increased.

When the strut was set at $\alpha = 2°$, the boundary-layer growth on the low-pressure side of the strut was considerably altered. Figure 5 shows mean-velocity profiles, measured at Positions A, C, and F at 25 and 50 ft/sec. Higher velocities were not used because the strut was a lifting surface. The slight angle of attack produced a more severely adverse pressure gradient, resulting in a much-thickened boundary layer. Furthermore, the normalized velocity profiles are not as well-scaled using displacement thickness and free-stream velocity. The profiles measured at Position A are particularly dissimilar.

A flow-visualization experiment at 50 ft/sec disclosed an extensive separated-flow region at the leading edge on the suction side of the strut. The associated separation bubble appeared to extend about two strut thicknesses downstream of the leading edge. There were no other separated-flow regions on the strut.

Figure 6 shows higher levels of turbulence intensity profiles than those at $\alpha = 0°$. At Position A, we note the high-intensity region extending to $y/\delta \simeq 0.4$; the normalized intensities are lower at 50 ft/sec than at 25 ft/sec. This speed dependence is more pronounced here than at other positions at either $\alpha = 0°$ or $\alpha = 2°$. The high intensities at Position A, therefore, may be determined by leading-edge separation, and the pronounced speed dependence of both the mean and the turbulent intensities probably reflects the influence of speed on the size and strength of the separated flow. Further downstream, e.g., at Position C, normalized intensities are still higher at $\alpha = 2°$ than at $\alpha = 0°$; however, the speed dependence is more similar

[16] Schloemer, H.H., Journal of the Acoustical Society of America, Vol. 42, p. 1 (1967).

to that observed at 0 deg. The intensities in the near wake at Position F were measured on both sides of the strut. The lack of symmetry reflects the effect of angle of attack. On the pressure side of the strut, the intensity profiles at 0 and 2 deg are similar. The boundary-layer thicknesses at this location at 50 ft/sec are 1.1 in. for $\alpha = 0°$ and 1.06 in. on the pressure side for $\alpha = 2°$. On the suction side at 50 ft/sec and $\alpha = 2°$, the boundary-layer thickness is 2.05 in. Thus the boundary-layer characteristics on the pressure side appear to be quite unaffected by the small change in angle of attack, while the boundary layer on the suction side is dramatically altered.

Figure 7 gives displacement thickness δ^* measurements. The displacement thickness is calculated from the measured mean-velocity profiles by

$$\frac{\delta^*}{\delta} = \int_0^\infty \left(1 - \frac{U}{U_\infty}\right) d\left(\frac{y}{\delta}\right) \tag{27}$$

We note the generally higher values of δ^* at $\alpha = 2°$ than at $\alpha = 0°$. Table 1 gives mean-velocity parameters for the strut.

Wall-shear coefficients, defined as

$$C_f = \tau_w / q$$

where τ_w is the mean local wall shear, were determined from the mean-velocity profiles. The mean-velocity profiles were curve fitted to Coles' (1956)[17] law of the wall,

$$\frac{U}{U_\tau} = 5.75 \tag{28}$$

where U is the local mean velocity,

U_τ is the friction velocity, and

ν is the kinematic viscosity of air.

The friction velocity is related to C_f by $U_\tau / U_\infty = (C_f/2)^{1/2}$. Wall-shear coefficients obtained in this manner are subject to the assumption that the law of the wall applies in some region of the boundary layer close to the wall. Even in severely adverse pressure gradients, Coles[17] has shown Equation (28) to apply. Some of the mean-velocity profiles of Figures 3 and 5 have been replotted in Figure 8. The spread in the data suggests an uncertainty in calculated C_f values of at least 20 percent. The values are shown in Table 1. In the trailing-edge region, C_f is nearly independent of position; it is reduced by a factor of 1.35 for a factor of 2

[17]Coles, D., Journal of Fluid Mechanics, Vol. 1, p. 191 (1956).

increase in speed. This suggests a speed dependence of $U_0^{0.4}$. At $\alpha = 2°$, the speed dependence of C_f is less, and this would imply a weaker Reynolds number dependence than at $\alpha = 0°$. We note at this point that all turbulence intensities peak at approximately $y/\delta \simeq$ 0.2 to 0.3. This roughly corresponds to $yU_\tau/\nu \simeq 250$ for most measurement cases. The mean-velocity profiles of Figure 8 indicate that this coordinate separates the law-of-the-wall region from the wake region of the boundary layer where the profile deviates from Equation (28). Also, an examination of Figures 3 and 5 shows that the vertical gradient of mean velocity $d(U/U_\infty)/d(y/\delta)$ diminishes in most cases for $y/\delta > 0.3$. Thus the high intensities are restricted to the constant stress or law-of-the-wall region of the boundary layer where the mean velocity gradient is highest and where the local mean velocity U is less than approximately 0.8 U_∞.

STATISTICS OF THE SURFACE PRESSURE FIELD

Autospectral densities of wall-pressure fluctuations were measured at Positions A through D at $\alpha = 0°$ for 50 and 100 ft/sec. The spectra are nondimensionalized on inflow speed U_0, dynamic head of the inflow $q_0 = 1/2\, \rho_0 U_0^2$, and δ^*; these variables collapse the spectra within 3 dB as shown in Figure 9. This spread in the dimensionless spectra is about double that shown by measurements in other facilities; however, the pressures measured on the strut are subject to a changing pressure gradient. Thus, in the present case, a unique dependence of the spectra on dynamic head and displacement thickness is unlikely. Schloemer[16] has shown a substantial dependence of the spectra on pressure gradient; the effects of an adverse pressure gradient are more severe than the effects of a favorable one. In the present case, we have normalized the spectra at Position C on the local wall shear τ_w; the right-hand ordinate on Figure 9 applies to this normalization. The dotted line in Figure 9 represents the wall-pressure spectra, normalized on τ_w, measured on a wind tunnel wall by Blake (1970).[18] Throughout most of the frequency range, the wind tunnel spectrum is of a level comparable to the spectrum measured at Position C, and the spectrum shapes are nearly parallel. At high frequencies, deviation of the spectrum shapes is caused by spatial averaging of the pressure field over the microphone face. Corcos[14] has shown that if U_c is the speed of convection of the pressure field across the microphone, and if R_m is the microphone radius, the pressure measurement is attenuated by roughly 3 dB at $\omega R_m/U_c \simeq 1$. We consider this to be the upper limit of the nonaveraged spectrum. If, in anticipation of later results, we let $U_c = 0.7U_0$, and since $2R_m \approx 0.03$ in., we find $\omega\delta^*/U_\infty = 4.6$ corresponds to the upper limit of

[18]Blake, W. K., Journal of Fluid Mechanics, Vol. 44, p. 637 (1970).

the nonaveraged spectrum at Position C. Thus the band limiting of the autospectra in Figure 9 for $\omega\delta^*/U_0 > 5$ is attributed to geometric microphone-size averaging rather than a nature of the flow.

The results show that over the downstream half of the strut, the autospectra are well described by the wall shear, δ^*, and U_0, and they are similar to those measured in boundary layers at higher Reynolds numbers with and without pressure gradients.

The autospectra of pressure measured at Position A with $\alpha = 2°$ are shown in Figure 10 for $U_0 = 25$ ft/sec, and $U_0 = 50$ ft/sec. The autospectra for this position scale well on speed and displacement thickness; however, the low-frequency, dimensionless spectrum levels are about 10 dB higher than those observed at all positions for $\alpha = 0°$. Using the criterion that was applied to Figure 9, microphone-size effects occur in the spectrum for $\omega\delta^*/U_0 > 7$. Autospectra measured at other positions for $\alpha = 2°$ are shown in Figure 11. The spectrum for Position A is shown with dashes for comparison. The spread of dimensionless spectra is greater than for $\alpha = 0°$, and low-frequency spectrum levels appear to diminish as the measurement point is moved further downstream and as the flow speed is increased. It is likely that upstream positions are influenced by the leading-edge, separation region which causes large-scale, turbulent eddies to be convected downstream. Recall from flow visualization that the angle of attack increased the extent of the leading-edge, flow separation. As the flow becomes influenced by the converging surfaces near the trailing edge, the influence of the leading-edge separation is less important. The spectra for $\omega\delta^*/U_\infty > 1$ are nearly similar for both values of α, except for possible microphone size attenuation effects, which are apparent at $\omega\delta^*/U_0 > 5$, and $\alpha = 0°$, and $\omega\delta^*/U_0 > 7$ for $\alpha = 2$.

Two-point, cross spectral densities were measured with different streamwise separations for both angles of attack. We will adopt the representation of the cross spectrum originally suggested by Corcos[14] and will normalize the magnitude of the cross-spectrum $|\phi(r_1,0,\omega)|$ on the auto-spectrum $\Phi_p(\omega)$. The magnitudes, therefore, represent a coherence. Here we have let r_1 be the streamwise separation distance. The normalized magnitudes will be presented as a function of the measured phase $\gamma(r_1,\omega)$, which depends on both frequency and separation. Figure 12 shows results at $\alpha = 0$; the spectra were measured at Positions A and C, and the microphone separations were referred to either of those positions. Upstream separations are designated negative; downstream separations are designated positive. Measurements were made at both 50 and 100 ft/sec. For phases greater than three, the cross-spectrum magnitudes for all speeds and separations are generally described by the phase alone. For phases less than three, the magnitudes are also functions of the reference location of the measurement as well as the separation. The magnitude of the cross spectrum is slightly less than that measured by Blake[18] on a smooth wall in zero pressure gradient. The lower magnitudes are most likely the result of the adverse gradient extant on the strut; such an effect has been studied by Schloemer.

The longitudinal cross-spectrum measurements for $\alpha = 2°$ are shown in Figure 13. For phases greater than two, the data are scattered; however, there is no consistent dependence on separation or measurement location. The magnitudes are also less than those measured on the smooth, wind tunnel wall in zero pressure gradient. At low phases, the magnitude of cross spectral density is a function of both separation and the position of reference.

The cross-spectrum phase has been interpreted by Corcos[14] as

$$\gamma_1 (r_1, \omega) = \omega r_1 / U_c$$

where U_c is the speed of convection of a pressure component of frequency ω over the distance r_1. The convection velocities are shown in Figure 14 for 0- and 2-deg angle of attack. For $\omega\delta^*/U_\infty > 0.3$, U_c/U_0 is nearly a constant independent of separation. The data for a 2-deg angle of attack show slightly more scatter for $\omega\delta^*/U_\infty < 0.75$. At very low frequencies, $U_c/U_0 > 1$ at Positions A and C. For very low frequencies and large separations at the trailing edge, U_c/U_0 approaches 0.5. The convection velocities at high frequencies approach from 0.6 to 0.7 U_0. Assuming that the pressure-producing eddies are convected at the local mean velocities; these values of U_c place the eddies which dominate the high-frequency spectrum at $y/\delta \simeq 0.1$. The eddies which dominate the low-frequency spectrum are convected at speeds greater than the inflow speed U_0, and they generate a coherent pressure field as evidenced by the high values of cross spectral density at low phase.

The measurements reinforce the suggestion that the low-frequency field is generated by the leading-edge separation with eddies convected at a velocity nearly equal to and sometimes larger than the local free-stream velocity. The low-frequency pressure field is affected by changes in mean angle of attack. The high-frequency pressure field is locally generated by slowly convected eddies within the constant stress region of the boundary layer. The pressures occurring for $\omega\delta^*/U_0 > 1$ are only slightly affected by angle of attack.

The lateral cross spectral density measurements are normalized on the autospectrum. Frequency is normalized on r_3, and we take $U_c \simeq 0.7\ U_0$. The results are shown in Figure 15. For phases $\omega r_3/U_0 > 1$, the spectral density is similar to that obtained on a wind tunnel wall by Blake.[18] At low frequencies the coherence is somewhat reduced from that observed in wind tunnels, and an additional dependence on separation appears.

The separate eddy fields appear to be characterized by separate coherence behavior. At higher frequencies the coherence appears dependent on $\omega r_1/U_c$ and $\omega r_3/U_c$. At lower frequencies, those apparently dominated by the separated flow at the leading edge, the coherence depends more on the microphone separation than on frequency. Figure 16 rather dramatically illustrates the dual behavior of the cross spectra. Frequency has been normalized

on the strut thickness h and on U_0. The ordinate is 20 log $|\phi(r_1, 0, \omega)| / \Phi_p(\omega)$. At low frequencies, the coherence for a given separation is dramatically increased for angles of attack. At $\alpha = 2°$, the low-frequency coherence is more a function of separation than of frequency; it is describable as

$$|\phi(r_1, 0, \omega)| / \Phi_p(\omega) \simeq e^{-r_1/\delta^*/13.7} \qquad \frac{r_1}{\delta^*} < 15, \frac{\omega h}{U_0} < 4 \tag{29A}$$

Also, the lateral cross spectral density is described by

$$\phi(0, r_3, \omega) / \Phi_p(\omega) \simeq e^{-r_3/\delta^*/2.9} \qquad \frac{r_3}{\delta^*} < 9, \frac{\omega h}{U_0} < 4 \tag{29B}$$

At high frequencies, the spectra are describable as

$$|\phi(r_1, 0, \omega)| / \Phi_p \simeq e^{-a_1(\omega r_1/U_c)} \tag{30A}$$

and

$$\phi(0, r_3, \omega)/\Phi_p(\omega) \simeq e^{-a_3(\omega r_3/U_c)} \tag{30B}$$

where a_1 and a_3 are determined from curve fitting Figures 12, 13, and 15.

The results of the wind tunnel investigation will be scaled to estimate the pressure field developed on an identically shaped strut, studied in a water tunnel. Tentatively based on the wind tunnel results alone, the autospectral density of wall pressure appears to be determined by dynamic head at low frequencies, which are domintaed by leading-edge separation, and by wall shear at the higher frequencies, which are dominated by the local inner boundary layer. Displacement thickness and inflow velocity appear to scale the frequency. The coherence of the pressure field has two separate descriptions given by Equations (29) and (30).

4. WATER TUNNEL INVESTIGATION OF THE DAMPING AND VIBRATION OF A BEAM IN FLOW

This segment of the investigation was directed at measuring the flow-induced damping and vibration of a series of cantilevered beams in water.

DESCRIPTION OF EXPERIMENT

Description of Test Specimens

The cantilevered beams were generally 20 in. long and were of varying widths. One beam was 1.5 in. wide and 14 in. long. The beams protruded from the clamp through a 6-in., dead-water region into the open jet of the water tunnel. A typical cross section of the beams is shown in Figure 2b; the overall width is designated w. The section consisted of a circular leading edge of 0.125-in. radius, followed by a 1/4-in.-thick parallel section of variable length 1 ft. The trailing edge was a wedge with a 12.5-deg included angle. The length of the wedged section was 1.0 in. for all beams. The widths of the beams were varied by changing 1 ft; they were 1.5, 2.75, and 5.0 in. The beams were stainless steel.

Water Tunnel and Damping Fixture

The measurements were made in the 12-in., variable pressure water tunnel at the Naval Ship Research and Development Center. The cylindrical test section of the tunnel was 37 in. long and 30 in. in diameter with a 24-in.-diam access hatch, located on the top side of the test section. Concentric with the test section were a 9 1/4-in.-long entrance nozzle and a 16-in.-long exit nozzle both 12-in. in diameter; thus was produced a horizontal cylindrical jet, approximately 12 in. in diameter and 12 in. long, in which to conduct the experiment.

The clamping assembly used to hold the beams in the waterjet is shown schematically in Figure 17. Extending down 13 3/4 in. from the top access hatch cover were four 1 1/4-in. angle-iron brackets at the bottom of which were attached two 1 1/4- by 13 3/4-in. angle-iron, horizontal cross members. A 190-lb, mass-clamp system—consisting of a 10- by 10- by 7-in. stainless steel block weighing 185 lb and a 2- by 5- by 5-in. clamping block weighing 5 lb, similar in design to that used by Kerlin and Snowdon (1970)[19]—was mounted on the two cross members by means of three cylindrical vibration mounts from Barry Controls, Type A32-051. The system had resonant frequencies of 12 Hz ±42 percent in the vertical direction and 5 Hz ± 16 percent in the horizontal direction. These frequencies were estimated, using stiffnesses provided in the data sheet supplied with the vibration mounts.

Extending down vertically from the clamping block, the beams were clamped rigidly with a root depth of 5 in. between the blocks, using six 3/8-16 cap screws tightened to 40 ft lb. The cap screws were always tightened to the same torque in order to insure, as nearly as possible, the same boundary condition for all beam specimens. Mounted 6 in. from the clamped end of the beam was a 0.38-in.-diam, 0.5-in. long, 7-g Wilcoxon Research Model 165 accelerometer with a sensitivity of 9 mV/g ± 1 dB.

---

[19]Kerlin, R.L. and J.C., Snowdon, Journal of the Acoustical Society of America, Vol. 47, p. 222 (1970).

Vibration Analysis

Accelerometer signals were carried by low-noise coaxial cable, which passed through a packing-gland seal in the test-section wall. The signals were then amplified by an Ithaco Model 257-A preamplifier and were processed in either of two ways. On one hand, spectral densities of acceleration were obtained, using a General Radio (GR) Model 1900-A wave analyzer with a 3-Hz-bandwidth filter. Spectra were recorded on a GR Model 1521-B graphic level recorder. On the other hand, damping measurements were obtained by filtering decaying acceleration levels, using a Bruel and Kjaer (B & K) audiofrequency spectrometer Type 2111, and by recording the filtered levels on a B & K Type 2305 graphic level recorder. Loss factors for modes were determined from the 1/3-octave-band, 60-dB decay times resulting from the response of the beam to the impulses received from a mechanical impulse generator. The structural mode densities of the beams were small enough that a 1/3-octave-measurement band, centered on a given mode, did not include more than a single beam mode.

Mode shapes of the beams in still water were measured, using a noncontact displacement probe called a Fontonic Sensor, Model KD45A, Mechanical Technology, Inc.

Anemometer Positioning and Flow Measurement

One of the two 17-in.-diam viewing portholes on the side of the test section was modified so that a 7/8-in. brass tube, which held a DISA 55A83 hot film anemometer probe, could be inserted into the tunnel normal to the beam surface. The viewing port was 1 1/4-in.-thick Plexiglas and had a 4-in.-diam penetration hole, which was covered with a 6 3/4-in.-diam, 1/8-in.-thick, brass plate that held the 7/8-in. tube. The tube was held in a combination knurled screwdown clamp and 0-ring seal which was brazed to the plate. The brass plate was sealed against the Plexiglas via an 0-ring and was held against the plexiglas with three clamp screws. Likewise, the anemometer probe and the 7/8-in. brass tube were sealed with 0-rings. The brass plate-hole cover enabled the anemometer to be moved along the directions of the beam chord and length, while the 0-ring seal around the 7/8-in. brass tube allowed the anemometer to be positioned along the normal to the beam. The position measurements were made with a machinist rule with 0.01-in. graduations. A DISA 55D05 anemometer was used to drive the anemometer probe.

The mean inflow velocity was measured with a pitot-static tube and a mercury-in-glass manometer. This velocity measurement provided the anemometer calibration standard. The probe was mounted to the frame of the clamping block so that the probe tip was just upstream of the leading edge of the beam.

Mechanical Impulse Generator

In air a mechanical impulse could be delivered by striking the beam with a hard, hand-held object. This method, of course, was impossible in the closed and water-filled test chamber. The first design of a remotely powered, impulse generator consisted of a solenoid surrounding a cylindrical plunger. The solenoid was in a series circuit with a battery and microswitch. This arrangement produced impulses which were too long because of the long time duration of the pulse current. The plunger of the solenoid in this arrangement would chatter against the beam, regardless of the speed with which the microswitch was activated. Hence, it was decided to discharge a capacitor through a solenoid in order to produce a short time current pulse. A small RC time constant was needed to produce a pulse of short time duration, while a large capacitance was needed to provide enough energy at a given charge voltage to excite the plunger during discharge. Consequently, it was necessary to find a solenoid with a resistance as low as possible, capable of carrying a large current lead. Fortunately, a starting solenoid from an old Chevrolet automobile was available, and this was modified to produce the mechanical impulse generator. The two separate windings of the solenoid were reconnected in series; then the entire solenoid along with the lead-in cable was waterproofed.

The plunger consisted of a brass rod 1/4 in. in diameter and 10 in. in length, which was held concentric with an iron pipe 3/4-in. in diameter and 1/4 in. in length by using a brass bushing. The brass rod protruded from the end of the solenoid. Figure 18 shows a sketch of the assembly. Parallel to the axis of the rod the cross bushing was drilled out as much as possible to reduce both the mass of the plunger and the frictional force of the water on it. The plunger was pulled into the solenoid by the magnetic field, and a spring was used to keep the plunger away from the stop of the solenoid after the magnetic field had collapsed. Power for the solenoid was provided by a 4000 μF, 50-V capacitor, which was charged to the desired potential, using a Sorensen Model QRD40-0.75 power supply. Finally, a double pole, double throw switch was used to isolate the power supply from the discharge transient. The final assembly had a resistance of only 1.5 ohm.

In operation, the capacitor was charged to the desired potential then discharged via the double pole, double throw switch, through the solenoid, producing a strong, short time duration magnetic field, which pulled the plunger into the solenoid and, consequently, caused the tip of the 1/4-in. brass rod to strike the beam. The strength of impact was changed by varying the charge on the capacitor.

Test Procedure

Before a typical run, the water tunnel was filled and then deaerated for 1 hr to remove bubbles from the test chamber. Then, following selection of a jet velocity, the 3-Hz-bandwidth levels of flow-induced beam acceleration were obtained. Finally the impulse-excited decay times were θ measured.

RESULTS OF MEASUREMENTS

Resonance Frequencies and Mode Shapes

The fundamental beam mode $m = 0$ for a 20-in.-long by 0.2-in.-thick cantilevered beam has a theoretical resonance frequency in air of approximately 14 Hz; however, the actual fundamental frequency could not be measured by shaking because that mode was outside the frequency limitations of the instrumentation. The resonance frequency for the 2.75-in. beam in water, calculated using Equations (9) for the entrained mass, is about 10 Hz. Narrow band, filtered levels of flow-induced acceleration on some beams displayed peaks in the range from 10 to 15 Hz which became less distinct as water speed was increased. Undoubtedly, the fundamental resonance was influenced by the finite mass of the clamp as well as by the stiffness of the rubber mounts. The theoretical resonance frequencies in water are given by a combination of the relationships following Equations (5) and (17), i.e.

$$\omega_m = \sqrt{\frac{D}{\rho_p h + m_m}} \frac{\pi^2}{4L^2} (2m + 1)^2 \ , \ m \geqslant 1 \tag{31}$$

Measured resonance frequencies are given in Table 2; for beam (m,0) modes in air, they are higher than those calculated by using Equation (31) by less than 15 percent. Torsion mode (0,n) resonance frequencies were not calculated. Entrained mass for the bending modes, determined from the resonance frequencies of Table 2, was in agreement with Equation (9).

Nodal patterns in water for beam modes of the 2.75- by 20-in. beam are shown in Figure 19. Locations of the shaker and reference accelerometer are designated by S and A, respectively, on each diagram. Also, the node lines, which are the theoretical points calculated by Young and Felgar (1949),[20] are shown for each resonance. Generally, the measured nodal patterns are curved, the curvature is caused by both the varying thickness and the finite width of the beam. For the $m = 2$ mode, the mode shape in water was measured for two chordwise locations along the knuckle and near the center of the beam. The arrows in Figure 19 show the measurement locations. The results are compared with the theoretical in vacuo mode shape of Young and Felgar in Figure 20. The vibration levels were normalized to be two at the tip. With this normalization, the curves of Figure 20 are consistent with the normalized functions of Equation (5). We see that the theoretical mode shape for $m = 2$ is only a rough approximation to the actual vibration patterns at the resonance frequency. The lack of similarity is probably due to the variable thickness of the beam and to the

[20]Young, D. and R.P. Felgar, "Tables of Characteristic Functions Representing Normal Modes of Vibration of a Beam," University of Texas, Publication 4913, Engineering Research Series 44 (Jul 1, 1949).

non-ideal clamping, since measured vibration patterns in air are similar to those measured in water. Theoretical in-vacuo mode shapes for the other modes, obtained from Reference 20, are also shown in Figure 20. The single point acceleration measurement, located on all beams at $z/L \simeq 0.28$ and denoted by arrows in Figure 20, can be considered representative of the theoretical mean-square level. For the m = 4 mode, the deviation of the mode shape from the theoretical nodal pattern as shown in Figure 19 probably accounts for the acceleration levels being measured at this location for this mode. Nevertheless, measured vibration levels for the m = 4 mode are likely to be relatively low. Also, since the beam passed through a dead-water region into the jet, the flow covered $z/L > 0.3$ for the 20-in.-long beams and $z/L > 0.43$ for the 14-in.-long beam.

Figure 21 shows 3-Hz-bandwidth acceleration levels for the 2.75-in. beam at 23.5 ft/sec with the mode orders responsible for the peaks shown in parentheses. The frequency is on a linear scale, and the acceleration levels are referred to the gravitational acceleration. The acceleration peaks at low frequencies have larger bandwidths than at high frequencies because of the higher loss factors at low frequencies. Other spectra at low speeds show a peak at approximately 10 to 15 Hz, which corresponds to the fundamental mode of motion. At this point it is well to note the coincidence of the expected fundamental with approximate resonance frequency of the rocking mode of the block 12 Hz and the 12-Hz rotation rate of the tunnel drive-propeller blades at $U_0 \simeq 7$ ft/sec. Thus we had at nearly 7 ft/sec the well-defined 10- to 15-Hz peak in the acceleration spectrum which could account for a ±0.5-deg angle of attack oscillation.

Dependence of Damping on Flow

Measured total loss factors for all of the 20-in. beams in still water are shown in Figure 22. The loss factors show no consistent dependence on the width of the beam, and they are higher in water than in air, where they are less than 10^{-3}. The effect on damping of wetting the clamp was determined in a small tank with and without immersion of the clamp. Only enough water was used to cover the clamp, leaving the complete length of the beam exposed to air. The loss factors were unaffected by wetting the clamp. Thus, it is assumed that the damping of the beam in air is controlled by dry friction in the clamp. The damping caused by viscous losses is estimated, using an empirical result obtained on blunt-edged, free-free beams by Blake.[1] Designating the viscous loss factor by η_v, we have from Reference 1

$$\eta_v = 4.5 \frac{\rho_0}{\rho_p h + m_m} \sqrt{\nu/\omega_m}$$

This expression has been plotted in Figure 22, using parameters for the 2.75-in.-wide beam. The observed loss factors are at least three times the calculated ones. It is possible that the sharp trailing edge has increased the viscous losses. Most of the results shown in Reference 1 were obtained with blunt-edged beams, and the effect of edge sharpness was never fully examined. In an experiment comparing the round- to sharp-edged damping of a cantilevered beam, Kerr, Shannon, and Arnold (1940)[21] determined a factor of 3.5 increase in damping level with sharp edges. In the current experiments, higher damping was observed when small bubbles were attached to the beam surface. These were generally removed after deaeration of the tunnel. Figure 23 shows the increase of loss factor with inflow speed U_0 for the 2.75-in. beam. The damping is highest at low frequencies, approaching nearly 9 percent of critical for the m = 1 mode.

The data have been normalized in line with the interpretation of Equations (18) and (19). The measured loss factors are multiplied by the ratio of the fluid plus structural masses to the entrained fluid mass. At high enough speeds when flow effects dominate the damping, we can interpret measurements as hydrodynamic loss factors

$$\eta_H = \frac{r_t}{m_m \omega}$$

which are given by Equation (19). Frequency is nondimensionalized, using the inflow velocity U_0 and the beam width w. Hydrodynamic loss factors for both the 1.5- and 2.75-in.-wide by 20-in.-long beams are shown in Figure 24. The data from Figure 21 are included and cover bending modes m = 1 through m = 4 as well as the first torsion mode of the 2.75-in. beam. At very low reduced frequencies—high speeds and low frequencies—the loss factors were calculated from the bandwidths of the flow-induced acceleration spectra. It appears that the hydrodynamic loss factor is well described as a function of reduced frequency $\omega w/U_0$ alone. Also shown in Figure 24 are the two- and three-dimensional asymptotic approximations for the hydrodynamic loss factors given by Equations (20) and (21). Since only a fraction of the length of the beam l_w/L is exposed to the waterflow, calculated η_H includes this factor. At very low reduced frequencies, the data approach the two-dimensional theoretical loss factors, and the measured loss factors approach the theory for vanishing aspect ratio AR at high reduced frequencies. At still higher reduced frequencies, those consistent with small values of U_0, the measured values of η_H approach an asymptotically constant value equal to the stillwater loss factors.

---

[21] Kerr, W. et al., "The Problems of the Singing Propeller," Proceedings of the Institute of Mechanical Engineering Vol. 144, p. 54 (1940).

Figure 25 shows hydrodynamic loss factors for the 5-in. wide by 20-in.-long beam. In this case data for beam modes m = 1, m = 2, and m = 4 as well as for the torsion mode (0,1) and plate modes (1,1) and (2,1) are shown. Theoretical values given by Equations (20) and (21) are included for the beam modes; the theoretical two-dimensional loss factor for the torsion (0,1) mode given by Equation (22) is also included. The loss factors for both mode types approach the two-dimensional values at low reduced frequencies. Figure 25 shows the hydrodynamic loss factors for the 1.5- by 14-in. beam. Only beam modes were examined, and the loss factors are again dependent only on reduced frequency. Also included are the theoretical two- and three-dimensional asymptotic limits as well as a more precise computation using results tabulated by Lawrence and Gerber.[11] The excellent agreement with theory as well as the close collapse of the data for all beams is strong evidence for the simple description of the hydrodynamic loss factor as a function of reduced frequency alone.

The loss factors at high reduced frequencies in Figures 24 through 26 are influenced by the damping extant in the beam at zero flow. We could delete the contribution at zero flow by assuming that the total loss factor is a linear sum of that hydrodynamically induced and that extant at $U_0 = 0$. Unfortunately such a correction, although appealing, is poorly founded since we have not characterized the mechanisms of damping in water at $U_0 = 0$. Thus we cannot say that the same mechanisms exist unchanged, when $U_0 \neq 0$. Viscous damping, for example, may well be modified when a steady flow is imposed on the beam.

Another effect, until now overlooked, is that caused by finite thickness. The two- and three-dimensional unsteady foil theory has been developed for struts of vanishing thickness. When, in fact, the reduced frequency is high enough so that $\omega h/U_0 > 1$, we can expect thickness effects to, perhaps, change the observed damping. These points correspond to $\omega w/U_0 \gtrsim 20$, 11, and 6 for the 5-, 2.75- and 1.5-in. beams, respectively. If we subtract loss factors measured at $U_0 = 0$ from those measured at $U_0 \neq 0$ we obtain values that are considerably lower than the theoretical lines shown in the figures for $\omega w/U_0 > 40$ or so. This has two possible causes: thickness effects reduce the hydrodynamic damping, and the loss factors at $U_0 = 0$ do not apply at $U_0 \neq 0$ because viscous effects on the damping are reduced, thus lowering the residual damping.

Flow-Induced Vibration Measurements

The records of 3-Hz-band acceleration levels, similar to the levels shown in Figure 20, were analyzed to determine modal acceleration spectral densities at each resonance frequency. These spectral densities $\phi_{\underset{m}{AA}}(\omega, \vec{x}_0)$ were then nondimensionalized on flow variables to emphasize the functionality demonstrated by Equation (26B). Letting the mean-square, 3-Hz-band levels measured at a position on the beam $\vec{x}_0$ be $\overline{a^2}$, the spectral density is

$$\phi_{AA}(\omega, \vec{x}_0) = \frac{1}{4\pi} \frac{\overline{a^2}}{\Delta f}$$

where

$$\Delta f = \eta_T f_m \qquad \eta_T f_m \leqslant 3 \text{ Hz}$$

or

$$\Delta f = 3 \qquad \eta_T f_m > 3 \text{ Hz}$$

where η_t is the total loss factor of the mode m, and f_m is its resonance frequency. The resulting acceleration spectra $\overline{a^2}/\Delta f$ are shown for the 2.75-in. beam in Figure 27. With the exception of some anomalous behavior at the lowest speed, the spectra vary smoothly with frequency. We note that only beam (m,0) mode response was examined in this manner. Mode orders are shown in parentheses in Figure 27.

A rearrangement of Equation (26B) to emphasize nondimensionalization is

$$\frac{\phi_{AA}(\omega, \vec{x}_0)}{q_0^2} [m_b + m_m]^{1/2} \eta_T^2 \frac{U_0}{h}$$

$$= 2\,\Psi_m(z_0) \frac{2\lambda_x 2\lambda_z}{A_s} \int_{-1/2}^{1/2} \frac{\Phi_\rho(\omega) \frac{U_0}{h}}{q_0^2} \frac{d\left(\frac{x}{w}\right)}{1 + \left(\frac{\omega\lambda_x}{U_c}\right)^2} \tag{32}$$

where we have replaced $\rho_p h$ by the area density m_b and have introduced the dynamic head of the inflow. Frequency should be nondimensionalized on a boundary-layer length scale as emphasized in Chapter 3; however, the magnitude of that scale is unknown. Figure 7 indicates that the dominant boundary-layer growth occurs at the wedge of the cross section so that we have used the maximum thickness of the section h as a characteristic length for scaling purposes. The dimensionless spectra for the 2.75-in. beam, taken from Figure 27, are shown in Figure 28. The flagged points denote data for the n = 4 mode. The nondimensionalization of Equation (32) collapses the data for individual speeds very well. Close correspondence of the points suggests that the boundary-layer length scale, which we have previously assumed proportional to h, and $\overline{\lambda_x}$ and $\overline{\lambda_z}$ are only weak functions of speed and are not dominantly affected by the vibration level. The data for the n = 4 mode may be relatively low because of the proximity of the accelerometer to the theoretical and actual locations of the node line of that mode.

The nondimensionalization was repeated for the other beams of the set; Figure 29 shows results for the 5-in. beam. Although the points for the 5-in. beam collapse well in terms of U_0 and h, the dimensionless spectra deviate slightly from those of the 2.75-in. beam at high frequencies. This would indicate that the actual length scale, which determines the high-frequency spectrum, is about 20 percent smaller relative to h on the 5-in. beam than it is on the 2.75-in. beam. Figure 30 shows dimensionless spectra for the 1.5- by 20-in. beam; the spread in the data includes the mean lines for both the other beams. In the case of the 1.5- by 20-in. beam, the m = 4 node line is apparently quite near the accelerometer since the flagged points are consistently the lowest. Finally, Figure 31 shows dimensionless spectra for the 1.5- by 14-in. beam. The dimensionless accelerations are all in agreement. The mean line for the 2.75-in. beam has been linearly adjusted for the difference in flow coverage over the span denoted by l_w.

All the normalized modal acceleration spectral densities appear to be nearly unique functions of $\omega h/U_0$ alone. To examine the possible analytical modeling of the acceleration spectrum, we require a combination of Equations (29) and (30) with Equation (32), using the appropriate fluid-scaling laws.

Mean and Turbulent Velocity Profiles Behind the Beam

To establish a basis of scaling the flow characteristics obtained in air to the conditions existing in the water tunnel, it was necessary to make a cursory velocity survey in the vicinity of the flow-excited beam. The measurement was performed for two speeds at Position F of the 2.75-in. beam at a distance $z/L \simeq 0.8$ below the clamping block.

The mean-velocity profiles were measured at two flow speeds of 3.7 and 7.7 ft/sec. The data were obtained on both sides of the beam. Figure 32 shows all four profiles normalized as U/U_∞ versus y/δ, where y is measured from the center of the axis. The profiles agree with each other and with the profiles measured in air. The strut was about 1-deg constant angle of attack, and the very low frequency vibratory motion of the beam accounted for another ± 0.5 deg superimposed on this. Thus the instantaneous angle of attack was bounded between a 0- and 2-deg angle of attack.

Figure 33 shows longitudinal turbulence intensities at Position F behind the 2.75-in. beam. Included are the results from Figures 4 and 6 for Position F obtained in air; the results obtained in water are generally bounded by the 0- and 2-deg angle-of-attack results in air. At values of $y/\delta > 2$ the turbulence intensity is approximately 0.01. This value was obtained with a 5-Hz, high-pass filter; with a 100-Hz, highpass filter, the background intensity is only 0.002. The autospectral densities of the turbulence levels obtained at Position F in air and in water are shown in Figure 34. The measurements were obtained well within

the boundary layers. The autospectra are normalized on the local mean velocity U, local mean-square velocity $\overline{u^2}$, and δ^*. The normalized spectra display an overall spread of 6 dB. All measurements at y = 0 are in agreement, regardless of the flow medium or angle of attack. At $y \simeq 2\delta^*$ the measurements in air are slightly higher at midfrequencies. However, they coalesce better at low and high frequencies. The close similarity of turbulent velocities in air and water further substantiates the flow-similarity in both media.

Table 3 summarizes some of the boundary-layer characteristics at Position F in air for $\alpha = 2°$ and in water; δ/δ^* and δ^*/h are nearly invariant over the Reynolds number range indicated. The experiment was designed to maintain similar air and water Reynolds numbers so that the scaling of results would be simple.

The background turbulence spectra were obtained for frequencies above 5 Hz at three speeds. In Figure 35 the spectral densities are shown nondimensionalized as

$$\frac{\phi_{uu}(\omega)\, U_0/h}{U_0^2} \text{ versus } \frac{\omega h}{U_0}$$

where h is a length arbitrarily selected to be equal to the beam thickness and h = 0.25 in. For speeds of U_0 = 7 ft/sec and U_0 = 13.2 ft/sec this nondimensionalization seems to generally describe the spectra; for U_0 = 3.5 ft/sec this spectrum level is uniformly 8 dB lower than those at the higher speeds. For later use we will determine a longitudinal integral scale by assuming that Taylor's Hypothesis of frozen convection applies to the turbulence and that the spectrum is of the form

$$\frac{\phi_{uu}(\omega)\, U_0/h}{U_0^2} = \frac{\overline{u_B^2}}{U_0^2} \frac{L'/\pi h}{1 + (\omega L'/U_0)^2} \tag{33}$$

The background intensity is $\overline{u_B^2}^{1/2}$ and L' is an integral scale of the intensity. Matching this spectrum form to the high-speed data in Figure 35 and using $\overline{u_B^2}^{1/2}/U_0 = 0.03$ we find $L' \simeq 2h$.

These spectra are compared to those determined in the wake of the 2.75 in. beam as shown in Figure 34. We multiply the high-speed data of Figure 35 by $\overline{u^2}/\overline{u_B^2}$ where $\overline{u^2}$ is here taken as the typical mean-square intensity in the wake and which is on the order of $0.01\, U_0^2$. We will also take $\overline{u_B^2}^{1/2}/U_0 = 0.028$; this is the broadband intensity at tunnel speeds of 7 ft/sec and 13 ft/sec. We will replace h by $\delta^* = 0.05$ in. So modified, the high-speed spectrum of Figure 35 has been plotted in Figure 34. This background is not influenced by electronic noise and we see that except at the lowest frequencies the shear layer turbulence is not comparable to the water tunnel background.

5. ANALYTICAL ESTIMATES OF THE FLOW-INDUCED ACCELERATION SPECTRUM

RESPONSE TO THE BOUNDARY-LAYER PRESSURE

An approximate expression for the acceleration induced by the boundary layer generated on the strut can be obtained from Equation (32). We let $\psi_m^2 (z_0) \approx 1$, and rewrite Equation (32), using the nomenclature of Figures 9 through 11

$$\frac{\phi_{AA} (\omega \vec{x}_0)}{q_0^2} (m_B + m_m)^2 \eta_T^2 \frac{U_0}{h}$$

$$\simeq \gamma_i \frac{2\lambda_x 2\lambda_z}{A_B^2} w_w \ell_w \left[\frac{\Phi_p \left(\frac{\omega\delta^*}{U_0}\right)}{q_0^2} \frac{\delta^*/h}{1 + \left(\frac{\omega\lambda_x}{U_c}\right)^2} \right] \tag{34}$$

where γ_i = 1 or 2, depending on whether the flow is correlated on one side or on both sides of the beam. In the case of the nonzero angle of attack, the low-frequency, boundary-layer pressures are mostly generated on one side, while those at high frequencies are equal and uncorrelated on both sides. The area of the beam which supports the most intense pressure field is denoted by $w_w \ell_w$, where ℓ_w is the depth of immergence into the waterjet of the tunnel. The close similarity of the flow fields at Position F in air and in water as indicated in Table 3 make scaling the results of Chapter 2 straightforward. Since the beam is at an angle of attack, the data of Chapter 2 for $\alpha = 2°$ will be used. The observation that at Position F δ^*/h varies only slightly over the Reynolds number range of Table 3 indicates that the average of δ^* over the wedge portion of the beam, say $\overline{\delta^*}$ should be nearly proportional to h. At 25 ft/sec, N_{Re_w} † = 2.9 x 10^5 in the air experiment, and N_{Re_w} = 1.6 x 10^5 in the water experiment at 7.7 ft/sec. Over this Reynolds number range, we expect the scaling of the pressure field to be on q_0 and δ^* as outlined earlier. We find at 25 ft/sec, $\overline{\delta^*}/h \simeq 0.13$. Figure 16B shows that separate models of the coherences are required above and below $\omega h/U_0 = 3$. As explained at the end of Chapter 3 we consider that the low frequency vibration affects the boundary layer as an oscillating angle of attack which probably does not instantaneously exceed 2 deg.

For high frequencies $\omega h/U_0 > 3$, corresponding to $\omega\delta^*/U_0 > 5$, we model the coherence with Equation (30). Curve fitting to Figures 13 and 15 yields

† $N_{Re_W} = U_0 W/\nu$

$$\lambda_x/\delta^* \simeq 5.5 \left(\frac{\omega\delta^*}{U_c}\right)^{-1}$$

$$\lambda_z/\delta^* \simeq 0.8 \left(\frac{\omega\delta^*}{U_c}\right)^{-1}$$

Figure 14 gives $U_c = 0.7\ U_0$. The average of δ^* over the width is determined by the downstream half of the width so that $w_w/w = 1/2$, and $\ell_w/L = 0.7$. Substitution into Equation (34) with $\gamma_i = 2$, gives

$$\frac{\phi_{AA}(\omega,\vec{x}_0)}{q_0^2}(m_b + m_m)^2\ \eta_T^2\ \frac{U_0}{h} \simeq 2.6 \times 10^{-8} \left(\frac{\omega h}{U_0}\right)^{-3}, \quad \frac{\omega h}{U_0} > 3 \tag{35}$$

where we have approximated

$$\frac{\Phi_p(\omega\delta^*/U_0)}{q_0^2} = 5 \times 10^{-5} \left(\frac{\omega\delta^*}{U_0}\right)^{-1}, \quad \frac{\omega\delta^*}{U_0} > 0.5$$

Equation (35) is the high-frequency boundary-layer excitation designated in Figure 35. The estimate agrees well with the measured values. Similarly, for the 1.5- by 14-in. beam, assuming that the boundary layer is nearly similar to that developed on the 2.75-in. beam, we have $\ell_w/L = 1/2$, and $w_w/w \simeq 1$, which, using data for $\alpha = 0°$, gives

$$\frac{\phi_{AA}(\omega,\vec{x}_0)}{q_0^2}(m_b + m_m)^2\ \eta_T^2\ \frac{U_0}{h} \simeq \begin{cases} 4.3 \times 10^{-9} \left(\frac{\omega h}{U_0}\right)^{-2}, & 3 < \frac{\omega h}{U_0} < 25 \\ 1.06 \times 10^{-7} \left(\frac{\omega h}{U_0}\right)^{-3}, & \frac{\omega h}{U_0} > 25 \end{cases}$$

and these equations are shown in Figure 31. The theoretical expressions in both cases account reasonably well for the observed acceleration levels.

At low frequencies of $\omega h/U_0 < 3$, we use Equations (29) which contain $\lambda_x = 13.7\ \delta^*$, and $\lambda_z = 2.9\ \delta^*$. We also have $U_c \simeq U_0$. Further, approximating that

$$\frac{\Phi_p(\omega)}{q_0^2}\frac{U_0}{\delta^*} = 4 \times 10^{-4}$$

$$w_w/w = 1$$

and

$$\ell_w/L = 0.7$$

we obtain

$$\frac{\phi_{AA}(\omega,\vec{x}_0)}{q_0^2}\frac{U_0}{h}(m_b + m_m)^2\,\eta_T^2 \simeq \frac{1.2 \times 10^{-7}}{1 + 3.2\left(\frac{\omega h}{U_0}\right)^2}$$

This is designated the low-frequency, $\alpha = 2°$, boundary-layer excitation in Figure 35. In this case the observed acceleration spectrum is greater than that which could theoretically be generated by the low-frequency, boundary-layer pressure. In the midfrequency range near $\omega h/U_0 \simeq 3$, the measured acceleration spectrum is close enough to the theoretical estimate for response to this part of the pressure field to be plausible.

RESPONSE TO INFLOW TURBULENCE

The right hand side of Equation (34) can be interpreted as a mean-square pressure coefficient exerted on the surface of the strut. Mugridge (1970)[3] has theoretically determined the mean square pressure coefficient on a rigid strut exposed to a three-dimensional turbulent inflow. We haveadopted Mugridge's[3] result to determine the response of the beams to the water tunnel turbulence. Thus we obtain

$$\frac{\phi_{AA}(\omega,\vec{x}_0)\,U_0/h}{q_0^2}(m_b + m_m)^2\,\eta_T^2 = \phi_L(\omega)\frac{U_0}{h}$$

$$= 4\pi^2\frac{\phi_{uu}(\omega)\,U_0/h}{U_0^2}\frac{1}{1 + 2\pi k}\left(\frac{\frac{\omega L'}{U_0}}{1 + \frac{\omega L'}{U_0}}\right) \tag{36}$$

where we have assumed isotropic turbulence; L' is the macro-scale of the field and $k = \omega w/2U_0$. We have assumed $L' < w$. This equation gives the resultant pressure spectra in terms of the inflow turbulence spectra which have been given in Figure 35. We have found $L' \simeq 2h$ and we have already used the background intensity $u_{B_{rms}}/U_0 \simeq 0.028$.

For a strut of thickness h, we would expect Equation (36) to apply for $\omega h/U_0 < 1$ because for higher frequencies the pressure fields above and below the beam would necessarily be uncorrelated. The result of Equation (36) is shown as the upper dotted line in Figure 36. The close agreement with the measured acceleration levels gives a substantial indication that low frequency acceleration is generated by the inflow turbulence.

The estimates of beam acceleration that have been made in this part have indicated that inflow turbulence generated the very low frequency vibration. Boundary layer pressures generated by the flow on the beam accounted for the very high frequency acceleration. The low frequency pressures which are associated with leading edge separation may have accounted for acceleration only in a small frequency region around $\omega h/U_0 \simeq 3$.

6. CONCLUSION

The linear interaction of a beam with flow parallel to its neutral axis has been characterized in terms of fluid excitation and damping. The vibration of the beam at high frequencies is controlled by its own boundary-layer pressure, and the mean-square modal acceleration has been found to be proporational to both the correlation area and intensity of the pressure field. At the frequencies for which the boundary layer controls the flow excitation, the correlation area is inversely proportional to the square of the frequency. Dependence of the pressure field on large-amplitude, low-frequency motion manifests itself as an oscillating angle of attack which causes a somewhat thicker boundary layer than would otherwise exist; however, this does not have a dominant influence on the level of beam vibration. The coherence and intensity of the boundary-layer pressure field is controlled by the flow in the wedge region of the trailing edge.

At low frequencies, the inflow turbulence controls the excitation of the beam. For $\omega h/U_0 \leqslant 1$, the response is given by the Mugridge 3 result; however, for higher frequencies, existing simple theories are not adequate to correctly predict the response to inflow turbulence. It is reasonable that this small-scale turbulence influences the response of the beam just as the relatively large-scale turbulence in the boundary layer formed on the beam. Large eddies in the boundary layer, such as those originating with flow separation at the leading edge of the strut, could materially contribute to the beam vibration at moderate frequencies, i.e. $\omega h/U_0 \simeq 3$.

The fluid loading on the beam is dominated by inertial and circulatory effects. The magnitude of the measured entrained inertia did not differ from that which would be calculated from simple potential theory; see Equation (9). Hydrodynamic damping was the dominant contributor to the total loss factors of most modes at high speeds. As predicted by two-dimensional oscillating hydrofoil theory, the hydrodynamic damping for torsion modes was

double that for bending modes. The speed-dependent resistance to vibration, which is induced by the fluid and which causes the damping, is normalized on the measured entrained inertia to form a hydrodynamic loss factor. So defined, this loss factor is apparently a function of a reduced frequency, based on the width of the beam and inflow speed; this dependence is, within the limits of the parameters covered in the experiments, nearly unique. This observation is theoretically supported, since application of oscillating-airfoil theory for vanishing aspect ratio yields a hydrodynamic loss factor which is independent of the aspect ratio.

The vibration patterns measured at resonance deviate from the theoretically calculated mode shapes in vacuo. The deviation is due to the nonideal clamping as well as the chordwise variation in thickness. That fluid loading does not affect the resonance vibration pattern is indicated, since the same patterns were obtained in air and water.

ACKNOWLEDGMENT

The authors appreciate the assistance of Dr. Y. Liu, who performed a stability analysis for the beams. Also, we acknowledge the assistance of Mr. R. Dwyer in performing the wind tunnel measurements.

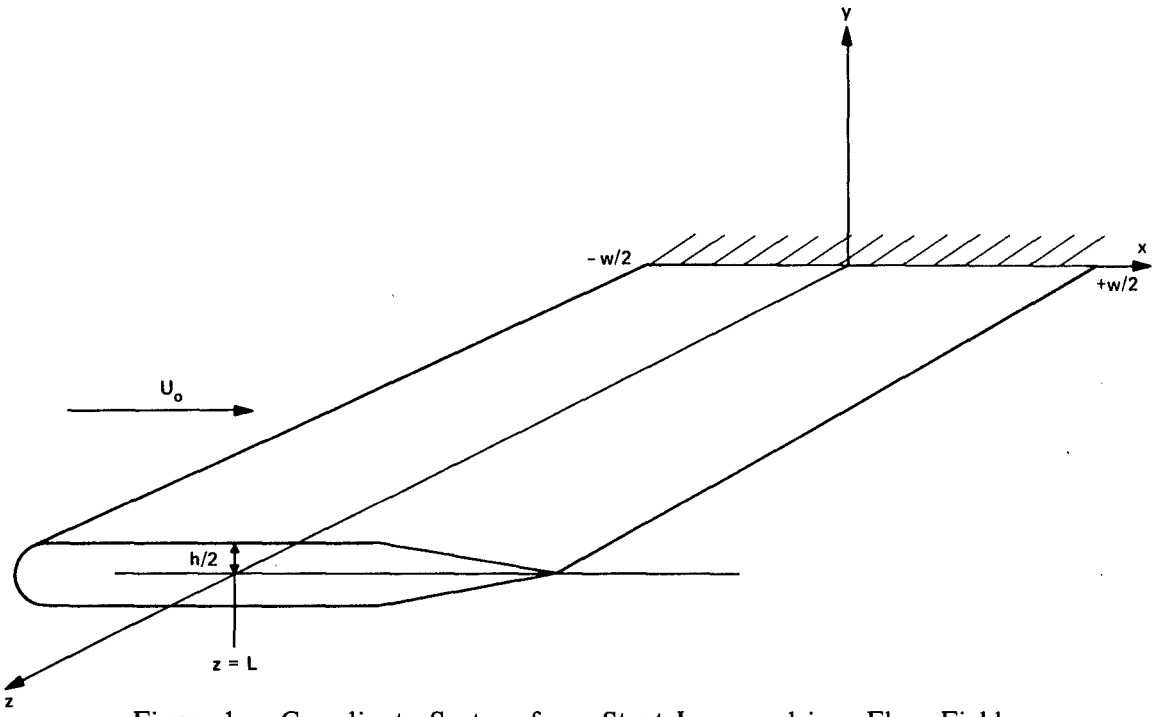

Figure 1 – Coordinate System for a Strut Immersed in a Flow Field

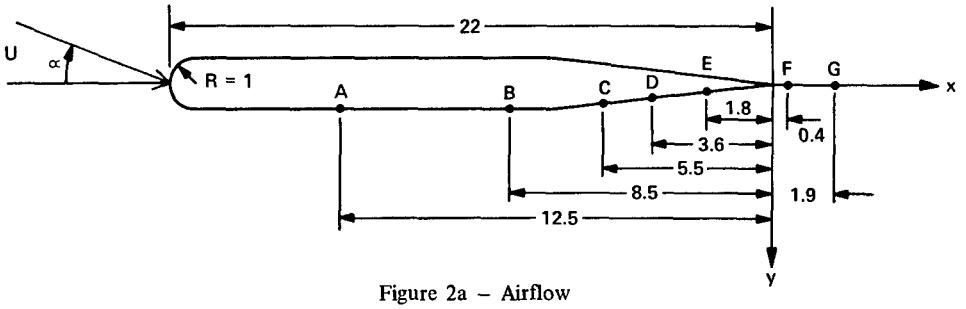

Figure 2a – Airflow

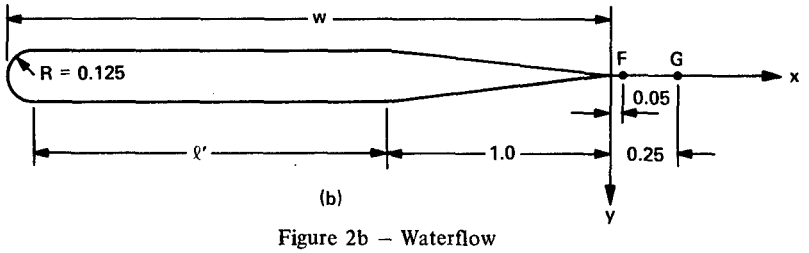

(b)

Figure 2b – Waterflow

Figure 2 – Cross Sections of Beams for Air- and Water-Flow Measurement, Showing Coordinates of Sensor Locations

All dimensions are in inches.

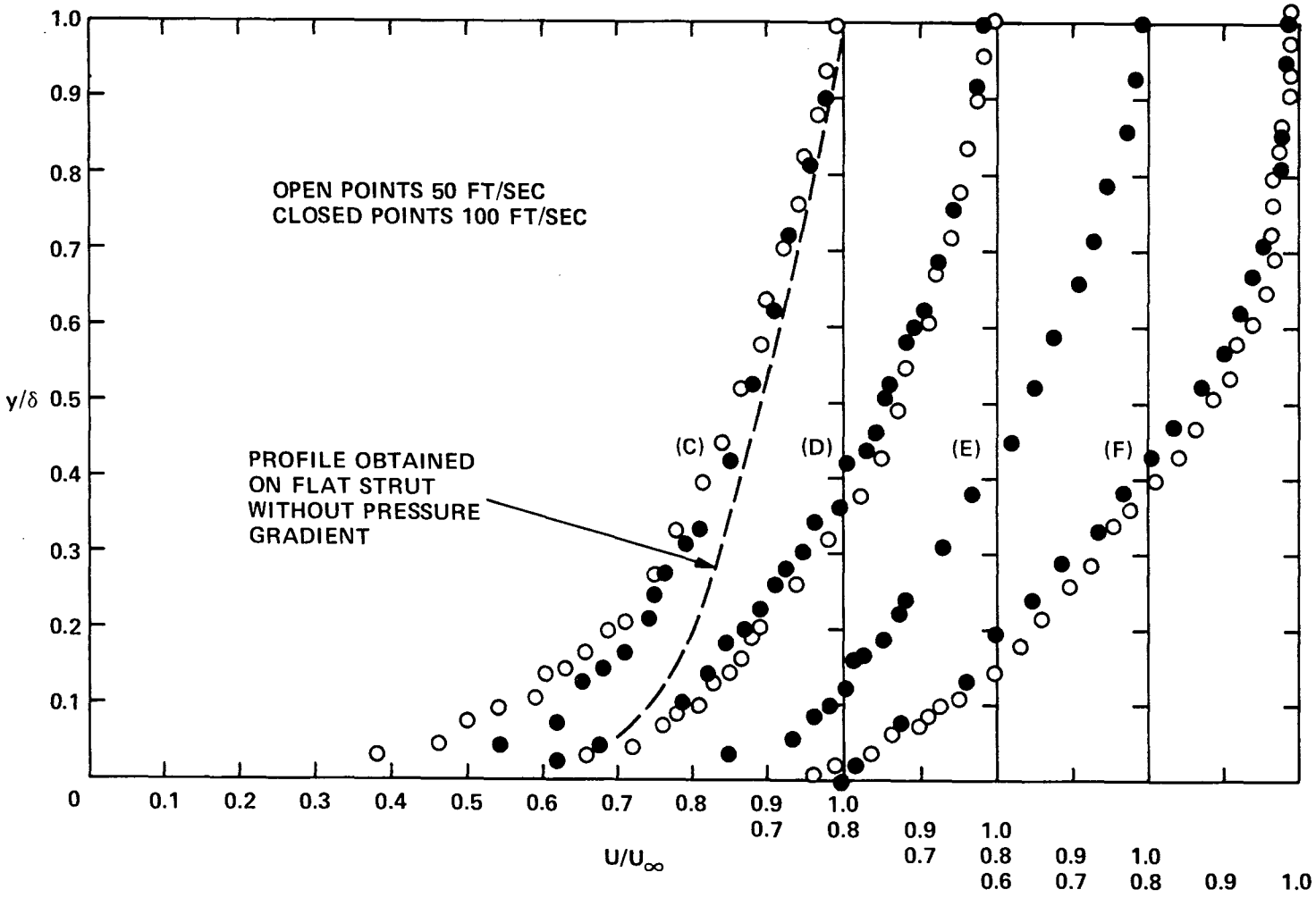

Figure 3 – Mean-Velocity Profiles at various Stations along the Strut in the Wind Tunnel at $\alpha = 0$ Degree

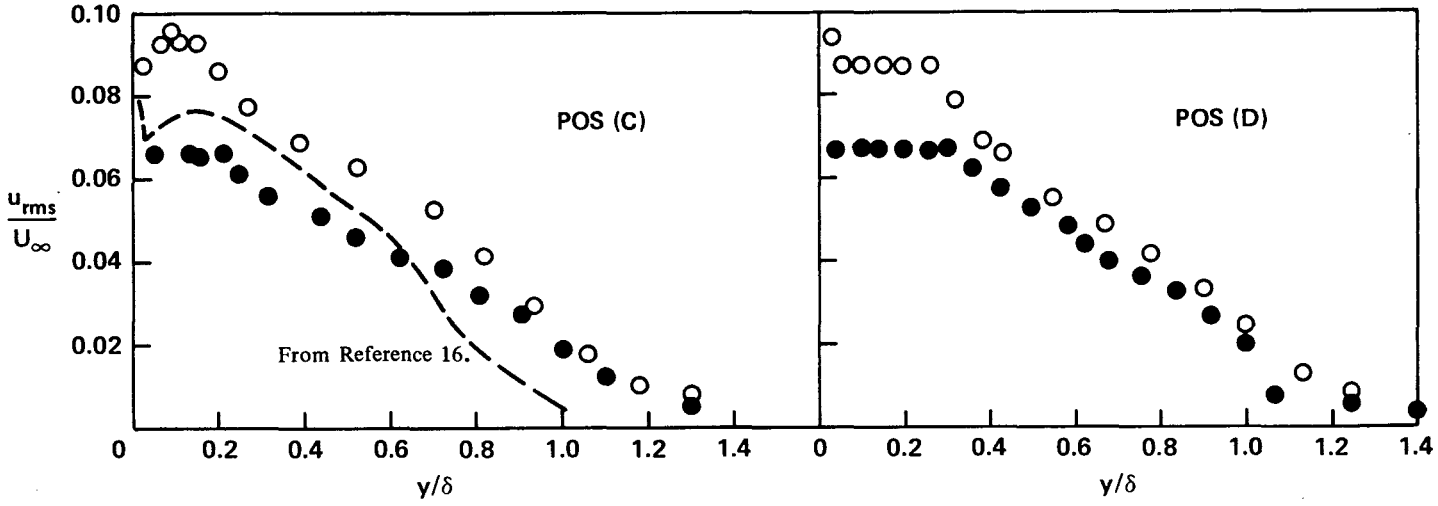

Figure 4a – Position C

Figure 4b – Position D

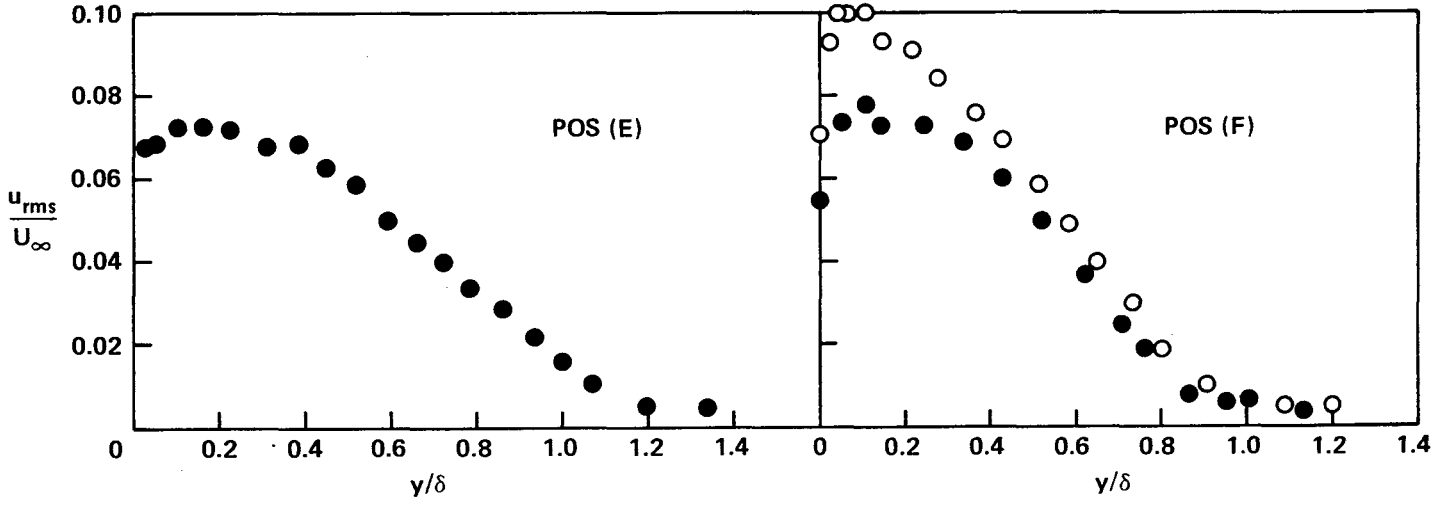

Figure 4c – Position E

Figure 4d – Position F

Figure 4 – Turbulence Intensities, Measured along the Rigid Strut at $\alpha = 0$ Degree in the Wind Tunnel

○ is 50 feet per second; ● is 100 feet per second.

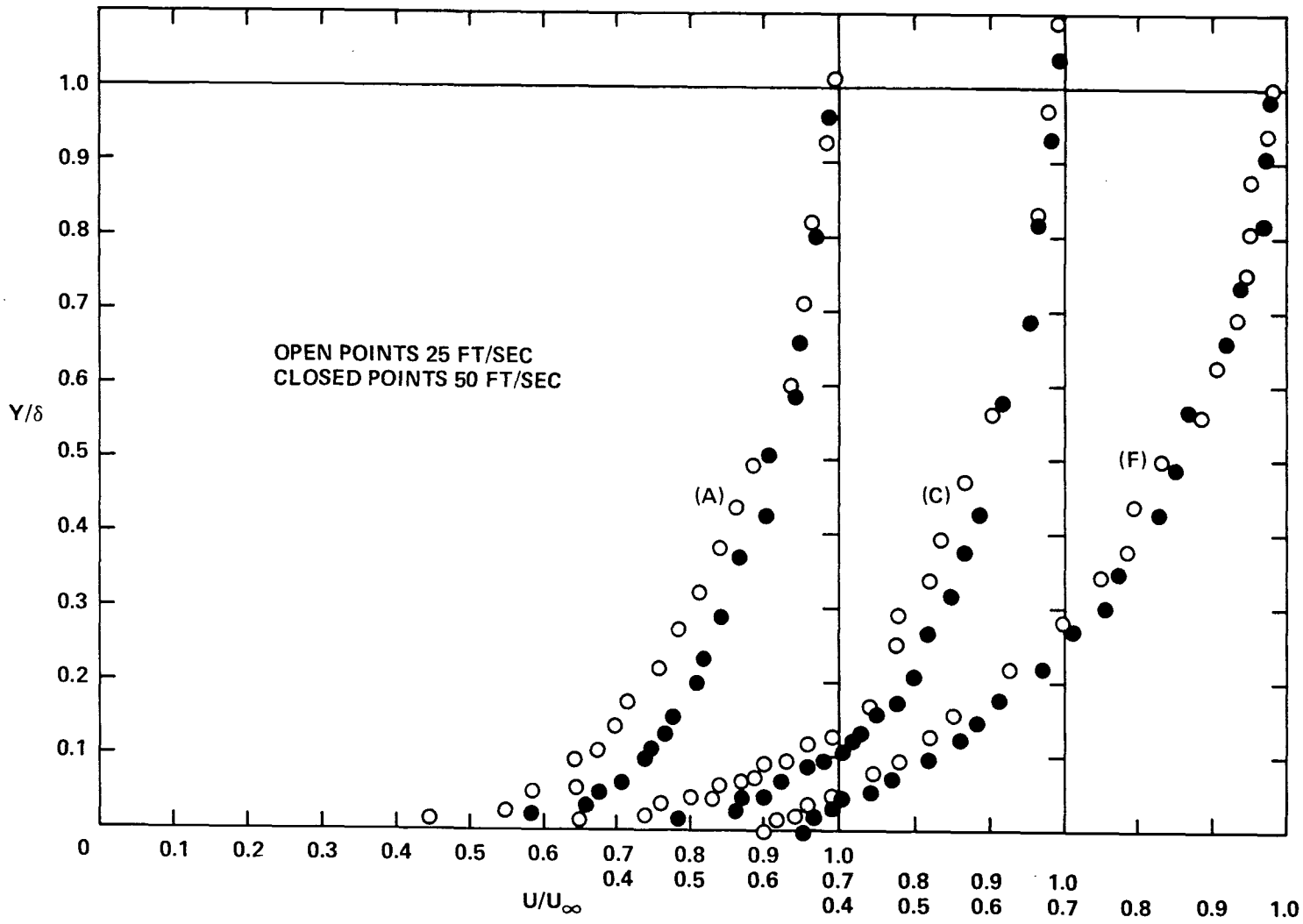

Figure 5 – Mean-Velocity Profiles at various Stations along the Strut in the Wind Tunnel at α = 2 Degrees

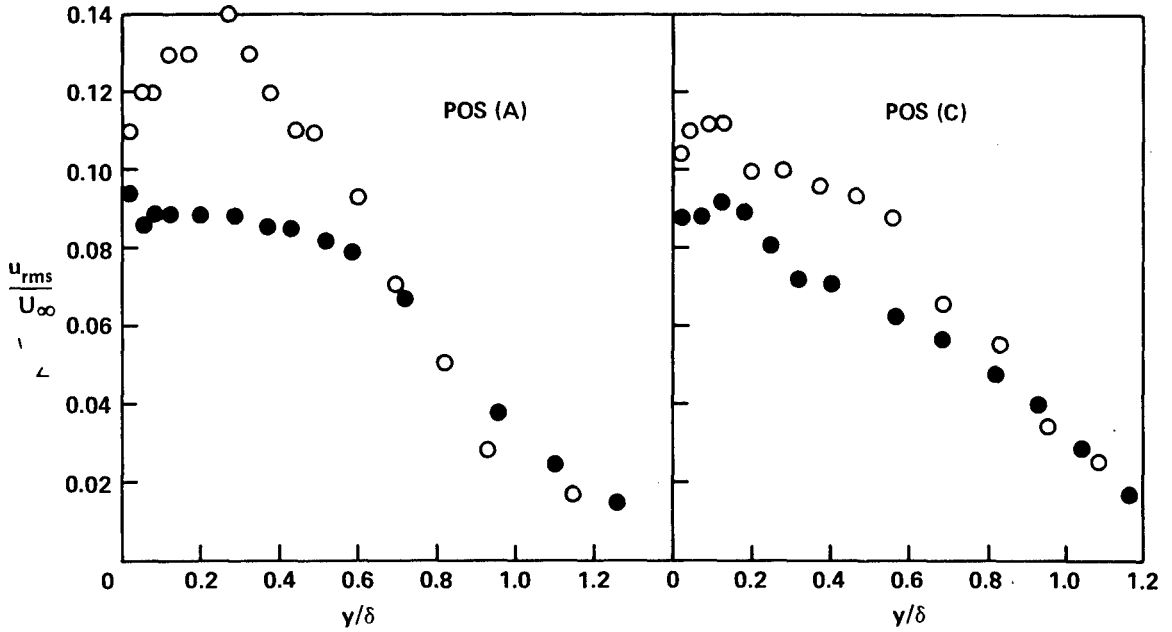

Figure 6a – Position A

Figure 6b – Position C

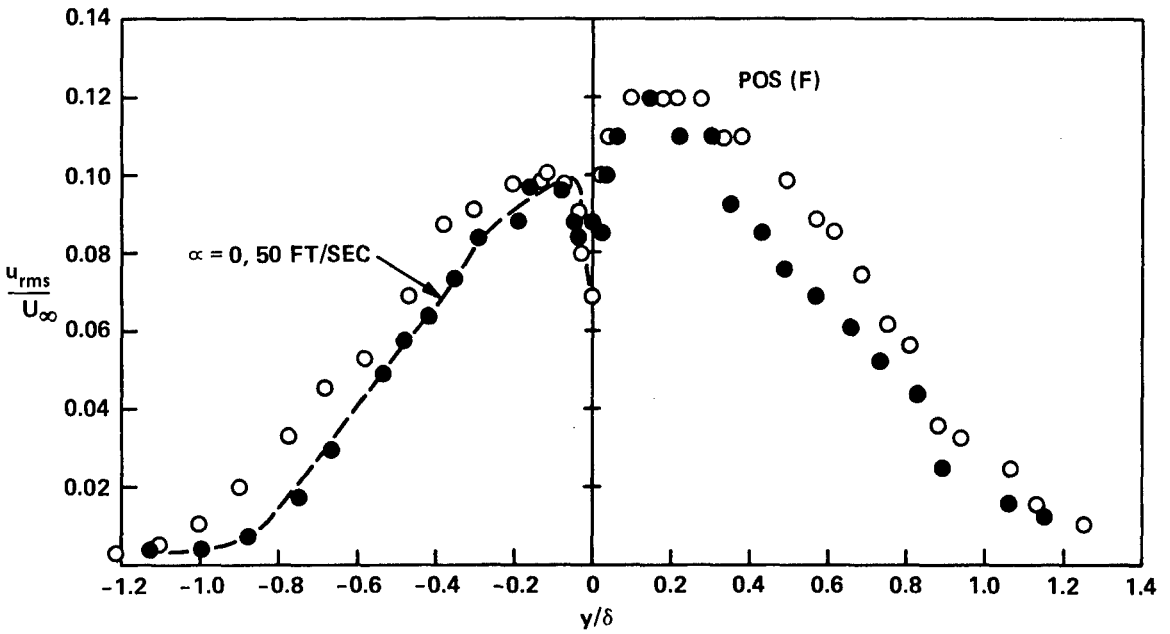

Figure 6c – Position F

Figure 6 – Turbulence Intensities, Measured along the Rigid Strut at α = 2 Degrees in the Wind Tunnel

○ is 25 feet per second; ● is 50 feet per second.

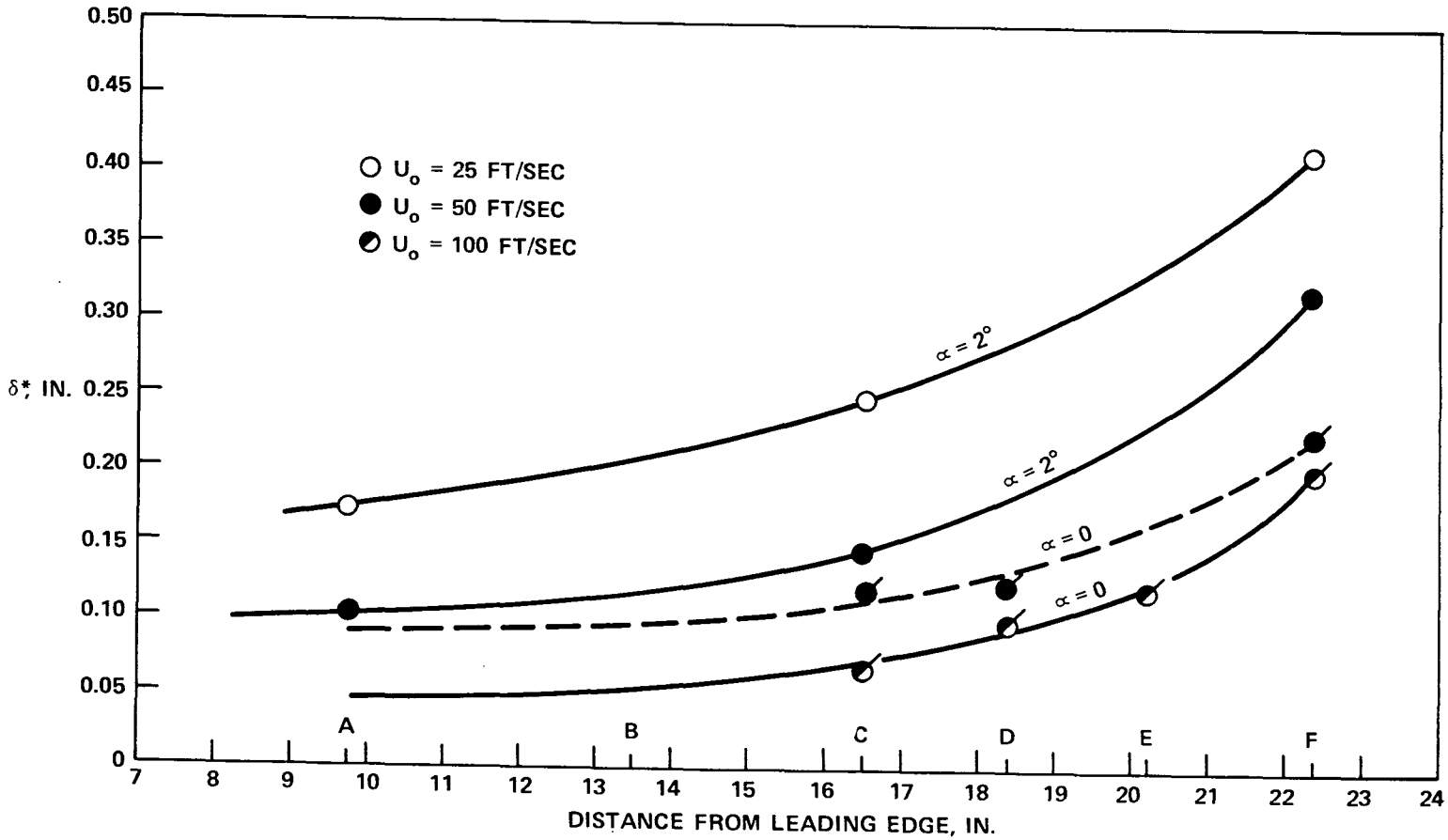

Figure 7 – Increase of Displacement Thicknesses along the Symmetrical Strut at α = 0 Degree and 2 Degrees

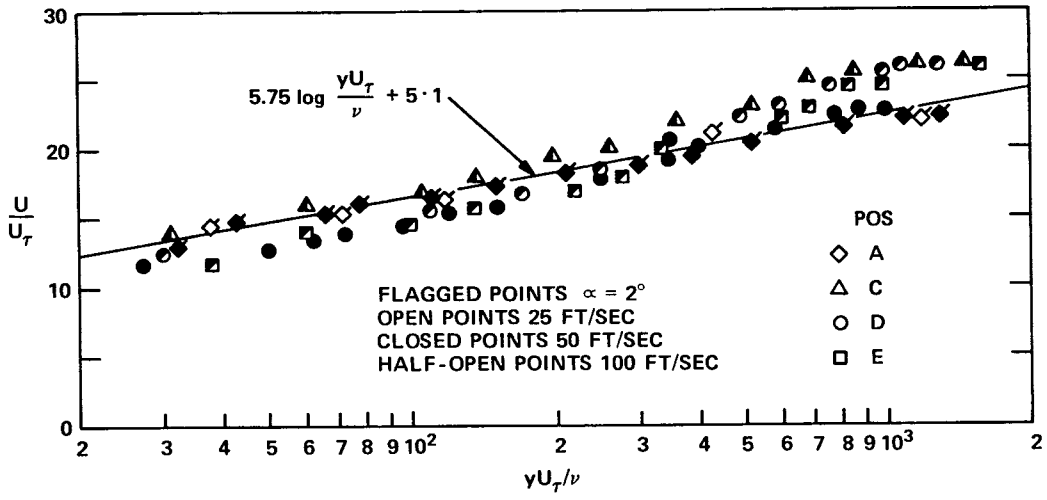

Figure 8 – Comparison of Measured Mean-Velocity Profiles to Coles Law of the Wall for ∝ = 0 Degree and 2 Degrees

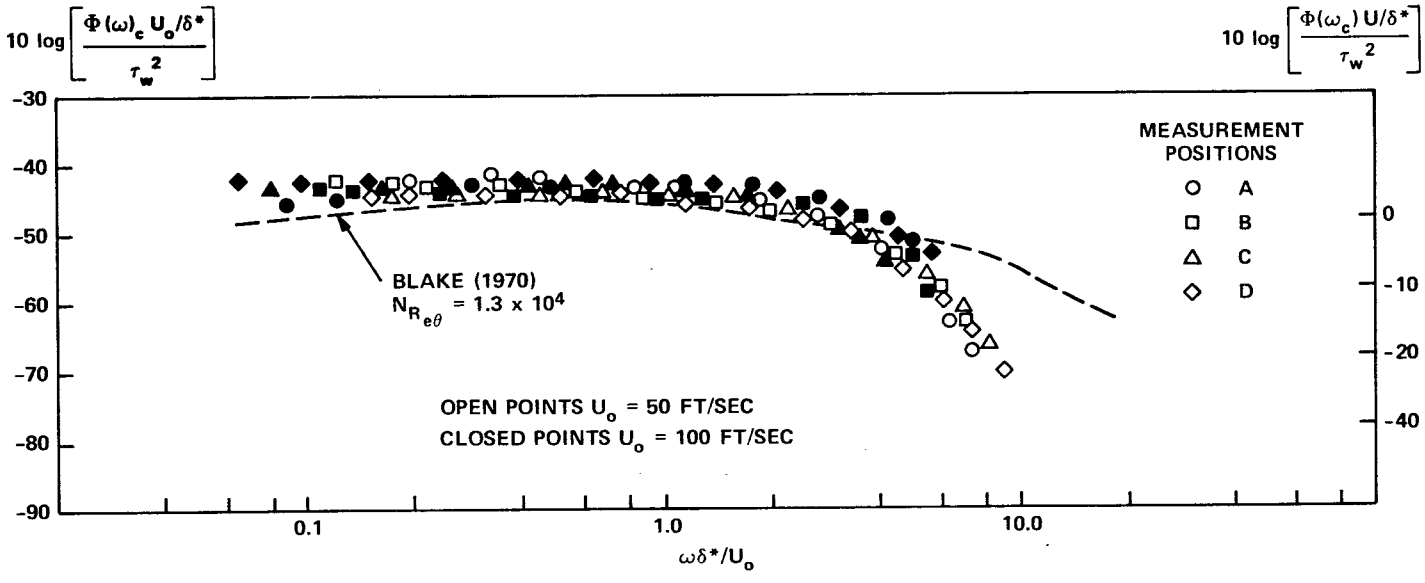

Figure 9 – Autospectra of the Wall Pressure on the Strut in the Wind Tunnel at ∝ = 0 Degree

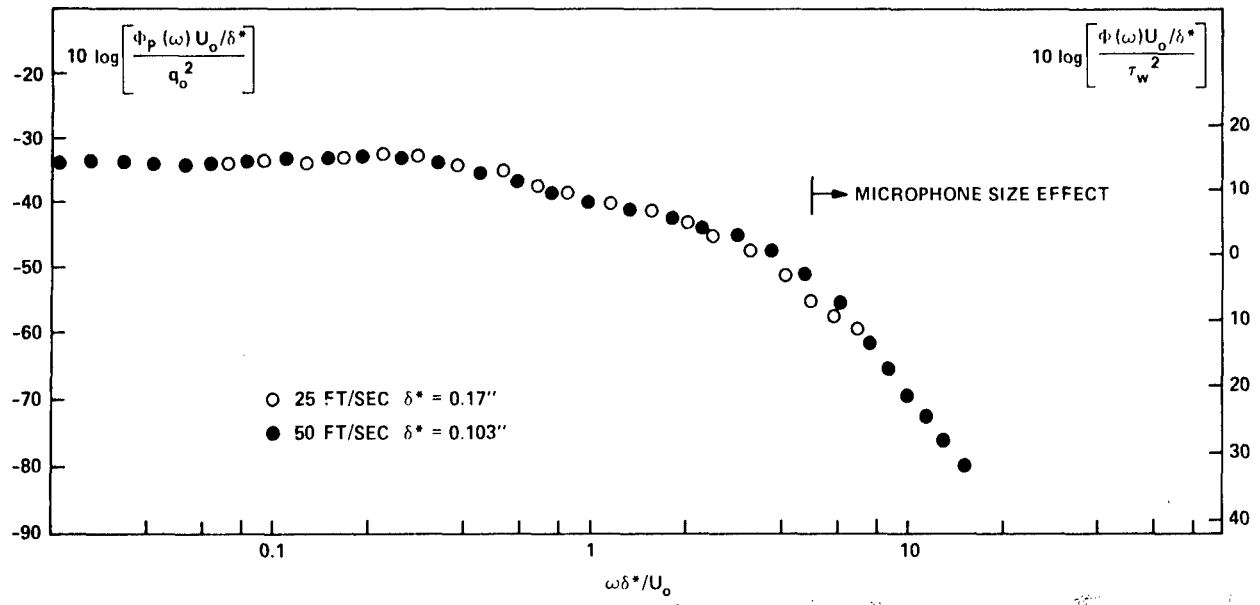

Figure 10 – Autospectra near the Semichord, Position A, on the Strut in the Wind Tunnel at α = 2 Degrees

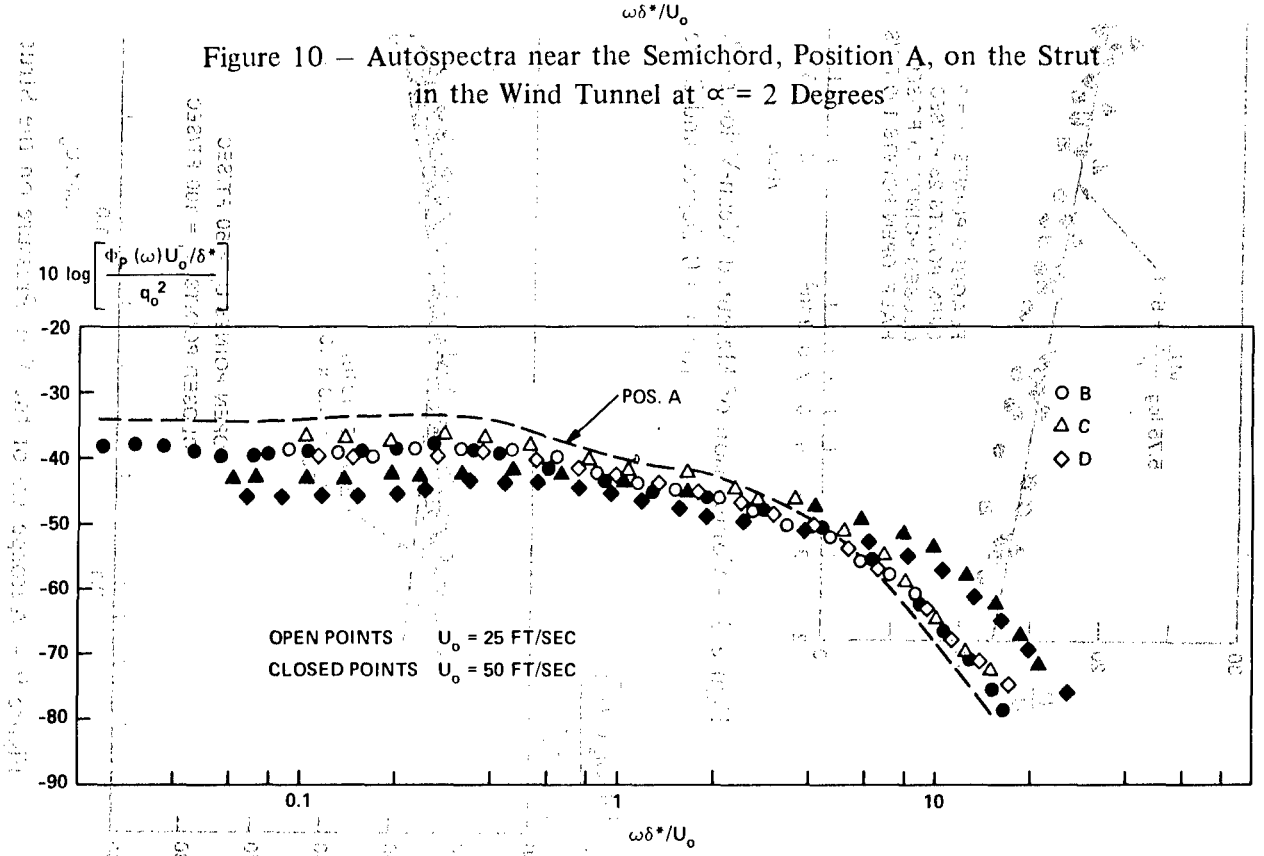

Figure 11 – Autospectra of the Wall Pressure on the Strut in the Wind Tunnel at α = 2 Degrees

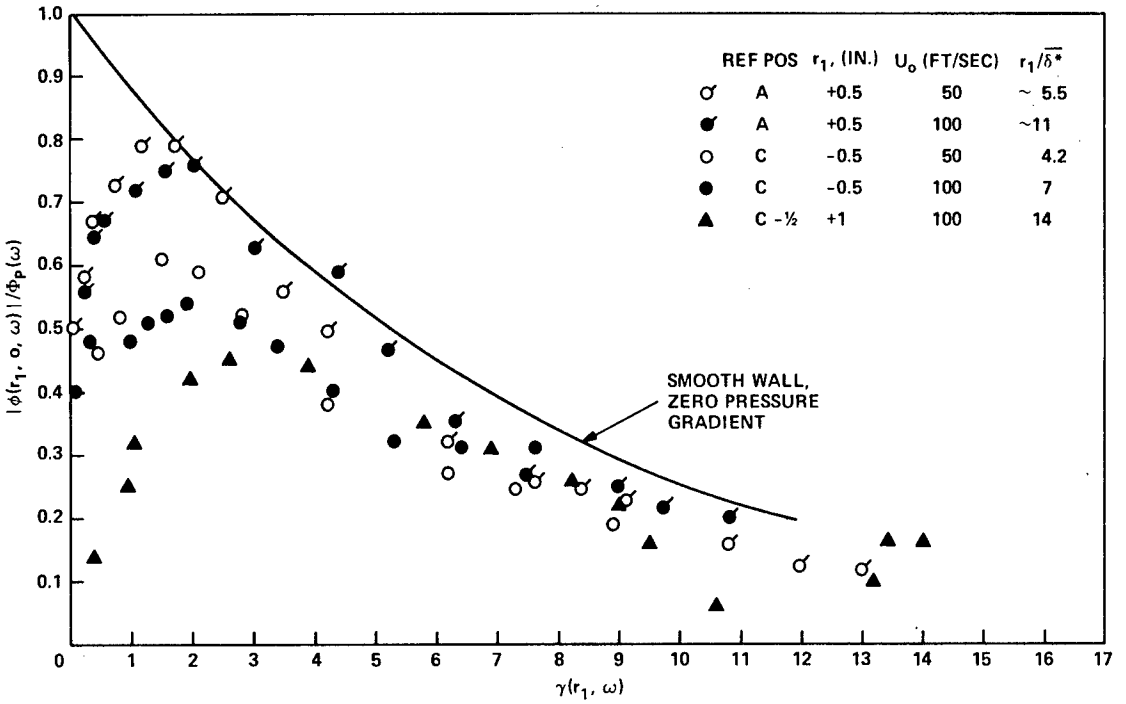

Figure 12 – Normalized Longitudinal Cross Spectral Density Magnitude on the Rigid Strut at α = 0 Degree

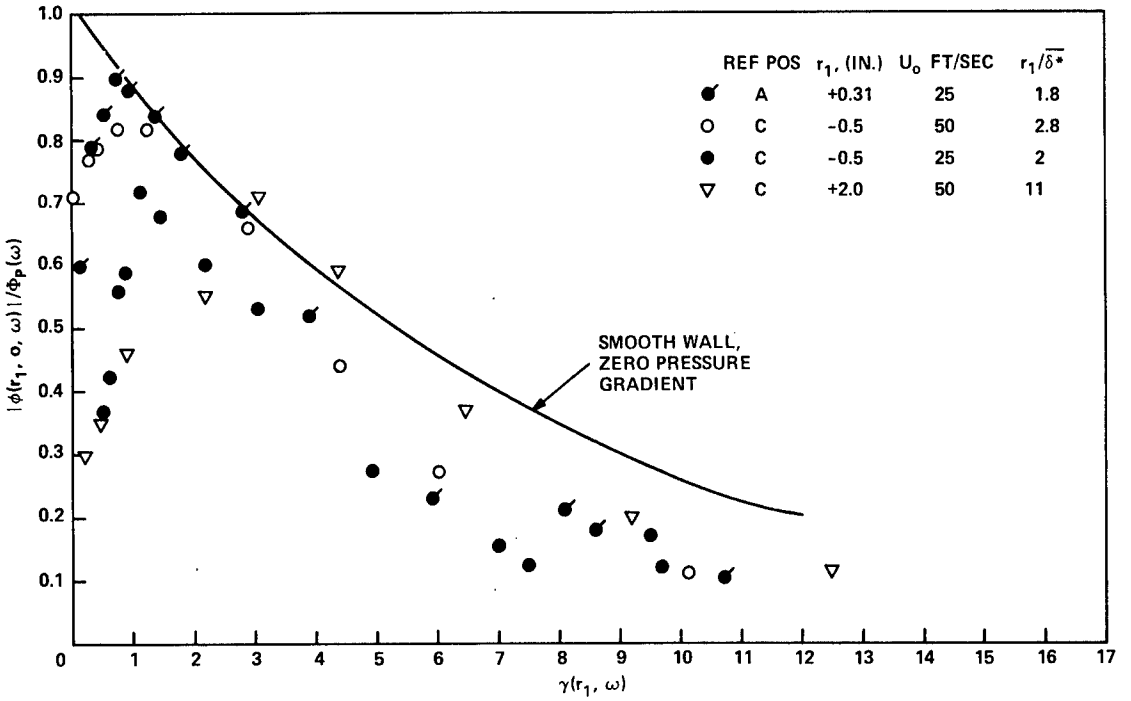

Figure 13 – Normalized Longitudinal Cross Spectral Density Magnitude on the Rigid Strut at α = 2 Degrees

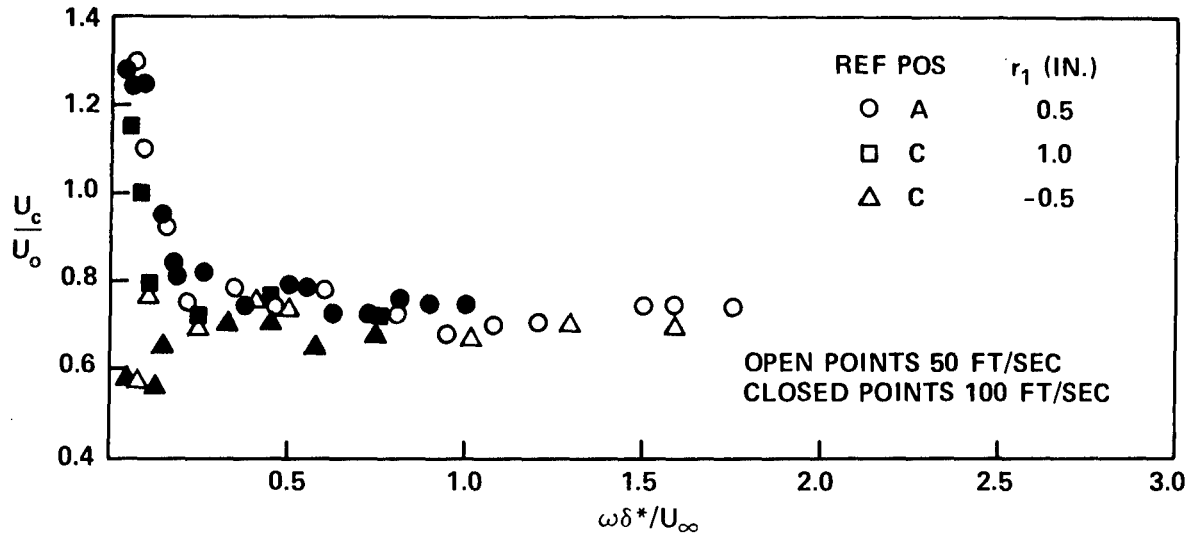

Figure 14a – $\alpha = 0$ Degree

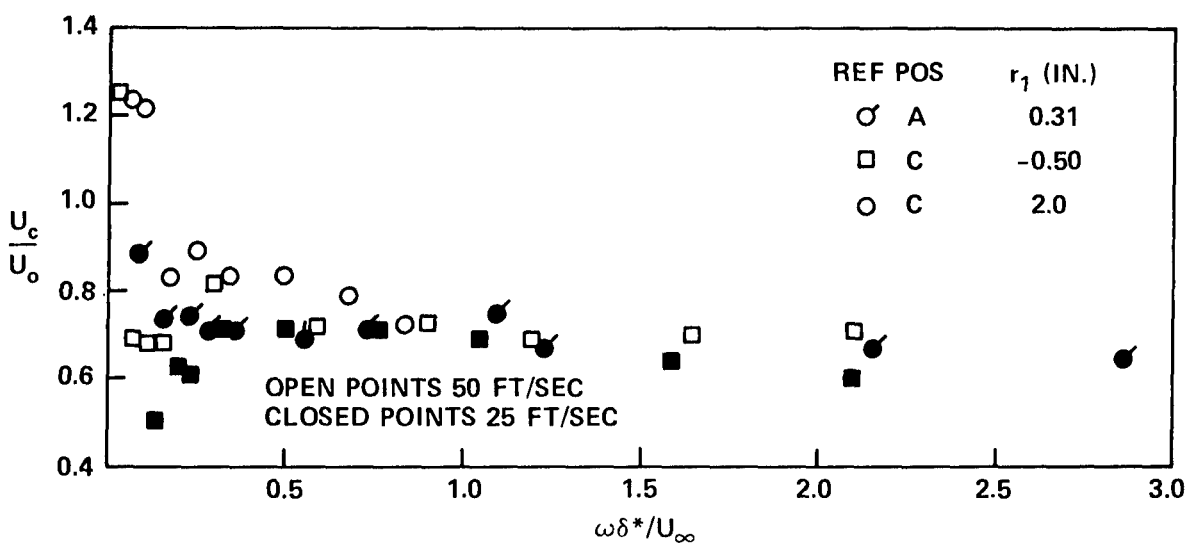

Figure 14b – $\alpha = 2$ Degrees

Figure 14 – Phase Velocities of the Wall Pressure on the Strut

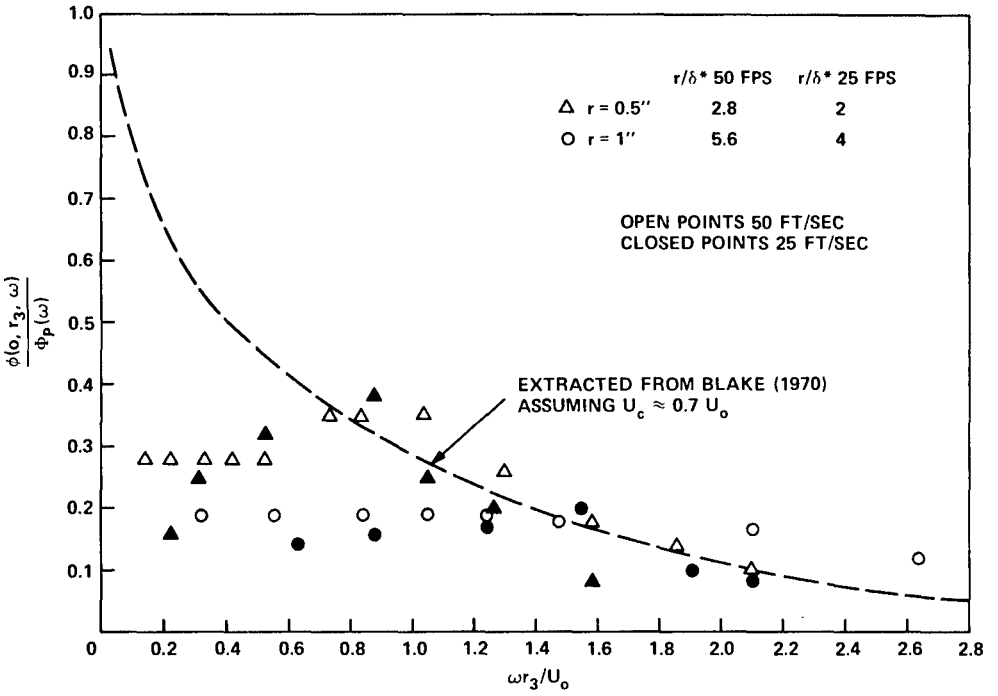

Figure 15 – Normalized Lateral Cross-Spectral Density at Position C on the Strut at α = 2 Degrees

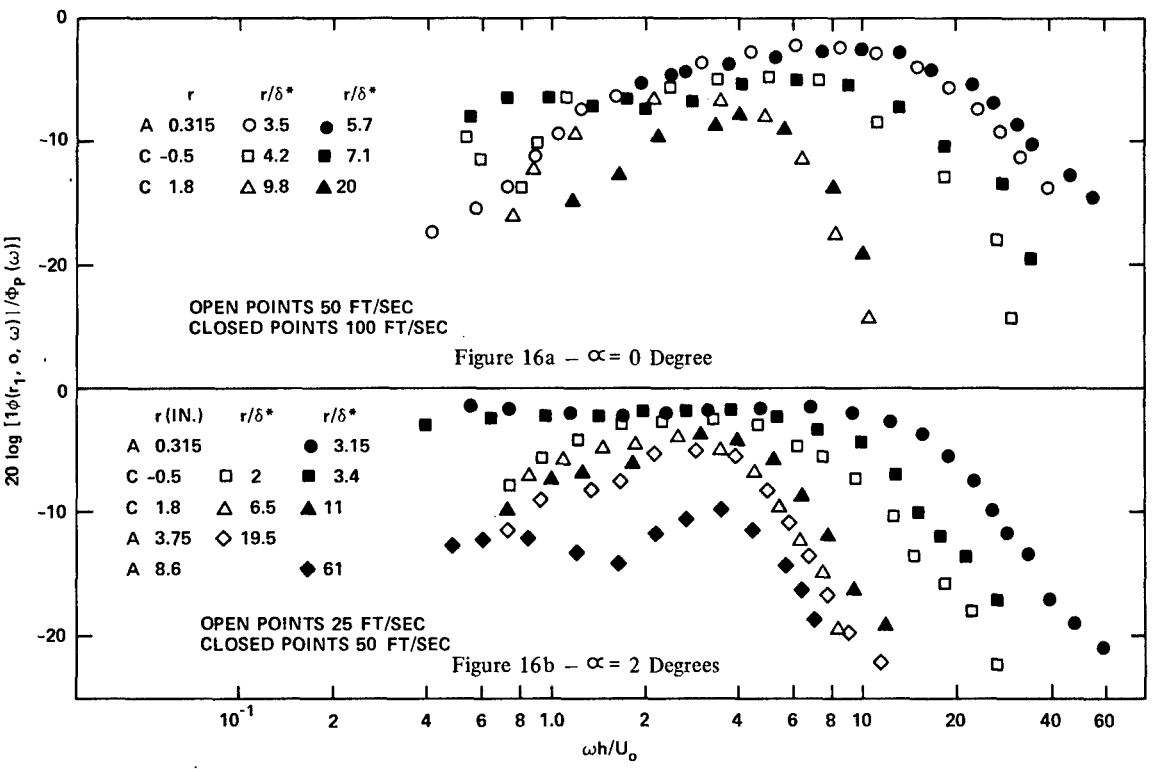

Figure 16 – Streamwise Coherence of the Pressure Field

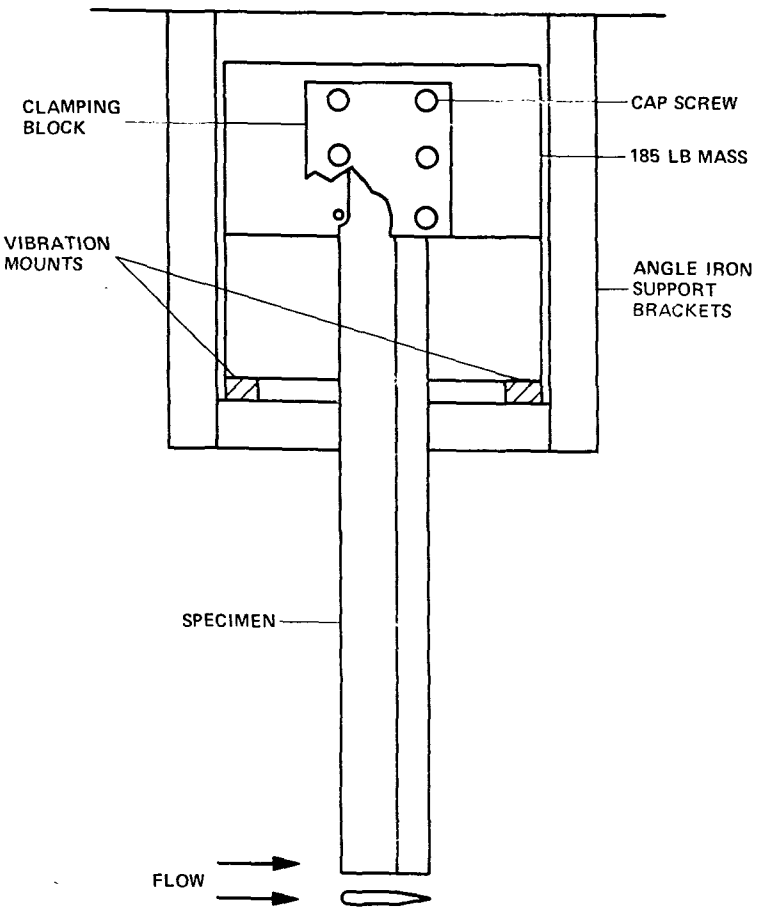

Figure 17a – Front View

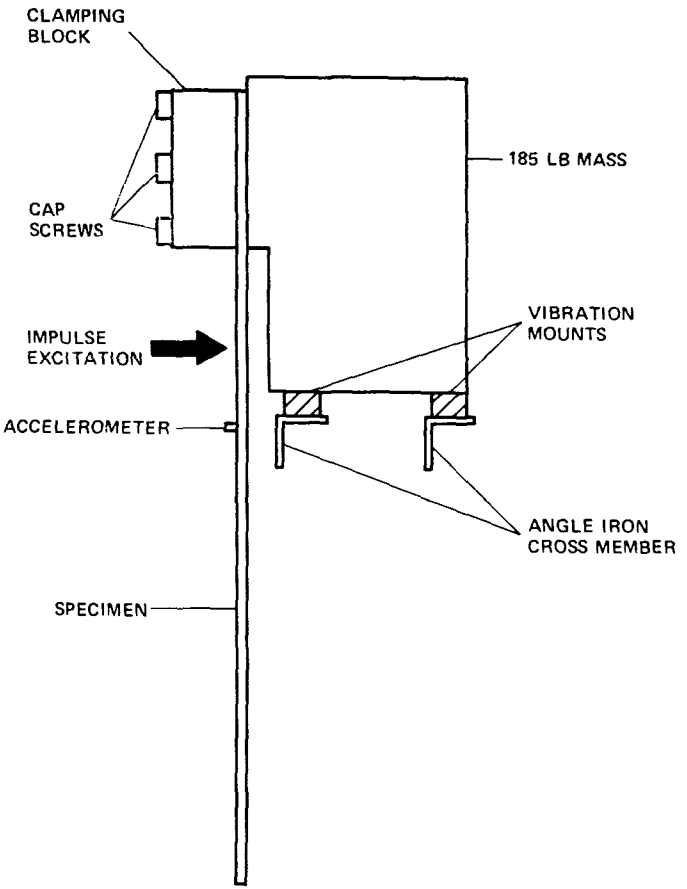

Figure 17b – Side View

Figure 17 – Beam Support and Clamping Arrangement

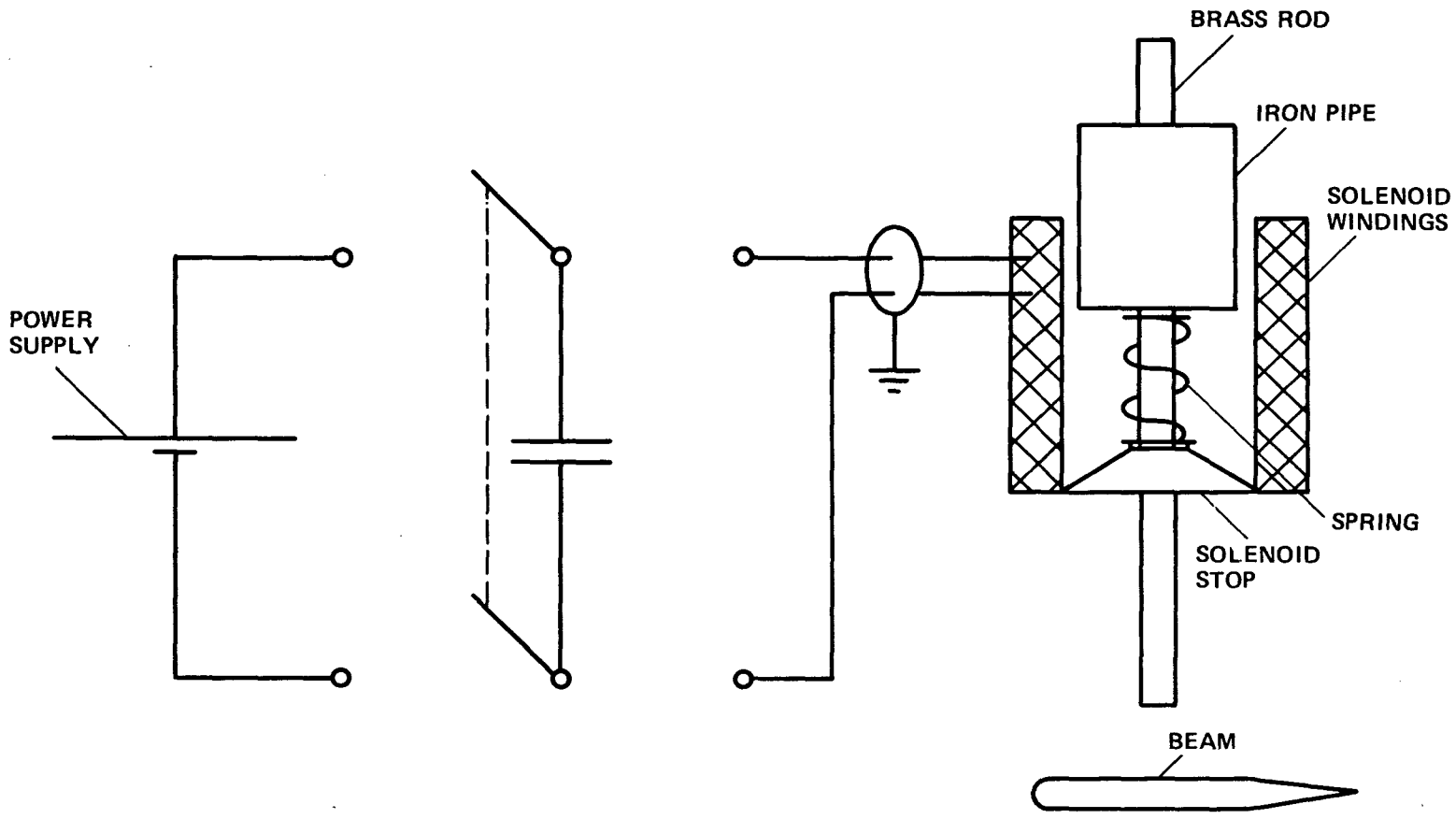

Figure 18 – Mechanical Impulse Generator Circuit

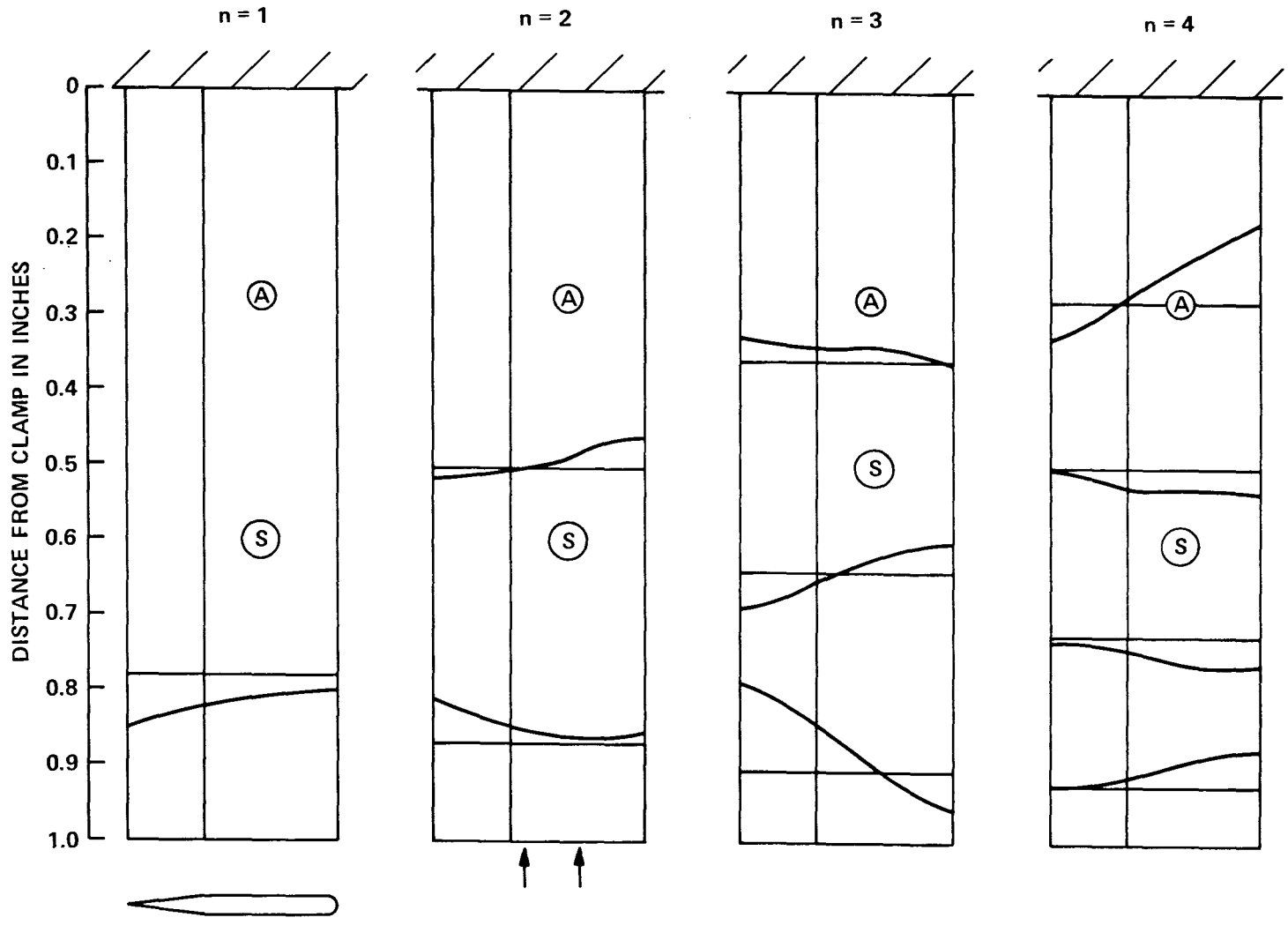

Figure 19 – Comparison of Theoretically Straight and Experimentally Determined Node Lines of the 2.75-Inch-Wide Beam

The A and S designate the position of the accelerometer and shaker, respectively.

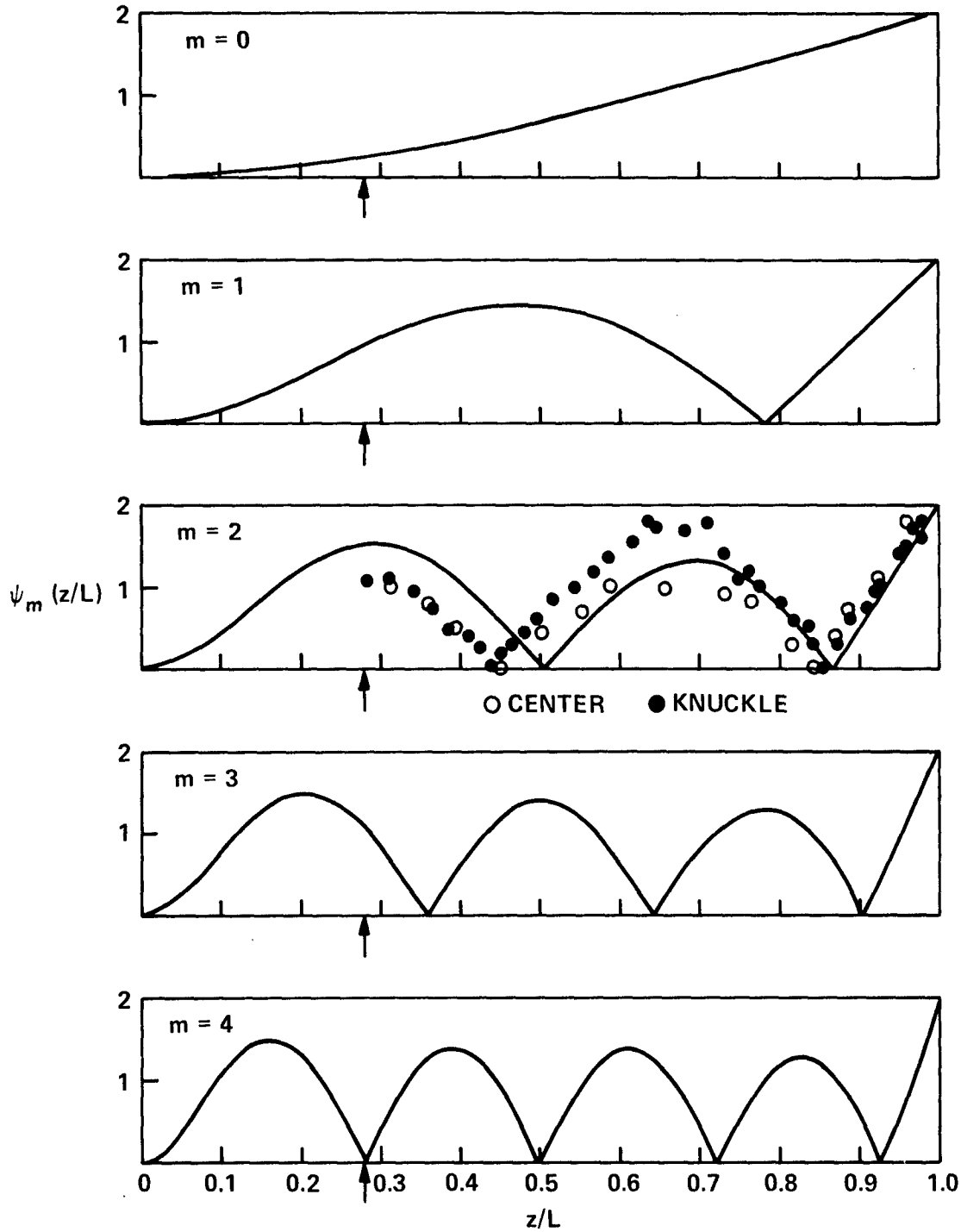

Figure 20 – Measured and Theoretical Mode Shapes for the Cantilevered Beams in Water

Measurements were made on the 2.75-inch beam. Arrows denote the location of the reference accelerometer.

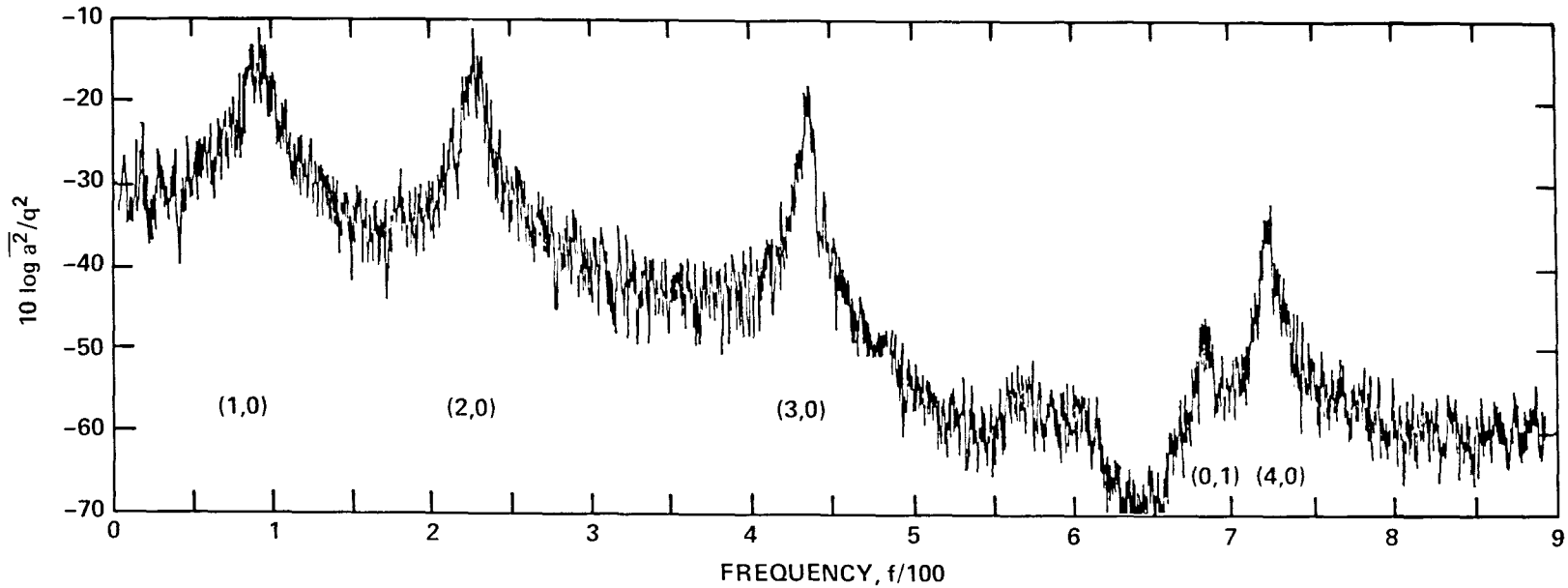

Figure 21 – Acceleration Levels, Measured in 3-Hertz Bands on a 2.75-Inch Chord Beam in Flow at 23.5 Feet per Second

Numbers in parentheses denote (m,n) mode order.

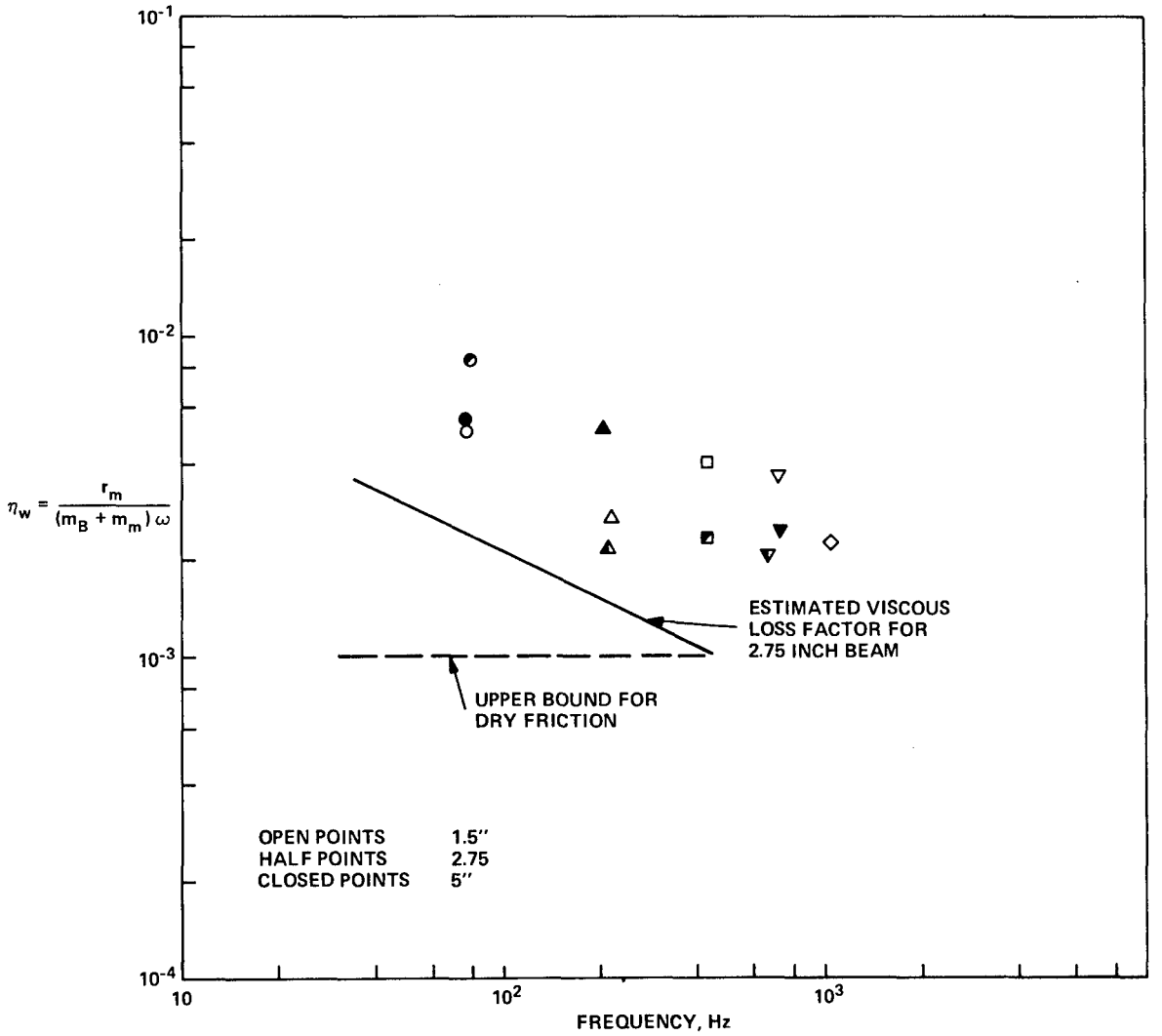

Figure 22 – Total Loss Factors of the Beams in Water with $U_0 = 0$

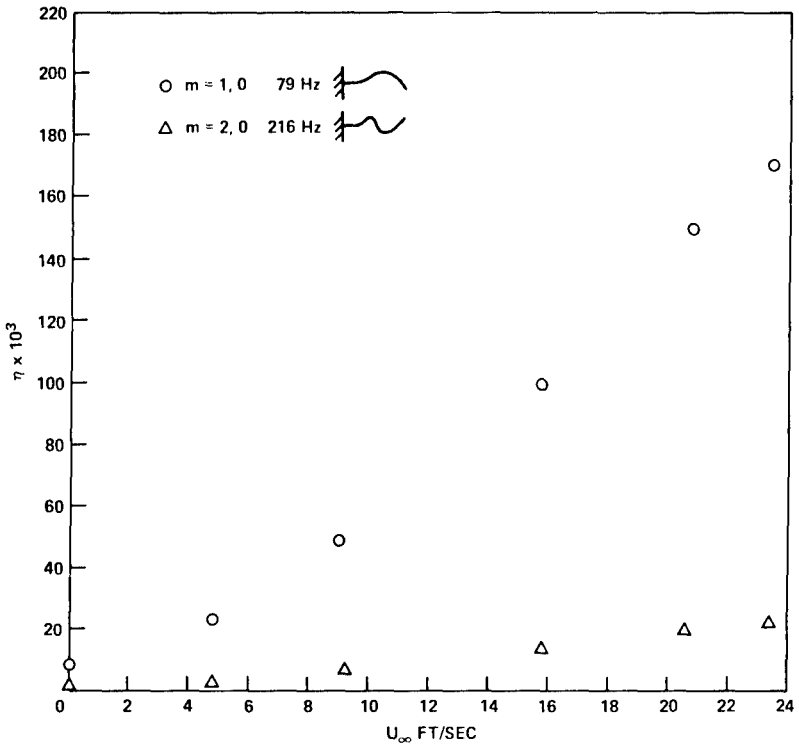

Figure 23a – Low Order Modes

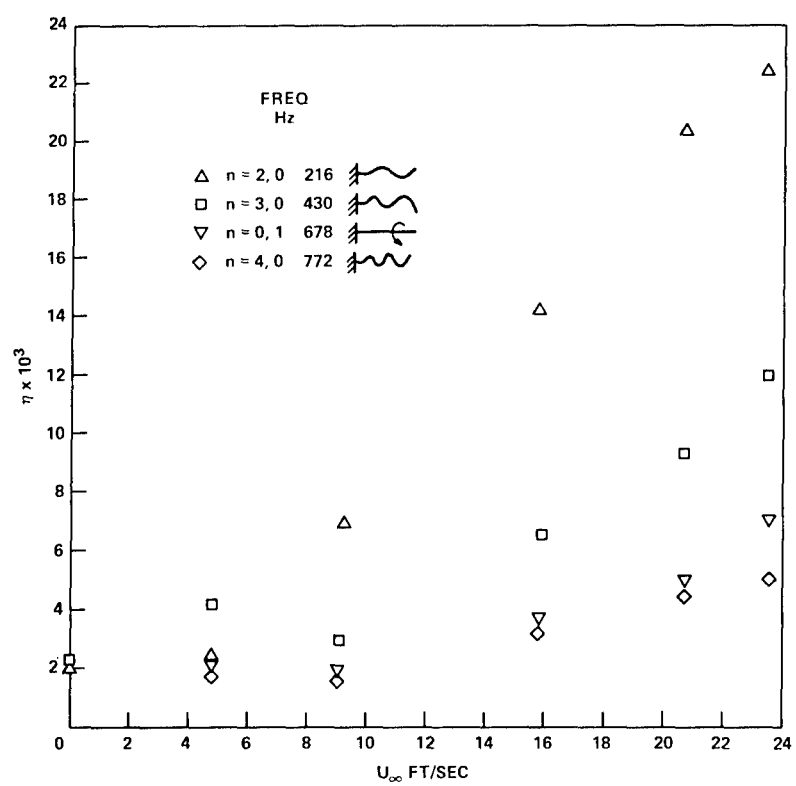

Figure 23b – High Order Modes

Figure 23 – Dependence of the Total Loss Factors of the 2.75-Inch Beam on Flow Speed

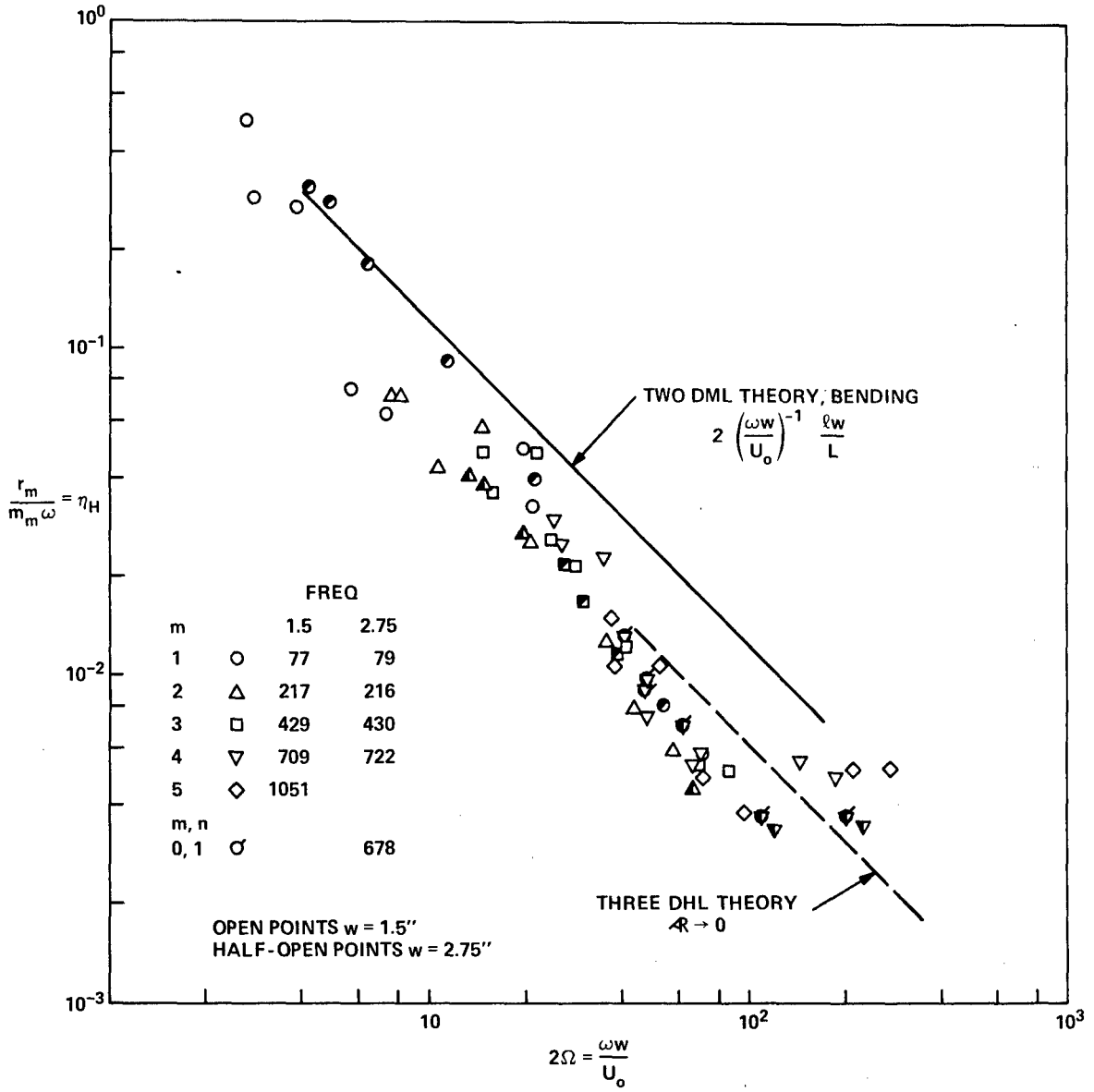

Figure 24 – Hydrodynamics Loss Factors on the 20-Inch-Long Beams of 1.5- and 2.75-Inch Widths

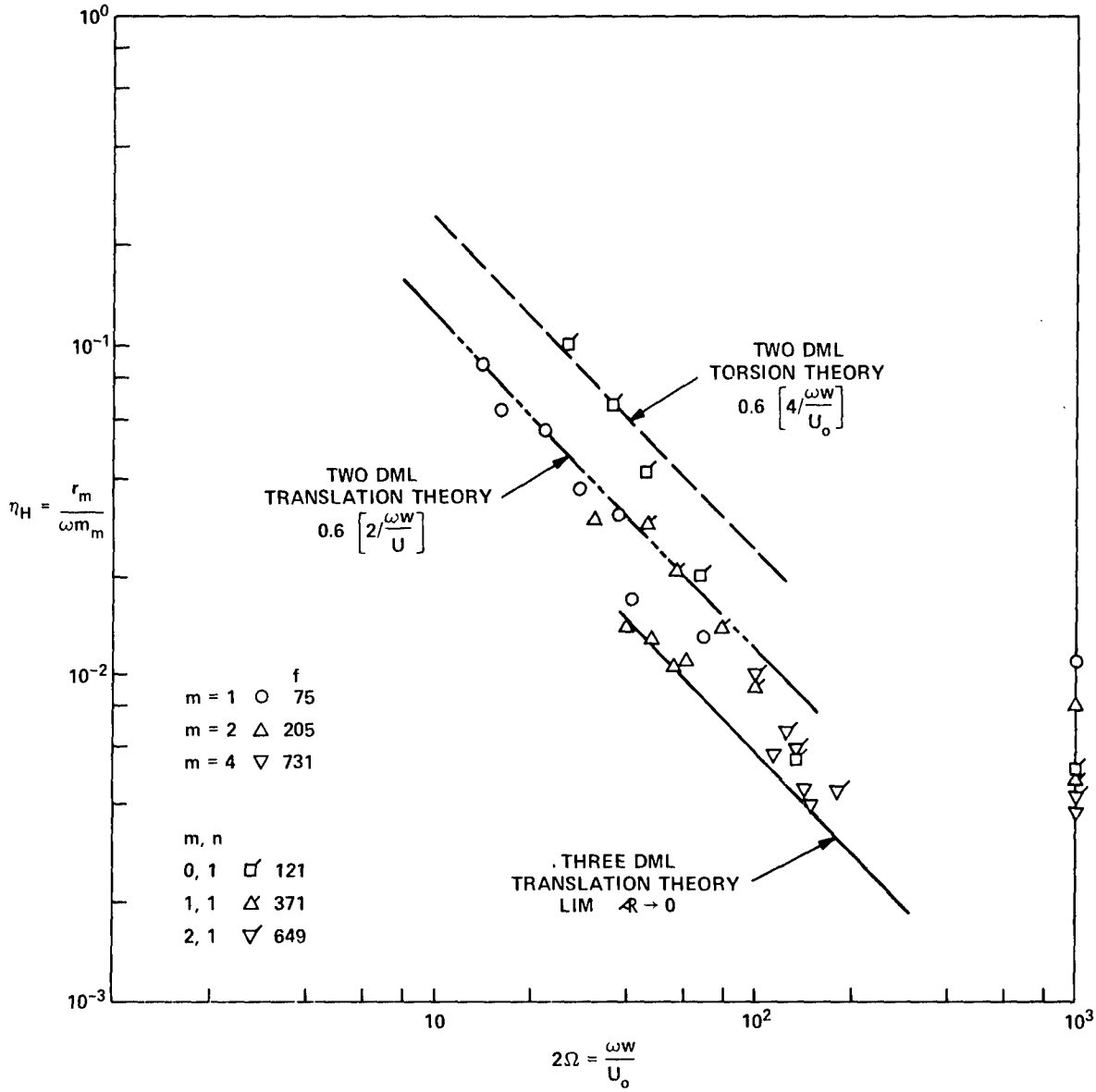

Figure 25 – Hydrodynamic Loss Factors for the 5- by 20-Inch Beam

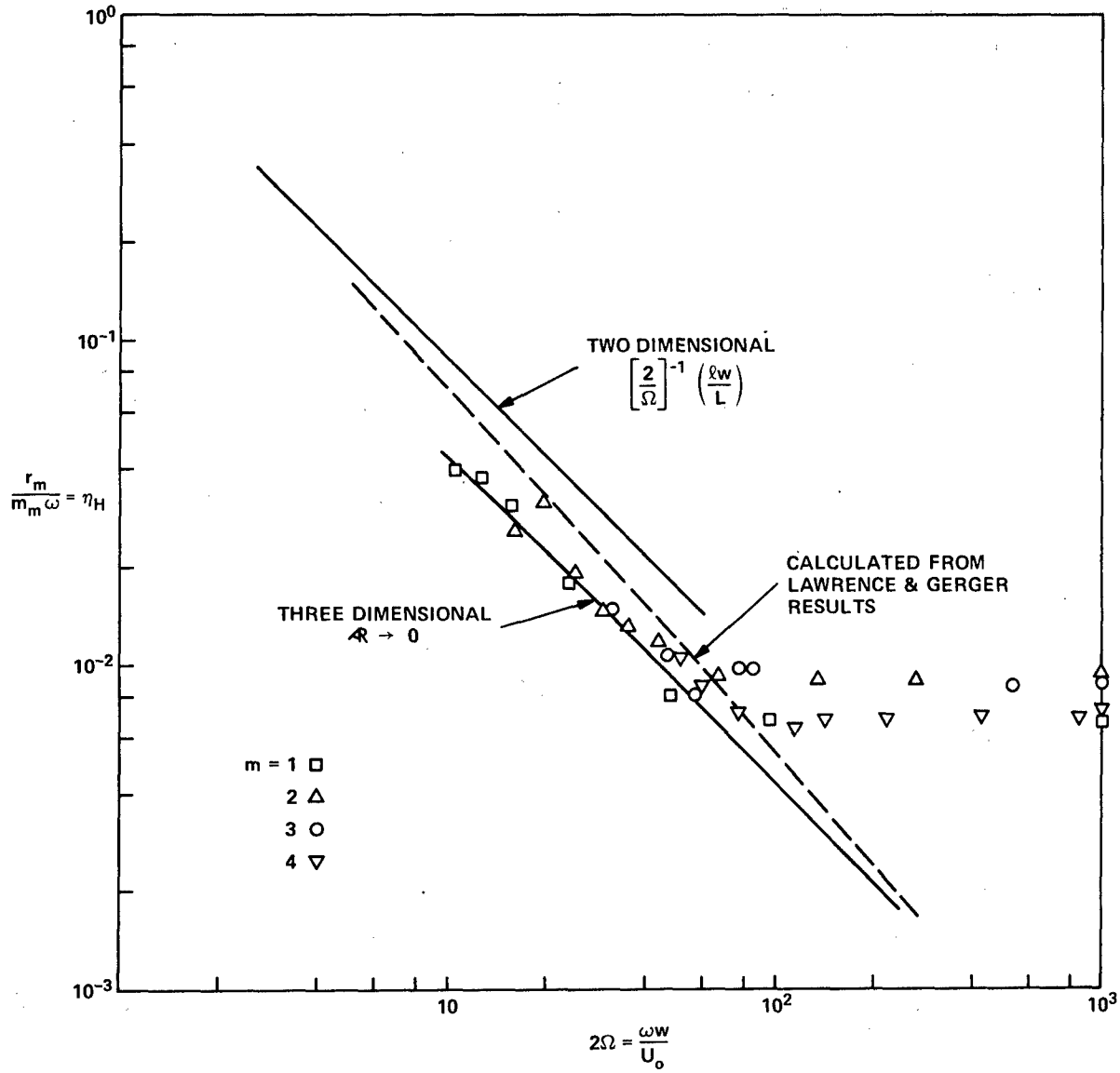

Figure 26 – Hydrodynamic Loss Factors for the 1.5- by 14-Inch Beam, $\ell w/L = 0.428$

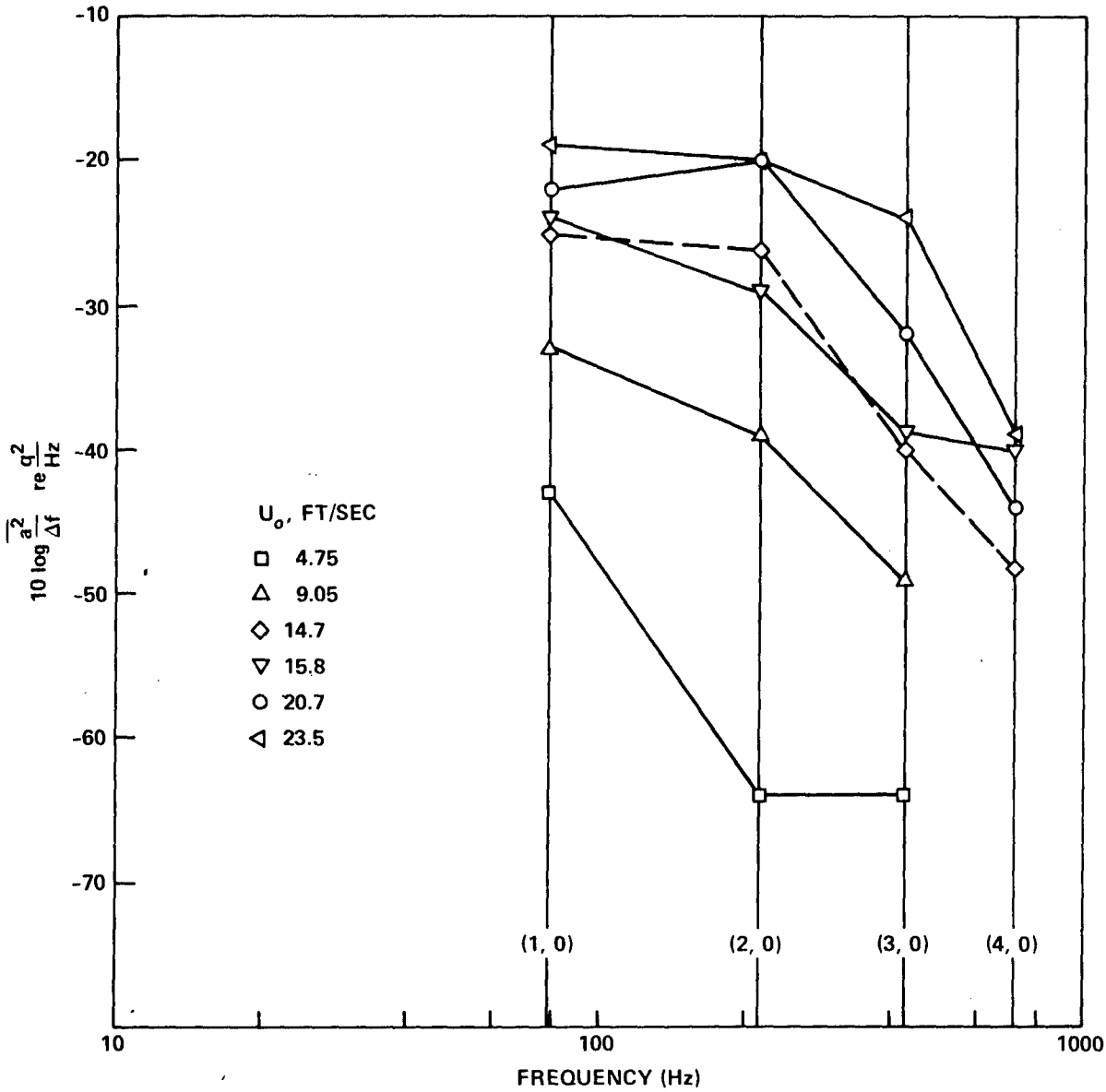

Figure 27 – Frequency Spectral Densities, $\overline{a^2}/\Delta f$, Determined from the Flow-Induced Modal Response of the 2.75-Inch Beam

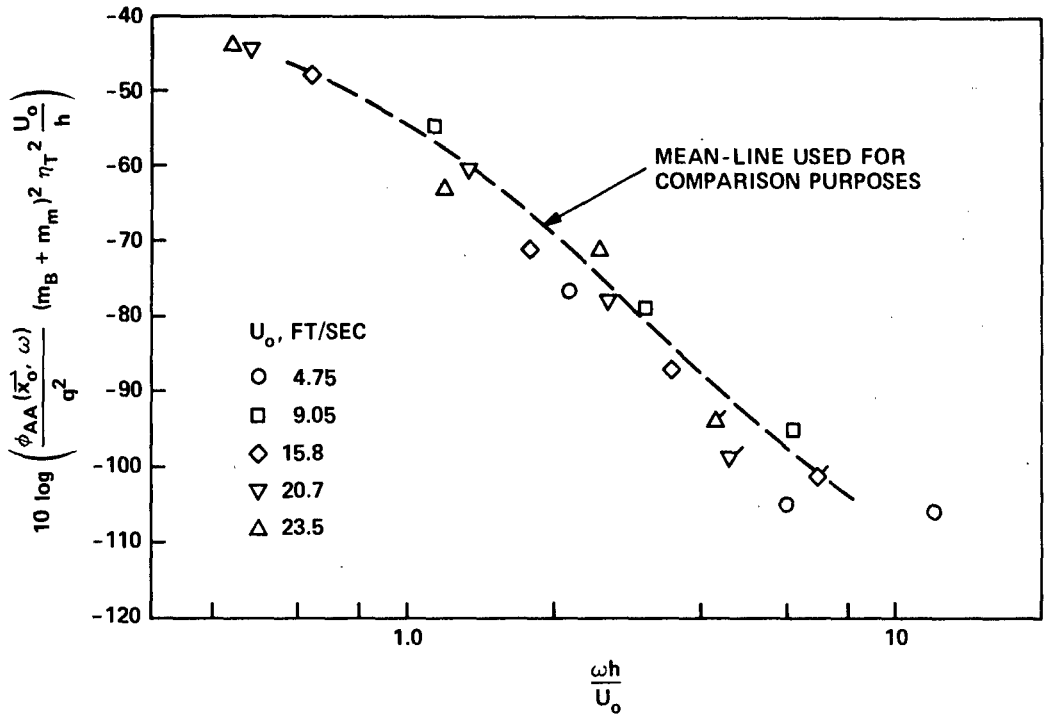

Figure 28 – Normalized Acceleration Spectra for the 2.75- by 20-Inch Beam

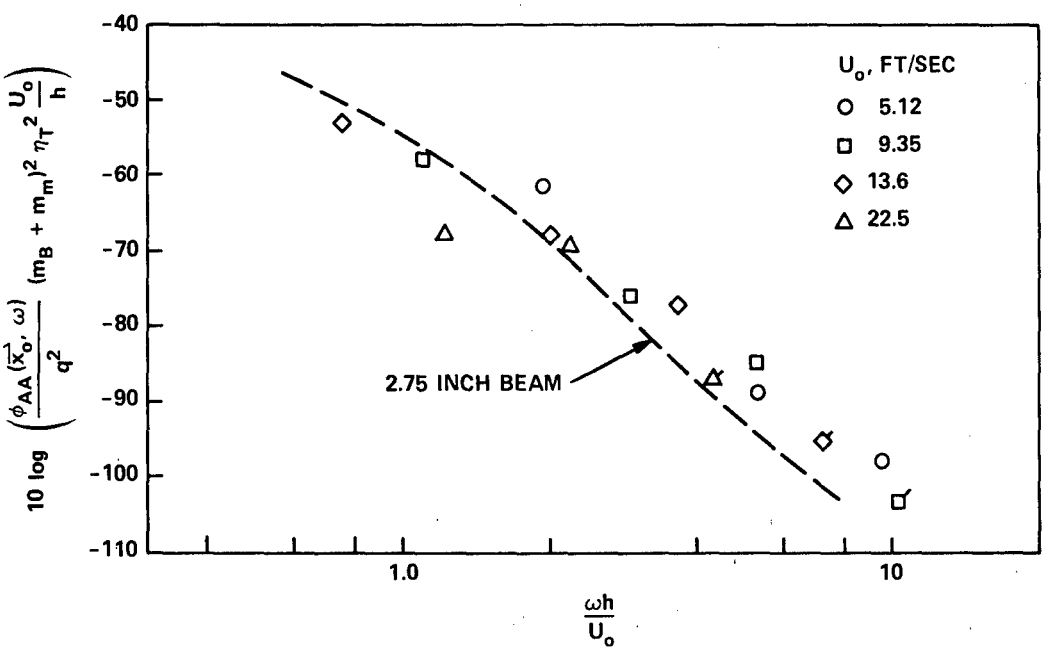

Figure 29 – Normalized Acceleration Spectra for the 5- by 20-Inch Beam

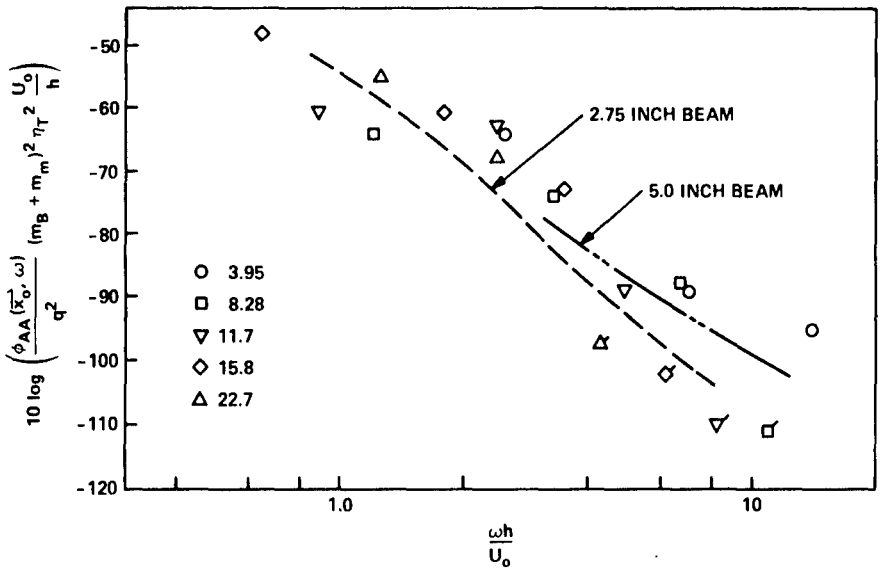

Figure 30 – Normalized Acceleration Spectra for the 1.5- by 20-Inch Beam

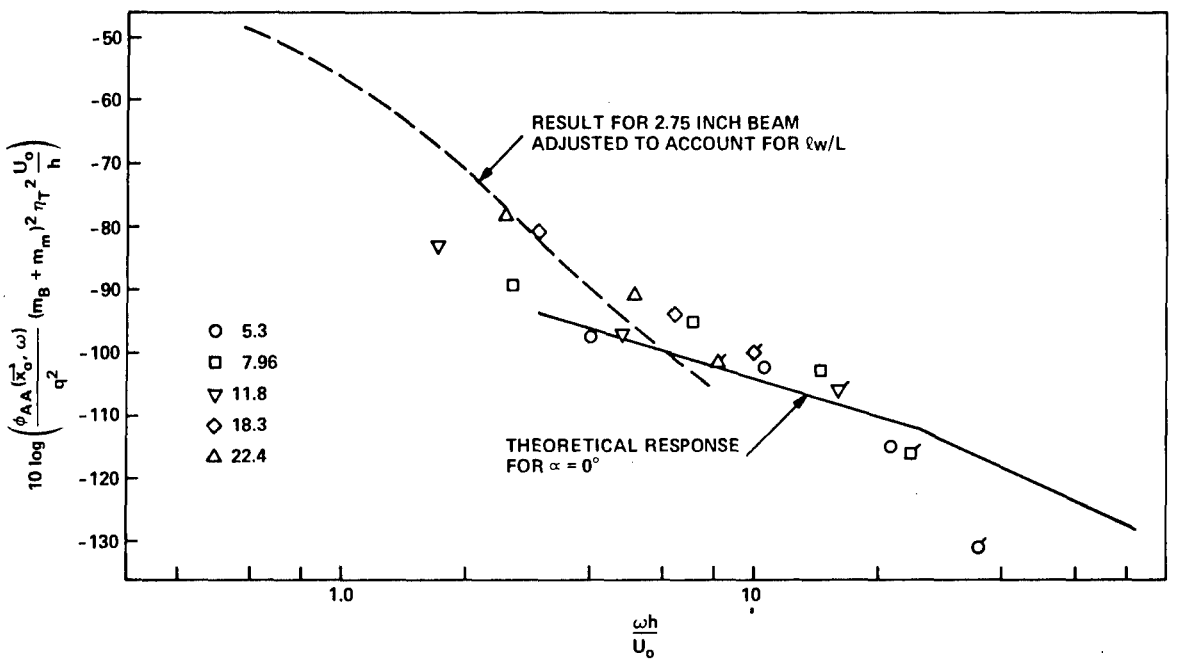

Figure 31 – Normalized Acceleration Spectra for the 1.5- by 14-Inch Beam

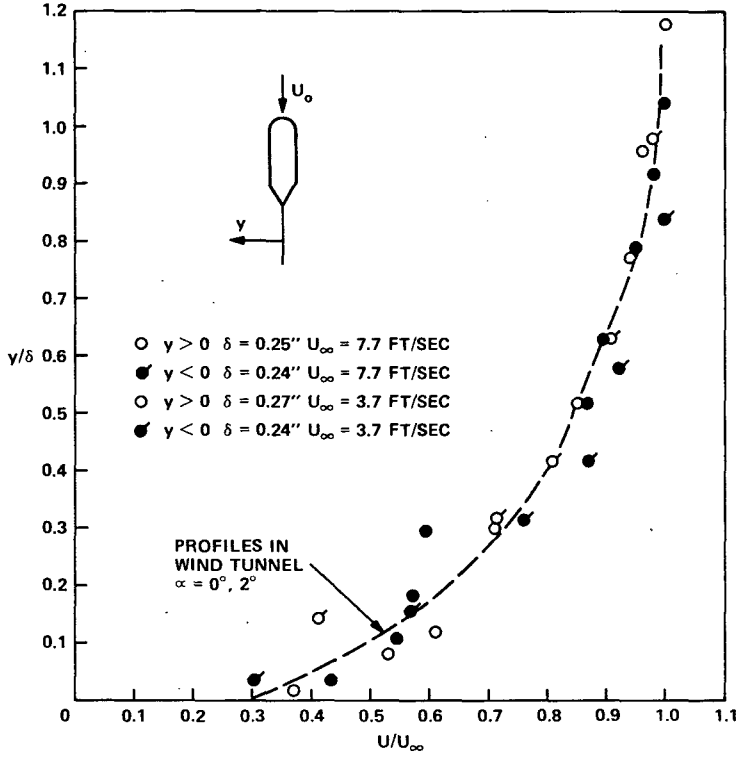

Figure 32 – Mean-Velocity Profiles at Position F behind the 2.75-Inch Strut in Water

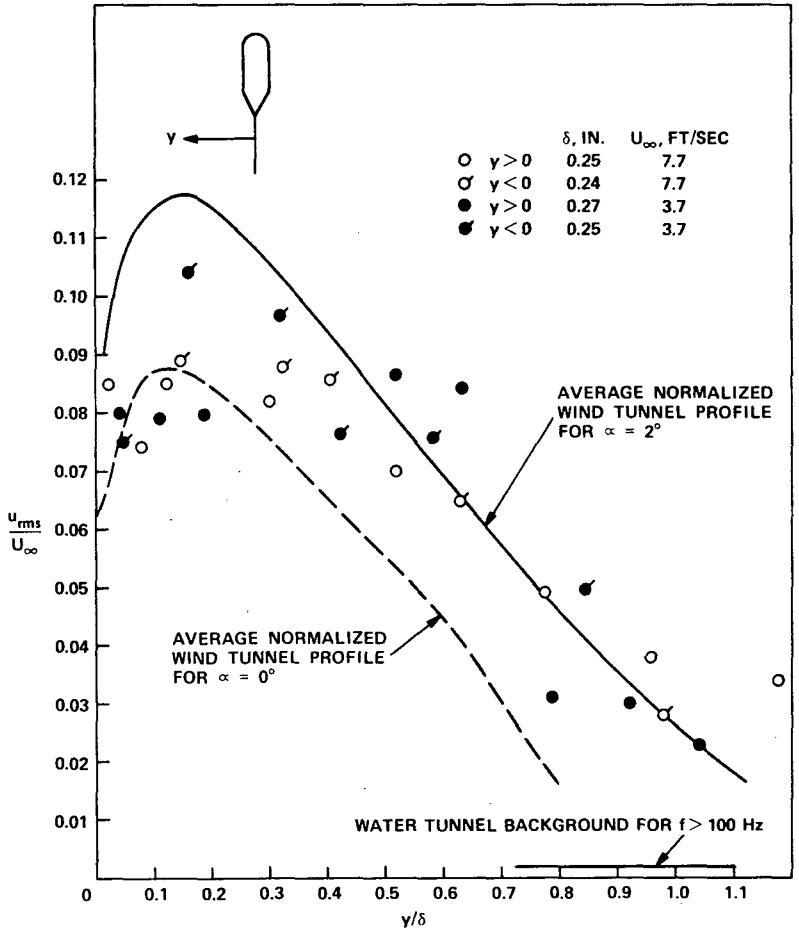

Figure 33 – Normalized Turbulence Intensities at Position F behind the 2.75-Inch Strut in Water

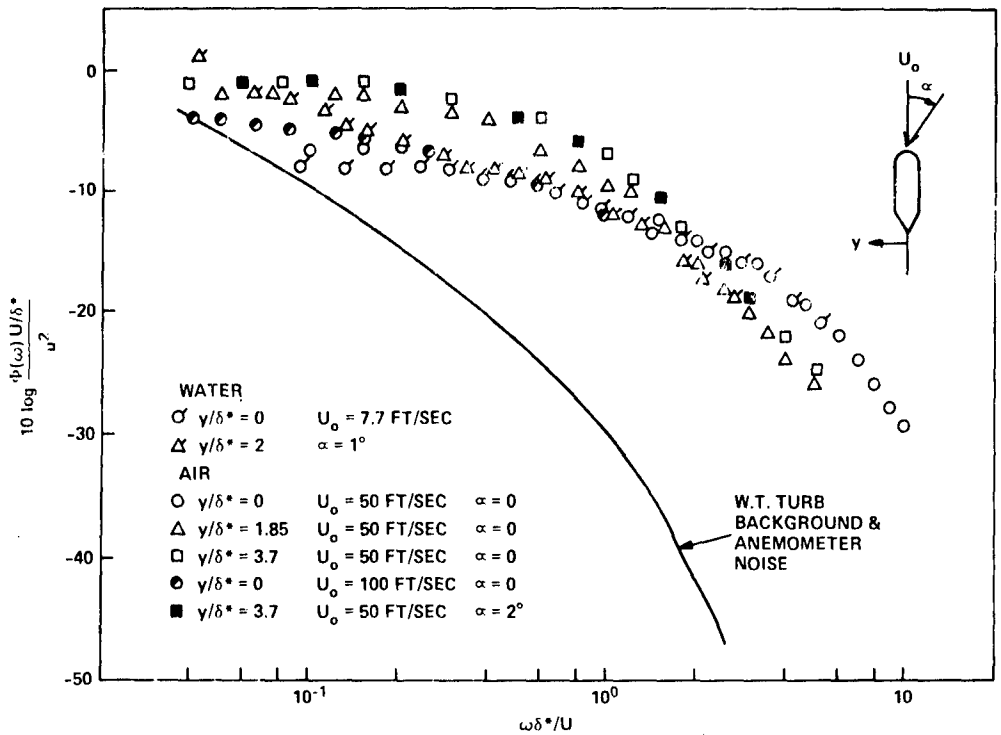

Figure 34 – Autospectra of the Longitudinal Turbulence Intensity at Position F, x/h = 0.2, Measured in Air and Water

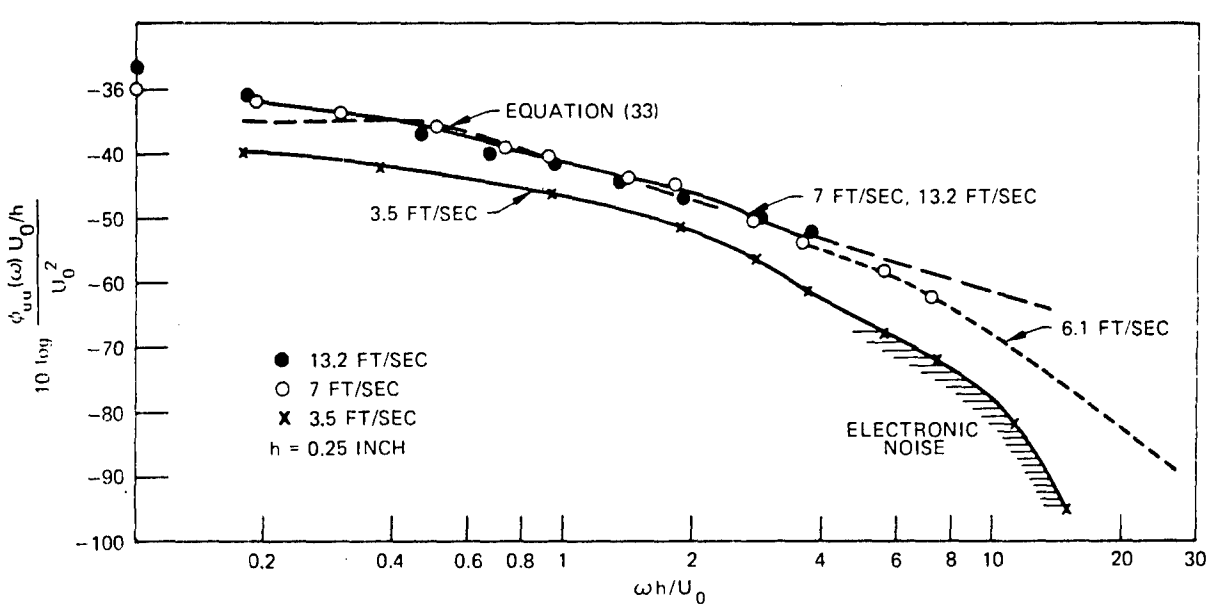

Figure 35 – Spectral Densities of Background Turbulence Intensities in the Water Tunnel

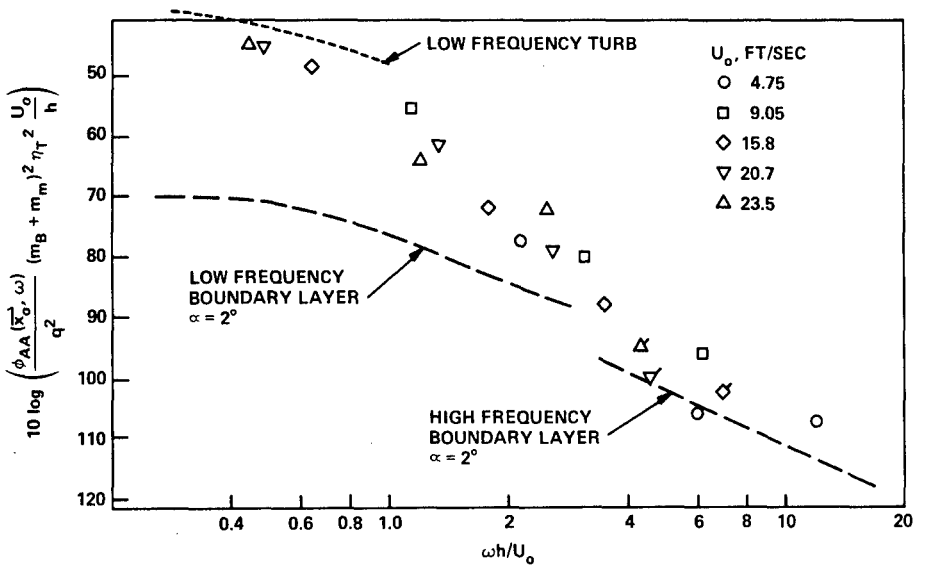

Figure 36 – Comparison of the Measured and Theoretical Dimensionless Acceleration Spectra for the 2.75-Inch Beam

TABLE 1 MEAN PROPERTIES OF BOUNDARY LAYERS

	$\alpha = 0°$								$\alpha = 2°$					
	$U_0 = 50$ ft/sec				$U_0 = 100$ ft/sec				$U_0 = 25$ ft/sec			$U_0 = 50$ ft/sec		
Position	C	D	E	F	C	D	E	F	A	C	F[+]	A	C	F[+]
δ in inches	0.66	0.69		1.1	0.42	0.5	0.58	0.84	1.21	1.49	2.15	0.9	1.09	1.62
δ/δ^*	5.35	5.5		4.9	6.3	5.1	4.8	4.2	6.35	6.1	5.1	8.7	7.4	4.9
H	1.46	1.44		1.55	1.38	1.49	1.42	1.47	1.38	1.4	1.49	1.26	1.31	1.52
$N_{R_{e\theta}} \times 10^{-3}$	2.2	2.3		4.3	2.5	3.4	4.4	7.05	1.8	2.2	3.7	2.1	2.9	5.7
$C_f \times 10^3$	4.2	3.8	-		3.1	3	3	–	4	4	–	4	3.2	-

[+]Measurements were made on the low-pressure side.

TABLE 2 RESONANCE FREQUENCIES IN WATER AND AIR

Hertz

Mode (n,m)	Water			
	L = 20			L = 14
	w = 1.50	2.75	5.00	w = 1.50
1,0	77	79	75	160
2,0	217	216	205	447
3,0	429	430	428	883
4,0	709	722	731	1438
5,0	1051	–	–	–
0,1	–	678	121	–
1,1	–	–	371	–
2,1	–	–	649	–
	Air			
1,0	106	114	122	216
2,0	292	319	355	596
3,0	577	623	666	1172
4,0	955	1027	1093	1920
0,1	–	897	171	–
1,1	–	–	517	–
2,1	–	–	900	–

TABLE 3 – COMPARISON OF BOUNDARY LAYER PARAMETERS IN AIR AND WATER

	Air ($\alpha = 2^\circ$)	Water
w in inches	22	2.75
U_0 in feet per second	50	7.7
δ^* in inches, Position F	0.32	0.05
δ/δ^*	4.9	5
δ^*/h	0.16	0.2
$\frac{U_0 w}{\nu} = N_{R_{e_w}}$	5.7×10^5	1.65×10^5
$\frac{U_0 \delta^*}{\nu} = N_{R_{e\delta^*}}$	8.3×10^3	3×10^3

REFERENCES

1. Blake, W.K., "On the Damping of Transverse Motion of Free-Free Beams in Dense Stagnant Fluids," Shock and Vibration Bulletin Vol. 42, Part 4, pp. 41–55 (Jan 1972).

2. Blake, W. K., "Radiation from Free-Free Beams under Influences of Light and of Heavy Fluid-Loading," NSRDC Report 3716 (Nov 1971).

3. Mugridge, B.D., "The Generation and Radiation of Acoustic Energy by the Blades of a Sub-Sonic, Axial Flow Fan Due to Unsteady Flow Interaction," University of Southampton (England) Ph. D. Thesis (Jan 1970).

4. Reissner, E., "On the General Theory of Thin Airfoils for Non-Uniform Motion," National Advisory Committee for Aeronautics TN 946 (Aug 1947).

5. Lin, Y.K., "Probablistic Theory of Structural Dynamics," McGraw-Hill, Inc., New York (1967).

6. Leehey, P., "Trends in Boundary Layer Noise Research," Proceedings of the Air Force Office of Scientific Research – University of Toronto, Institute for Aerospace Studies Symposium, Toronto, Ontario, Canada (20–21 May 1968).

7. Davies, H. G., "Sound from Turbulent Boundary Layer Excited Panels," Massachusetts Institute of Technology Acoustics and Vibration Laboratory Report 70208-2 (Feb 1969).

8. Leissa, A. Q., "Vibration of Plates," National Aeronautics and Space Administration Report SP-160 (1969).

9. Theodorsen, T., "General Theory of Aerodynamic Instability and the Mechanism of Flutter," National Advisory Committee for Aeronautics Report 496 (1935).

10. von Kármán, T. and W. R. Sears, Journal of the Aeronautical Sciences, Vol. 5, p. 379 (1938).

11. Lawrence, H. R. and E. H. Gerber, Journal of the Aeronautical Sciences, Vol. 19, p. 769 (1952).

12. Laidlaw, W. R. and R. L. Halfman, Journal of the Aeronautical Sciences, Vol. 23, p. 117 (1956).

13. Sears, W. R., Journal of the Aeronautical Sciences, Vol. 8, p. 104 (1940).

14. Corcos, G. M., Journal of the Acoustical Society of America, Vol. 35, p. 192 (1946).

15. Blake, W. K. and R. D. Dwyer, "A Statistical Description of the Pressure and Velocity Fields at Trailing Edges of Flat Struts," NSRDC Report 4241 (1973).

16. Schloemer, H. H., Journal of the Acoustical Society of America, Vol. 42, p. 1 (1967).

17. Coles, D., Journal of Fluid Mechanics, Vol. 1, p. 191 (1956).

18. Blake, W. K., Journal of Fluid Mechanics, Vol. 44, p. 637 (1970).

19. Kerlin, R. L. and J. C., Snowdon, Journal of the Acoustical Society of America, Vol. 47, p. 222 (1970).

20. Young, D. and R. P. Felgar, "Tables of Characteristic Functions Representing Normal Modes of Vibration of a Beam," University of Texas, Publication 4913, Engineering Research Series 44 (Jul 1, 1949).

21. Kerr, W. et al., "The Problems of the Singing Propeller," Proceedings of the Institute of Mechanical Engineering Vol. 144, p. 54 (1940).

INITIAL DISTRIBUTION

Copies	
2	ONR 1 Code 468, H. M. Fitzpatrick 1 Code 439, Dr. Perrone
2	USNA 1 Bruce Johnson 1 Lib
1	NAVPGSCOL, Monterey, Calif Attn: Dr. Targut Sarpkaya
1	USNROTC & NAVADMINUMIT
1	NAVWARCOL
3	NAVSHIPSYCOM 1 SHIPS 037 2 SHIPS 0372, R. Sherwood and A. Paladino
2	NAVUSEACEN, San Diego 1 Dr. A. Fabula 1 Dr. J. Hoyt
3	NLONLAB NUSC 1 Dr. H. Bakewell 1 Dr. H. Schloemer 1 Dr. W. Strawderman
2	NAVSEC 1 SEC 6110 1 SEC 6148
12	DDC
1	American Univ Attn: Prof. Mark Harrison, Chairman Dept of Physics
1	Univ of California at Los Angeles Attn: Prof. W. C. Meechan Dept of Engineering
1	Univ of California at San Diego Attn: Prof. J. W. Miles Institute of Geophysics and Planetary Physics
2	Catholic Univ of America 1 Dr. F. A. Andrews 1 Dr. M. Casarella

Copies	
9	MIT 1 Dr. R. H. Lyon, Dept Mech E 1 Dr. S. Crandall, Dept, NAME 1 Dr. P. Leehey, Dept, NAME 1 Dr. Ira Dyer 1 Dr. S. Widnall, Dept, Aeronau Astronautics 1 Dr. H. Davies 1 Prof. P. M. Morse 1 Prof. K. U. Ingard
1	Univ of Michigan, Dept of Aerona & Astronautical Engineering Attn: Prof. W. W. Willmarth
2	Univ of Minnesota 1 Prof. R. Plunkett 1 Prof. R. Lambert
1	St. Anthony Falls Hydraulic Lab Univ of Minnesota Attn: Dir. Mr. J. M. Killen
2	Univ of Notre Dame Engineering Sciences Dept 1 Dr. A. F. Strandhagen 1 Prof. A. A. Szewczyk
3	ARL, Penn State Univ 1 Dr. B. Parkin 1 Dr. E. J. Skudrzyk 1 Dr. R. Arndt
2	SWRI 1 Dr. Wilfred Baker 1 Editor, Applied Res Review
2	SIT/DL 1 Dr. J. Breslin 1 Dr. R. J. Nickerson
2	Binary Systems Inc., L.I., N.Y. 1 Mr. S. Gardner 1 Mr. O. Lindeman
1	Bolt Beranek & Newman Inc. Van Nuys, Calif Attn: Dr. P. White

Copies	
6	Bolt Beranek & Newman Inc. Cambridge 1 Dr. N. A. Brown 1 Dr. D. Chase 1 Dr. P. Smith 1 Dr. K. L. Chandiramani 1 Dr. J. Barger 1 Dr. F. Bergeron
2	Cambridge Acoustical Associates 1 Dr. M. C. Junger 1 Dr. D. Feit
1	Gen Applied Sciences Lab., Inc. Westbury, L.I., N.Y. Attn: Dr. F. Lane
2	Electric Boat Div, General Dynamics Corp 1 Mr. William Ezell 1 Mr. Michael Pakstys, Jr.
1	Hydrospace Res Corp. Attn: Lib
1	Tetratech Inc. Attn: Dr. D. Ross
1	Dr. Ewald G. Eichler 101 Trowbridge St. Cambridge, Ma. 02138
1	Dr. A. A. Hudimac 12100 Devilwood Dr. Rockville, Md. 20854

CENTER DISTRIBUTION

Copies	Code
8	15 1 1505 1 154 2 1544 1 M. L. Miller 3 1552 1 Dr. T. T. Huang 1 Dr. F. B. Peterson
2	1844 1 Mr. F. M. Henderson
42	19 1 1901 1 1902 1 1903 1 1906 1 1908 2 1926 1 S. G. Solomon 1 1932 1 1933 1 194 20 1942 1 Dr. F. D. DeMetz 1 F. E. Geib 1 L. J. Maga 1 R. W. Brown 1 B. E. Bowers 1 Dr. A. J. Tucker 1 L. S. Chandler 1 P. J. Granum 10 Dr. W. K. Blake 5 1945 1 Dr. M. L. Rumerman 1 Dr. W. T. Reader 1 F. Schloss 1 F. W. Desiderati 1 1962 2 1966 1 Dr. Y. Liu

Distribution authorized by fonecon between J. Shen, NSRDC, Code 1942 and A. Paladino, NAVSHIPS, Code 037 on 25 April 1973

UNCLASSIFIED
Security Classification

DOCUMENT CONTROL DATA - R & D

(Security classification of title, body of abstract and indexing annotation must be entered when the overall report is classified)

1. ORIGINATING ACTIVITY *(Corporate author)* Naval Ship Research and Development Center Bethesda, Md. 20034	2a. REPORT SECURITY CLASSIFICATION UNCLASSIFIED 2b. GROUP

3. REPORT TITLE

VIBRATORY DYNAMICS OF FLOW-EXCITED STRUTS IN WATER

4. DESCRIPTIVE NOTES *(Type of report and inclusive dates)*

Final Report

5. AUTHOR(S) *(First name, middle initial, last name)*

William K. Blake and Lawrence J. Maga

6. REPORT DATE December 1973	7a. TOTAL NO. OF PAGES 73	7b. NO. OF REFS 21
8a. CONTRACT OR GRANT NO. b. PROJECT NO. Work Unit 1942-057 c. SF-35-452-007 d. Task 1356	9a. ORIGINATOR'S REPORT NUMBER(S) Report 4087 9b. OTHER REPORT NO(S) *(Any other numbers that may be assigned this report)*	

10. DISTRIBUTION STATEMENT

APPROVED FOR PUBLIC RELEASE: DISTRIBUTION UNLIMITED

11. SUPPLEMENTARY NOTES	12. SPONSORING MILITARY ACTIVITY Naval Ship Systems Command, 037 Washington, D. C. 20360

13. ABSTRACT

The general problem of the response of a cantilevered beam to flow over its surface is considered experimentally and theoretically. The measured flow induced modal vibratory motion of a nonsinging beam is compared to theoretical estimates of inflow turbulence excitation and boundary-layer excitation. The comparison indicates that while the response to turbulent inflow is dominant at low frequencies, the response of the strut to its own boundary layer is important at high frequencies. The magnitude of hydrodynamically induced damping is also characterized experimentally. It is shown that results agree favorably with an approximate expression based on finite-aspect-ratio, unsteady airfoil theory. Loss factors, based on entrained mass, are found to be inversely proportional to a reduced frequency based on the width of the strut and inflow speed. Finally, a wind tunnel study of the statistical properties of the boundary layer formed on the strut is described. The results disclose that flow separation at the leading edge, which is sensitive to angles of attack, generates a low-frequency pressure field that is markedly higher than that normally encountered in boundary layers. At high frequencies the pressure field is influenced by the local flow parameters normally used in boundary-layer studies.

DD FORM 1 NOV 65 1473 (PAGE 1)

S/N 0101-807-6801

UNCLASSIFIED
Security Classification

14. KEY WORDS	LINK A ROLE	LINK A WT	LINK B ROLE	LINK B WT	LINK C ROLE	LINK C WT
Vibration						
Fluid loading						
Damping						
Turbulence						
Boundary layer						
Hydrodynamic loading						